BEYOND 5G – OPTICAL NETWORK CONTINUUM
(H2020 – Grant Agreement № 101016663)

Deliverable D5.3

B5G-OPEN Techno-Economic Validation

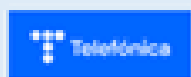|	
Editor	António Eira (INF-P)
Contributors	TID, UC3M, TIM, INF-D, INF-P, Adtran, UPC, OLC, PLF, ELIG
Version	2.0
Date	30.10.2024
Distribution	PU

DISCLAIMER

This document contains information, which is proprietary to the B5G-OPEN (Beyond 5G – OPtical nEtwork coNtinuum) consortium members that is subject to the rights and obligations and to the terms and conditions applicable to the Grant Agreement number 101016663. The action of the B5G-OPEN consortium members is funded by the European Commission.

REVISION HISTORY

Revision	Date	Responsible	Comment
0.1	May 12, 2024	A. Eira (INF-P)	Table of Content
0.2	Oct 13, 2024	A. Eira (INF-P)	Draft version
0.3	Oct 20, 2024	A. Eira (INF-P)	All contributions integrated
1.0	Oct 24, 2024	A. Eira (INF-P)	Final version
2.0	Oct 30, 2024	A. Eira (INF-P)	Version update after quality check

LIST OF AUTHORS

Name	Partner
Albert Rafel	BT
Kris Farrow	BT
Paul Wright	BT
Caio Marciano Santos	HHI
Behnam Shariati	HHI
Johannes Fischer	HHI
Luis Velasco	UPC
Marc Ruiz	UPC
Jaume Comellas	UPC
Filippo Cugini	CNIT
Ramon Casellas	CTTC
Laia Nadal	CTTC
Ricardo Martínez	CTTC
Farhad Arpanaei	UC3M
Jose Alberto Hernández	UC3M
Fernando Díaz de María	UC3M
Óscar González de Dios	TID
Edward James Echeverry	TID/TSA
Ivan De Francesca	TID/TSA
Pablo Pavón Mariño	ELIG
Francisco Javier Moreno	ELIG
António Eira	INF-P
João Pedro	INF-P
Antonio Napoli	INF-G
Carlos Castro	INF-G
Marco Quagliotti	TIM
Alexandros Stavdas	OLC-E
Rui Bian	PLF
Lutz Rapp	ADTRAN
Nicola Calabretta	TUE

Abbreviations and Acronyms

Acronym	Expansion
5G	Fifth Generation
5GPPP	5G Infrastructure Public Private Partnership
AAU	Active Antenna Unit
ACO	Access Central Office
ADM	Add/Drop Multiplexer
AI	Artificial Intelligence
AP	Access Point
API	Application Programming Interface
AR	Augmented Reality
ASE	Amplified Spontaneous Emission
B5G	Beyond 5G
BBN	BackBone Network
BER	Bit Error Ratio
BNG	Broadband Network Gateway
BSS	Business Support System
BVT	Bandwidth/bit rate Variable Transceivers
Capex	Capital Expenditure
CAGR	Compound Annual Growth Rate
CBR	Constant Bit Rate
CDN	Content Delivery Network
CN	Core Node
CNF	Cloud-native Network Function
CO	Central Office
CP	Control Plane
CPT	Coherent Pluggable Transceiver
CPRI	Common Public Radio Interface
C-RAN	Centralized-Radio Access Network
CSG	Cell Site Gateway
CU	Central Unit
DC	Data Centre
DCI	Data Centre Interconnection
DSC	Digital Subcarrier
DSCM	Digital Subcarrier Multiplexing
DSLAM	Digital Subscriber Line Access Multiplexer
DSP	Digital Signal Processing
DSR	Digital Signal Rate
DT	Digital Twin
DTC	DT City
DU	Distributed Unit
DWDM	Dense Wavelength Division Multiplexing
E/O	Electrical to Optical
E2E	End-To-End

EC	European Commission
eCPRI	Enhanced CPRI
EDFA	Erbium Doped Fibre Amplifier
ENP	E-Lighthouse Network Planner
EPA	Enhanced Platform Awareness
Eth.	Ethernet
ETSI	European Telecommunication Standards Institute
ETSI MANO	ETSI NFV Management and. Orchestration
FCAPS	Fault, Configuration, Accounting, Performance, Security
FTTA	Fibre-To-The-Antenna
FTTH	Fibre-To-The-Home
FWM	Four-Wave Mixing
gNB	gNodeB
GW	Gateway
HD	High Definition
HLS	High Layer Split
HSI	High Speed Internet
HTC	Holographic-Type Communications
IBN	Intent-Based Networking
IETF	Internet Engineering Task Force
IIoT	Industrial IoT with cloudification
ILP	Integer Linear Programming
INT	In-band Network Telemetry
ION	Intelligence Operation Network
IoT	Internet-of-Things
IP	Internet Protocol
ISRS	Inter-channel Stimulated Raman Scattering
IT	Information Technology
ITU	International Telecommunication Union
KPI	Key Performance Indicator
KVI	Key Value Indicator
LiFi	Light Fidelity
LLS	Low Layer Split
MAC	Media Access Control
MAN	Metro Aggregation Network
MAS	Multi-Agent System
MB	Multi-Band
MBH	Mobile Back-Haul
MBN	Multi-Band Network
MB-OXC	Multi-Band - Optical Cross-Connect
MCF	Multi-Core Fibre
MCN	Metro Core Network
MCS	Multicast Switch
MDA	Monitoring and Data Analytics
MFH	Mobile Front-Haul
MIMO	Multiple-Input Multiple-Output

ML	Machine Learning
MMH	Mobile Mid-Haul
mMIMO	Massive MIMO
MPLS	Multiprotocol Label Switching
NBI	North Bound Interface
NCC	Network and Computing Convergence
NCO	National Central Office
NE	Network Element
NFV	Network Function Virtualization
NG	Next Generation
NGC	Next Generation Core
NMS	Network Management System
NOS	Node Operating System
NR	New Radio
O/E/O	Optical to Electrical to Optical
OADM	Optical Add/Drop Multiplexer
OD	Origin-Destination
ODN	Optical Distribution Network
OFC	Optical Networking and Communication Conference
OIF-ENMI	OIF External Network to Network Interface
OLA	Optical Line Amplifier
OLT	Optical Line Terminal
ONF	Open Networking Foundation
ONT	Optical Network Termination
ONU	Optical Network Unit
OpEx	Operational Expenditure
OSNR	Optical Signal-To-Noise Ratio
OSS	Operation Support Systems
OTN	Optical Transport Network
OTT	Over-The-Top
OXC	Optical Cross-Connect
P2MP	Point-To-MultiPoint
PCE	Path Computational Engine
PCEP	Path Computation Element Communication Protocol
PE	P-Edge
PM	Project Manager
PMD	Physical Medium Dependant
PO	Project Officer
PoC	Proof of Concept
PON	Passive Optical Network
POP	Point Of Presence
PPP	Point-to-Point Protocol
PM-16QAM	Polarization multiplexed 16-ary quadrature amplitude modulation
PM-QPSK	Polarization-multiplexed quadrature phase-shift keying
PtoMP	Point-to-Multi-Point
PtoP	Point-to-Point

QMR	Quarterly Management Reports
QoE	Quality of Experience
QoS	Quality of Service
QoT	Quality of Transmission
R&D	Research and Development
RAN	Radio Access Network
RAT	Radio Access Technology
RCO	Regional Central Office
RL	Reinforcement Learning
RMSA	Routing, Modulation and Spectrum Assignment
ROADM	Reconfigurable OADM
RoF	Radio Over Fibre
RRH	Remote Radio Head
RRU	Remote Radio Unit
RTT	Round-Trip Time
RU	Radio Unit
S-BVT	Sliceable Bandwidth/bitrate Variable Transceiver
SC	Steering Committee
SDM	Space Division Multiplexing
SDN	Software Defined Networking
SDO	Standards Developing Organization
SD-WAN	Software Defined WAN
SL	Supervised Learning
SLA	Service Level Agreement
SME	Small and Medium-sized Enterprises
SoA	State of the Art
SOA	Semiconductor optical Amplifier
SONiC	Software for Open Networking in the Cloud
SRS	Stimulated Raman Scattering
STIN	Space-Terrestrial Integrated Network
TCO	Total Cost of Ownership
TDM	Time Division Multiplexing
TIP	Telecom Infra Project
TIRO	Tactile Internet and Remote Operations
UE	User Equipment
UNI	User Network Interface
UP	User Plane
uRLLC	Ultra-Reliable Low-Latency Communication
VLAN	Virtual Local Area Network
VM	Virtual Machine
VNF	Virtualized Network Function
VoD	Video on Demand
vOLT	virtual OLT
vPON	virtual PON
VR	Virtual Reality
VV	Volumetric Video

WAN	Wide Area Network
WB	White-Box
WDM	Wavelength Division Multiplexing
WiFi	Wireless Fidelity
WIM	WAN Infrastructure Manager
WP	Work Package
WSS	Wavelength Selective Switch
ZTN	Zero Touch Networking

EXECUTIVE SUMMARY

Deliverable 5.3 reports on the techno-economic analysis that evaluate the impact of B5G-OPEN solutions for optical network deployments in the access/metro/core segments. These studies are directed towards evaluating specific KPIs defined at the project start, which cover multiple subjects in the B5G-OPEN ecosystem, provided they can be evaluated from a techno-economic standpoint.

The network-wide evaluations, based on optimization tools and simulation/modeling, highlight a number of quantifiable KPI metrics. The use of multi-band networks, enabled by corresponding devices (amplifiers, switching nodes and transceivers) as well as B5G-OPEN control plane solutions, enables metro aggregation optical networks to be deployed with about 30% lower cost, compared to simply consuming additional fibre pairs using only the C-band. This figure tends to go up if the operator cannot easily deploy new fibre and has to lease it. On the operational front, power consumption can be reduced by as much as 90%, when compared to lighting up new fibre pairs, and all the associated terminal equipment/chassis. Furthermore, the extra capacity enabled by multi-band transmission, coupled with advances in the transceiver capacity, allows these metro aggregation scenarios to scale up capacity by a factor of 10. Furthermore, B5G-OPEN demonstrated how critical the optical performance characterization and launch power optimization is when deploying multi-band fibre transmission, such that not only capacity on new bands (e.g. L- and S-bands) is maximized, but also capacity on the existing C-band is not significantly impacted.

Another key aspect of B5G-OPEN is point-to-multipoint transmission, relying on digital subcarrier multiplexing transceivers. These devices allow to adapt the physical devices to hub-and-spoke traffic patterns which are very common in metro aggregation and metro access scenarios. The benefits of employing these devices, as well as designing optical topologies suited to extract their benefits, translate into capital expenditure benefits between 40-50% compared to deploying point-to-point interfaces, as well as around 20% less power consumption due to a more granular adaptation of the subcarriers to the actual required traffic.

B5G-OPEN also proposed to integrate LiFi small cells into its control and service orchestration ecosystem. This deliverable reports on quantifiable power consumption benefits, relative to regular 5G femtocells in the order of 50% less power, while at the same time increasing the throughput over the small cell.

Packet/Optical integration is also a key proposal in B5G-OPEN, which provides new control solutions to deploy and manage optical interfaces in white box switches/routers. In D5.3, we report on the network-level benefits of using pluggable coherent interfaces in routers for optical transmission in metro networks. The number of devices, compared to deploying stand-alone transponder boxes, is similar in scenarios up to a few hundred kilometers, which covers a very wide array of network applications. This way, the cost and operational expenditure of maintaining boxes and chassis solely hosting transponders can be greatly reduced, which makes networks easier to maintain. Based on the study in this deliverable, power consumption reduction in the order of 50% seems achievable through the use of pluggable coherent interfaces in router cards.

Another overarching concept in B5G-OPEN is the massive use of monitoring data to fuel AI/ML applications in various network scenarios. Concretely, B5G-OPEN proposed a complete distributed monitoring platform and data processing infrastructure, which can scale the amount

of processed data ten-fold relative to the state-of-the art. This large-scale monitoring allows more powerful machine learning models to be easily deployed, which can improve network efficiency. In a case study reported here, it is shown how this data monitoring allows for efficient failure prediction analysis of optical devices, which allows not only to reduce the number of hard failures (>70%) by proactively addressing them, but also enables operators to much more efficiently manage and deploy their maintenance teams. Estimated savings of 40% on maintenance support operations are possible by centralizing the support teams, given there is on average more advance warning to deploy the technicians in response to failure events.

TABLE OF CONTENTS

List of Figures

List of Tables

1 INTRODUCTION

This deliverable reports on the techno-economic aspects of the solutions proposed in B5G-OPEN. The network architecture options designed or supported through data and control plane components developed in this project are evaluated in different sets of studies, aiming to demonstrate capital and operational expenditure improvements against the state of the art in optical access, metro and backbone networks.

The results reported here target specific project KPIs, particularly those that cannot be validated through direct experiments and demonstrations but require system level simulation and cost/power modeling. The KPIs are distributed across various areas where B5G-OPEN made tangible contributions: multi-band transmission, point-to-multipoint networking, packet/optical integration in white boxes, integration of Li-Fi access, advanced network monitoring and predictive maintenance. The KPI evaluations resort to a mix of quantitative and qualitative analysis, employing network modeling and optimization frameworks described herein.

The document structure is as follows: Section 2 reports and summarizes on the project KPIs addressed in this deliverable. Section 3 addresses cost, power consumption and capacity benefits of multi-band transmission and P2MP networking in metro aggregation and metro core networks, with a comprehensive planning framework, optical performance characterization and cost model to address various scenarios. Section 4 discusses the power and throughput impact of integrating LiFi cells in the access infrastructure (including the optical Xhaul). Section 5 describes how B5G-OPEN platforms enable an order of magnitude increase in the amount of consumable telemetry by employing distributed monitoring systems and quantifies the benefits of these platforms for an adaptive capacity allocation that reduces overall network power consumption. Section 6 discusses techno-economic aspects related to the benefits of packet/optical integration, specifically by comparing the economics of replacing stand-alone transponder boxes by coherent pluggables integrated in router white boxes, which can be managed and orchestrated through interfaces and modules developed in B5G-OPEN. Section 7 discusses multiple aspects where dynamic networking, enabled by both physical devices and control/management components developed or enhanced through B5G-OPEN, can improve network efficiency. These include predictive failure systems and the impact on network operations from telecom operators' perspective, as well as an evaluation of the impact of P2MP interfaces on network flexibility, and consequently on cost of deployed devices throughout the network lifecycle. Finally, the Conclusion provides a broader overview on how and where B5G-OPEN architecture and components can improve network deployment costs, reduce operating costs, and expand the optical end-to-end infrastructure capacity.

2 KPI VALIDATION

This section lists the project objectives and associated KPIs and details, for the KPIs addressed in this deliverable, how they were achieved and the deliverable Section where they are addressed. For completeness, the full list of KPIs is shown, and the respective deliverable (if not the present one) where they are reported is indicated).

2.1 KPI TABLE

Table 1 shows the project Objectives, respective KPIs, and the deliverables in which their evaluation is detailed. For KPIs addressed in this deliverable, the corresponding Section is included.

Table 1 – List of Project KPIs and deliverables where they are reported.

Objective	KPI	Description	Deliverable(s)
2. Design and validation of an innovative optical transport infrastructure supporting MB connectivity and transparent network continuum from User Equipment to DC.	2.1	Reduction of total power consumption from 30% to 50% with respect to SoA architectures (e.g. H2020 METRO-HAUL results) and legacy solutions	**D5.3 – Section 3.2**
	2.2	CAPEX reduction above 50% in the end-to-end "domain-less" architecture relative to fixed-domain metro-access/regional/core segments	**D5.3 – Section 3.1**
	2.3	KPI Increase of 10x in-service bandwidth w.r.t. currently deployed C-band transport solutions.	**D5.3 – Section 3.3**
3. Design of novel optical network devices for switching amplification and transmission to enable B5G-OPEN solutions and demonstration.	3.1	MB Optical Switching Matrix with bandwidth covering S, C, L and O-band, supporting multiband operation on 50-100 GHz-grid, reducing the overall switching time to < 1 ms, and enabling multiband reconfiguration with added flexibility (dynamicity) in order to improve effective and agile usage of the traffic pipes. The modularity of the architecture will help to scale the node capacity to 3 Pb/s in a pay as it grows approach. Moreover, photonic integrated technology improves the power consumption by 4×…	**D3.3, D5.2**
	3.2	MB filter-less add-drop stage with bandwidth covering at least S, C, L and O-band,	**D3.2, D5.2**

		supporting flexible MB operation based on passive components and thus negligible power consumption.	
	3.3	MB amplification with cumulative gain bandwidth of at least three times the bandwidth of SoA EDFAs, sufficient gain flatness to allow four transmission spans without gain equalization, and gain control response time in the millisecond range.	**D5.2**
	3.4	MB transceivers: Increase the capacity of SoA transceivers up to 2× - 4× by exploiting multiple transmission bands while enabling appropriate slice/band selection according to the network path. Pluggable solutions fully integrated within the white box enabling the removal of stand-alone network elements (e.g. xPonders, OLTs, etc.) to reduce footprint.	**D3.3** **D4.3** **D5.2**
4. Design and validation of next-generation optical access & X-haul for B5G applications enabling massive cost-efficient 5G and Li-Fi small cell deployment.	4.1	50% CAPEX reduction in the X-haul infrastructure compared to NG-PON2, by leveraging on open disaggregated solutions over MB, pluggable technology, and avoiding stand-alone OLT/SBT	**D5.3 – Section 3.2**
	4.2	100x offered capacity increase of fixed-line systems compared to NG-PON2 by leveraging on standardized cost-effective 100GHz channel spacing technology and pay-as-you-grow strategy for MB	**D5.2**
	4.3	50% energy reduction in small cell deployments as of today, by leveraging on power efficient Li-Fi small-cells and AI-based throughput optimization algorithms	**D5.3 – Section 4.1**
	4.4	LiFi handover: QoS-guaranteed handover with minimum throughput higher than 50% of the capacity by predicting the mobility and anticipating flow	**D5.3 – Section 4.1**

		rerouting and parallel delivery to adjacent APs. In case of blockage of the line-of-sight link, the auto-reconnection time < 2× blockage period.	
5. Development of an end-to-end monitoring platform covering the optical MB transmission, switching and the packet layer.	5.1	10x more physical monitored data than what is today available in the field	**D5.3 – Section 5.2**
	5.2	20% OPEX reduction (in combination with O8 and ZTN) by minimizing the power consumption impact of this massive new monitoring platform	**D5.3 – Section 5.3**
	5.3	Accurate measurements over different bands, e.g. < 1.5 dB uncertainty of OSNR measurements.	**D5.2**
6. Design, implementation and validation of an operating system for the novel network elements.	6.1	Flow adaptation/control/monitoring capabilities in the millisecond time scale, enabled by AI prediction and wire-speed P4 operations with no SDN Controller intervention	**D4.3, D4.4, D5.2**
	6.2	Service Provisioning. Multi-vendor operations through fully specified models and APIs, enabling seamless support of optical adaptation functionalities within the packet-optical white box	**D5.2**
	6.3	50% CAPEX reduction by avoiding node solutions designed specifically for the telecom market while leveraging and enhancing white boxes designed for the much wider computing market.	**D5.3 –Section 6**
7. Design, implementation and validation of the service orchestration and infrastructure control system.	7.1	High level service provisioning (e.g. interconnected cloud native functions and containers) relying on low level service setup performed in the sub-second time scale (data connectivity services, leveraging on the MB fully integrated packet-optical infrastructure and supported predictive capabilities)	**D5.2**

	7.2	Reduction of the average setup time for connectivity service by 30% compared to serialized provisioning, exploiting approaches relying on parallelism and concurrency	**D5.2**
	7.3	10x number of controlled devices, based on advanced SDN deployments with microservice-based lightweight virtualization and hierarchical arrangements and device / node abstraction	**D4.2**
	7.4	10x rate of e2e provisioning supported services (e.g. number of requests per hour) leveraging on telemetry-empowered SDN Controller communication across multiple domains of visibility and cluster-based deployments for load sharing between controllers.	**D5.2**
8. Build a framework for an AI-assisted autonomous and dynamic network supporting real-time operations and ZTN.	8.1	Speed of decision-making in the sub-second scale by placing the intelligence near the devices, applying advanced AI/ML techniques, accurate model training based on simulation tools, and knowledge sharing among controllers	**D5.2**
	8.2	Reduce overheads/overprovisioning by >20%, by proactively adapting the capacity to the demand	**D5.3 – Section 7.2**
	8.3	Reduce OPEX by >20%, by increasing autonomous operations and reducing manual intervention	**D5.3 – Section 7.1**
	8.4	Improve and guarantee service and network availability (> 6x9s availability will be reached by combining MB and PtMP with anticipated degradation detection and proactive decision making).	**D5.3 – Section 7.1**

2.2 SUMMARY OF KPI ACHIEVEMENTS IN D5.3

2.2.1 Objective 2 KPIs

Addressing the objective 2 KPIs, this deliverable reports studies on network cost, power and capacity, when employing key technologies proposed and developed by B5G-OPEN such as multi-band transmission, optical continuum and point-to-multipoint transmission.

For KPI 2.1 (Reduction of total power consumption from 30% to 50% with respect to SoA architectures (e.g. H2020 METRO-HAUL results) and legacy solutions), this deliverable reports a study on the power consumption benefits of replacing traditional point-to-point pluggable coherent modules with point-to-multipoint interfaces, which allow to reduce the number of devices needed and the overall power consumption in metro aggregation networks. Depending on the traffic pattern and network topology, the power consumption (and associated CO_2 emissions), can be reduced by up to 89%. For details on the analysis, refer to Section 3.2.

For KPI 2.2 (CAPEX reduction above 50% in the end-to-end "domain-less" architecture relative to fixed-domain metro-access/regional/core segments), Section 3.1, reports a comprehensive study performing network planning in metro-access and metro-core scenarios in order to estimate the cost benefits of deploying multi-band transmission (with standard and super-C and/or L-band). The study uses a tiered classic multi-domain network from a telco and analyzes multiple band options as well as establishing direct communication paths between the different layers/domains.

The analysis estimates a ~70% OpEx benefit over a ten-year exploration period, resulting in a overall CapEx or TCO benefit from multi-band networking (i.e. adding the L-band) of around 30%. As the study demonstrates, this average benefit depends strongly on the fibre leasing costs (where multi-band transmission provides the clearest benefit). Hence, the average CapEx reduction is below the original KPI target, but the >50% benefit target is possible for scenarios/operators that incur higher fibre lease costs.

Addressing KPI 2.3 (Increase of 10x in-service bandwidth w.r.t. currently deployed C-band transport solutions), the expected capacity increase in optical transport networks when scaling to multiple band transmission is evaluated. In Section 3.3, a qualitative and quantitative analysis is presented, detailing the traffic requirements and service granularity from a Telco perspective, as well as a performance analysis on how much capacity is unlocked by transmitting in different bands (since transmission efficiency is smaller in e.g. S/O/E-bands, and transmitting in those bands can also decrease the spectral efficiency of the C/L-band transmission). The analysis indicates that network extensions using C/L/S-bands simultaneously can result in a roughly 3-fold increase in fibre capacity for smaller link lengths (<150km). In this scenario, the increase in channel capacity (relative to state-of-the-art 100G systems), to 400G pluggables produces another 4-fold increase, which can easily reach a x10 service bandwidth increase.

2.2.2 Objective 4 KPIs

Objective 4 addresses KPIs related to improvements in the metro-access and X-Haul infrastructure, including cost/capacity benefits of new transmission devices and architectures, as well as power consumption benefits from LiFi integration.

KPI 4.1 (50% CAPEX reduction in the X-haul infrastructure compared to NG-PON2, by leveraging open disaggregated solutions over MB, pluggable technology, and avoiding stand-alone OLT/SBT) was changed in scope, as NG-PON2 no longer makes sense as a benchmark, due to

reduced relevance in the overall PON market scope. Alternatively, we evaluated CapEx reduction from the use of pluggable P2MP transceivers in the metro-access area, as reported in 3.2 along with the power consumption study. This study shows that the amount of transmission devices required for various topologies is reduced by ~50% when employing P2MP transceivers, while the benefits are maximized when the traffic resembles hub & spoke patterns where point-to-multipoint transmission more efficiently utilizes the available capacity per leaf node.

KPI 4.3 (50% energy reduction in small cell deployments as of today, by leveraging on power efficient Li-Fi small-cells and AI-based throughput optimization algorithms) and KPI 4.4 (LiFi handover: QoS-guaranteed handover with minimum throughput higher than 50% of the capacity by predicting the mobility and anticipating flow rerouting and parallel delivery to adjacent APs. In case of blockage of the line-of-sight link, the auto-reconnection time < 2× blockage period.) are addressed in Section 4.1. It shows how femtocell power consumption is reduced to <5W, entailing a more than 50% reduction relative to regular femtocells. Additionally, the reported throughput increase is also detailed.

2.2.3 Objective 5 KPIs

Objective 5 covers KPIs around monitoring and telemetry capabilities of the network infrastructure and control plane. In the scope of D5.3, we evaluate the impact of these monitoring capabilities.

For KPI 5.1 (10x more physical monitored data than what is today available in the field), Section 5.2 reports how implementing a distributed monitoring platform allows to scale the amount of monitored data more than ten-fold.

For KPI 5.2 (20% OPEX reduction (in combination with O8 and ZTN) by minimizing the power consumption impact of this massive new monitoring platform), an analysis proposing dynamic combining monitoring of granular traffic over each path, with the capabilities of P2MP digital subcarrier allocation, shows the intended 20% power consumption reduction can be achieved.

2.2.4 Objective 6 KPIs

Objective 6 addresses the benefits of integrating optical networking in disaggregated white box routers. For the techno-economic analysis, KPI 6.3 (50% CAPEX reduction by avoiding node solutions designed specifically for the telecom market while leveraging and enhancing white boxes designed for the much wider computing market) is evaluated in Section 6. The scope of this KPI was changed from CapEx to power consumption analysis, since the CapEx analysis is highly dependent on cost figures that vary strongly between different vendors and specific applications. In its place, we propose to evaluate the power consumption of the integration of pluggables into routers, forgoing the need for stand-alone transponder boxes. The simulation framework suggests that 50% power consumption reduction is possible

2.2.5 Objective 8 KPIs

Objective 8 sets targets to evaluate the impact of autonomous network operation on the efficiency of running the infrastructure and service provisioning. Multiple KPIs associated to this objective are evaluated in this deliverable. For KPI 8.2 (Reduce overheads/overprovisioning by >20%, by proactively adapting the capacity to the demand), we present a network simulation/optimization study in Section 7.2 where, with the help of a ML assisted clustering algorithm, the P2MP trees exploiting P2MP transceivers are designed to cover uncorrelated sets

of traffic patterns, thereby maximizing the efficiency of the P2MP architecture. In this scenario, CapEx benefits between 40-50% are achieved.

For KPI 8.3 (Reduce OPEX by >20%, by increasing autonomous operations and reducing manual intervention), a study in Section 7.1 is performed where a service model characterizing the cost of manual interventions for network maintenance is proposed. Through this model, the impact of using predictive failure based on AI/ML is quantified and shown to be in the range of 40-50% OpEx reduction associated to technician interventions.

KPI 8.4 (Improve and guarantee service and network availability (> 6x9s availability will be reached by combining MB and PtMP with anticipated degradation detection and proactive decision making), the analysis (also in Section 7.1) shows how predictive maintenance also allows to reduce the amount of soft-failures becoming hard-failures by more than 70%.

3 TECHNO-ECONOMIC ANALYSIS OF MULTI-BAND AND POINT-TO-MULTIPOINT NETWORKS

This section reports on the cost, power and capacity analysis of the B5G-OPEN network architecture solution for metro networks, when making use of key technological contributions in the project, such as multi-band transmission, direct optical connectivity for services across domains, and point-to-multipoint enabled transceivers.

3.1 COST ANALYSIS

3.1.1 Introduction

The relentless demand for high-bandwidth services and applications in the beyond-5G/6G era necessitates optical networks to provide ample spectral resources to accommodate the increasing traffic loads. This requirement is especially pronounced in metro and regional segments, where a projected traffic compound annual growth rate (CAGR) of over 40%, driven by content delivery network (CDN) traffic concentrated near the end users, threatens to push the fibre capacity to its limits on a number of heavily utilized links in the short to medium term. This limitation cannot be circumvented despite the utilization of spectrally efficient modulation formats designed for short-distance transmission. Thus, it is imperative to explore migration strategies to solutions that allow expanding spectral resources beyond the current usage of the extended C-band (4.8 THz). In this section, we present a comprehensive evaluation of multi-homed edge-to-core routing, modulation-level selection, and spectrum assignment simulations conducted over reference metropolitan area networks (MANs) by leveraging on a novel network planner called 6D-MAN which we have developed to adapt to heterogeneous multi-layer networks based on multi-band and multi-fibre transmission. Our simulations consider coherent transmission with flexible modulation format transponders operating at capacities ranging from 100-400 Gbps on the 50-GHz grid and explore link-by-link migration strategies restricted to the C+L-band, ensuring optimal performance in terms of the generalized signal-to-noise ratio (GSNR). The obtained results demonstrate that deploying L-band equipment on a selected number of links effectively extends the lifespan of existing networks, enabling congestion-free operation with minimal intervention.

In their entirety, our findings underscore the importance of contemplating alternative spectral resources beyond the conventional C-band. They unequivocally accentuate the potential of L-band equipment strategic deployment to tackle capacity constraints in MANs, resulting in a 60% reduction in fibre length and a remarkable 45% decrease in new fibre-pair link deployment needs. The profound implications of efficient fibre capacity utilization manifest themselves in substantial OpEx and optical total cost of ownership savings, amounting to approximately 71% and 17-27%, respectively, over a ten-year period. This research provides valuable insights for MAN operators seeking sustainable strategies to support the growing demands of future beyond-5G/6G services.

3.1.2 Motivations

Conventional optical transport networks, which primarily operate within the C-band spectrum, are facing challenges due to the increasing data demands from new services. To address this, telecom operators are exploring two key strategies: expanding either the spectral or spatial dimensions. Expanding the spatial dimension, while leveraging established C-band technology,

is currently limited by the lack of commercially available network elements that can handle multiple spatial planes and the additional costs associated with multi-core or few-mode fibres. On the other hand, expanding the spectral dimension avoids the need for new fibre deployments by utilizing untapped spectral resources beyond the C-band. However, this requires advancements in both hardware (e.g., multi-band Bandwidth Variable Transponders, amplifiers, dynamic gain equalizers) and software to manage issues such as the Stimulated Raman Scattering (SRS) effect.

Telecom operators must weigh factors like fibre availability, network topology, and operational issues to determine the most cost-effective expansion strategy. Two potential approaches include deploying multi-band/multi-fibre solutions from the start or adopting a pay-as-you-grow (PAYG) scheme, with studies suggesting the latter as the more cost-effective strategy. While most research has focused on backbone networks, there is a need to explore these strategies in Metro Area Networks (MANs), which are experiencing rapid traffic growth due to high-bandwidth applications. Therefore, this study investigates practical mid-term migration strategies for C+L-band/multi-fibre network solutions in MANs compatible with a PAYG approach. The 6D-MAN tool developed for this purpose is designed to optimize routing, spectrum allocation, and cost efficiency while ensuring fully disjoint primary and secondary paths. The study proposes three migration strategies: (i) C+new fibre pair (NFP), (ii) C+Super C+NFP, and (iii) C+Super C+L+NFP. These strategies are evaluated for their suitability in MANs, with an emphasis on seamless migration from C-band to multi-band and multi-fibre configurations.

This study is structured to first introduce the network architecture and traffic engineering model, followed by an exploration of the three migration scenarios. It then delves into the details of the 6D-MAN planning tool and its cost model, before validating the tool with simulations based on real network data. Finally, the results are compared to assess the performance of the proposed migration strategies, leading to the conclusions of the study.

3.1.3   Hierarchical optical MAN

Before exploring migration scenarios and the algorithms for deploying the 6D-MAN planning tool, let's start with an overview of the network and node architecture, and traffic engineering in real-world hierarchical MANs.

3.1.3.1   *Network Architecture*

This study examines a multi-layered, multi-homed hierarchical MAN. As detailed in [Rap22], the network architecture features five levels at the IP layer (see Figure 1(a)), with a focus on the four highest levels (HL1, HL2, HL3, and HL4) in this research (see Figure 1(b)). HL1 nodes interface with external providers and the Internet. HL2 nodes connect HL3 aggregation nodes to HL1 nodes and also host data centers. HL4 nodes aggregate traffic from HL5 nodes or local offices, while HL5 nodes handle traffic from the access network.
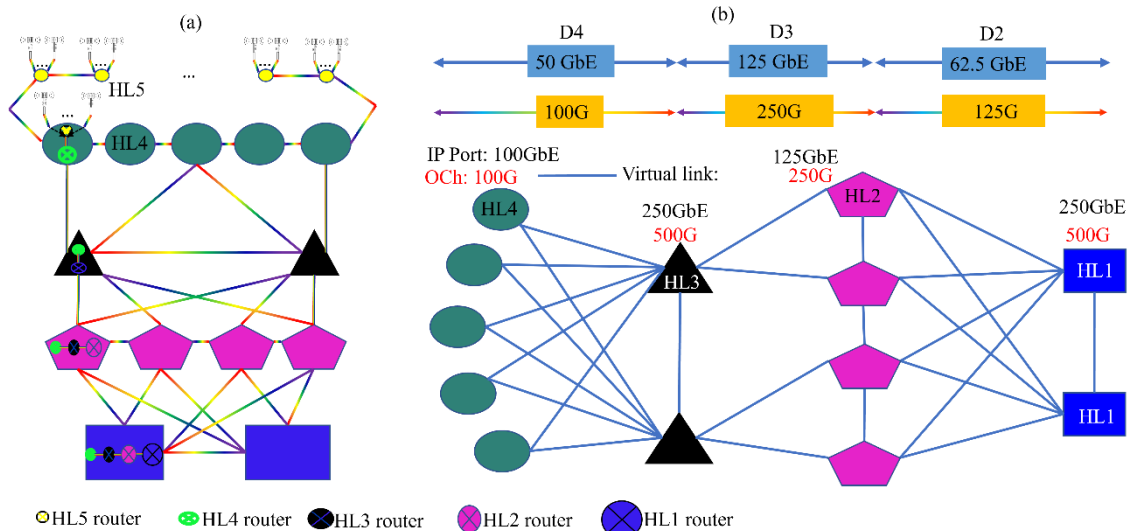
Figure 1: Illustrative physical (a) and logical (b) connectivity across the nodes of a hierarchical MAN. Optical channel (OCh) capacities in red indicate the maximum node aggregated traffic in the event of a single link or node failure. Dd: domain d, HLh: node with hierarchical level h.

Unlike previous studies on MAN network planning, such as [Rap22], this approach considers the traffic of lower HL routers within higher HL nodes. As shown in Figure 1(a), each node typically includes routers that aggregate traffic from the lower HL domain. For example, HL5 nodes can be co-located with HL4, HL3, HL2, and HL1 nodes, serving as hubs. For simplicity, HL5 nodes are not included in our study, as depicted in Figure 1(b); instead, their presence is indicated within HL4 nodes to illustrate the co-location concept more clearly.

The network's physical topology is segmented into three parts: access rings/partial meshes, the metro meshed network (connecting HL3, HL2, and HL1), and the final aggregation stage (linking HL2 and HL1). The IP logical topology is divided into three domains (D4, D3, and D2), with logical links connecting HL nodes to their lower-level hubs, facilitating IP traffic transmission and employing multi-homed aggregation, as illustrated in Figure 1. In the example provided in this figure, the D4 domain features a horseshoe-shaped physical topology with five HL4 nodes connected via 100GbE virtual links to two HL3 nodes. The D3 and D2 domains use a photonic mesh for their physical topology, aggregating traffic as it moves from HL4 to HL1 nodes. Redundancy is incorporated to ensure survivability against failures in either the IP or optical layers. This is demonstrated in Figure 1 as follows: (1) in D4, each HL4 node is linked by two 50GbE virtual links, with optical layer survivability supported by 100G LAND PSP; (2) in D3, each HL3 node has two 125GbE virtual links, supported by two 250G OChs; and (3) in D2, each HL2 node features two 62.5GbE virtual links, supported by two 125G OChs. In this setup, the aggregated traffic totals 250GbE at the HL3 nodes, 125GbE at the HL2 nodes, and 250GbE at the HL1 nodes.

3.1.3.2 Node architecture and traffic grooming

To enable flexible cross-layer service provisioning, this research assumes the node architecture shown in Figure 2(a). In all domains, optical nodes are equipped with colorless, directionless, and contentionless (CDC) reconfigurable optical add-drop multiplexers (ROADMs). Additionally, the network includes a sufficient number of gray clients and colored line transceiver (TRx) interfaces or BVTs. The variable TRx interfaces operate under a license-based client port

activation scheme, and these interfaces are integrated into the optical terminal or Xponder, which may or may not include an Optical Transport Network (OTN) switch fabric.
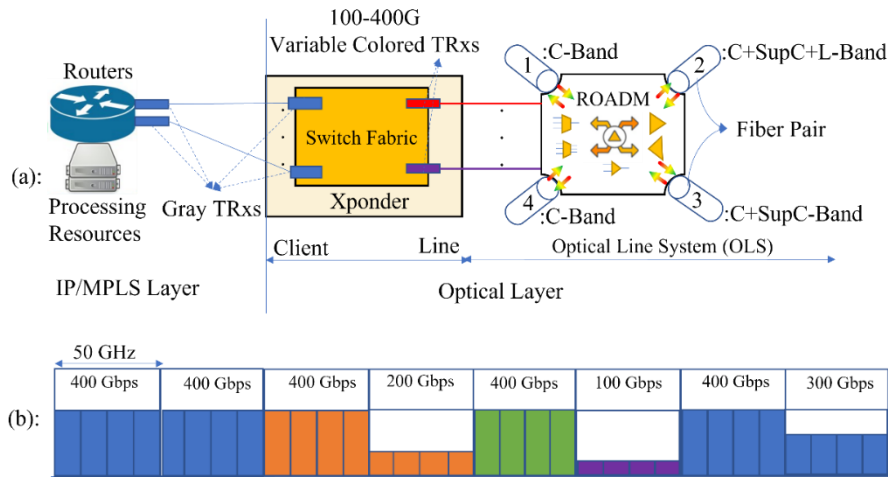
Figure 2: a) Node architecture. (b) Optical channel plan on the 50-GHz fixed grid based on a 100G license PAYG scheme.

The gray client interfaces of the Xponder connect with the IP/MPLS layer, enabling routers to transmit or receive aggregated flows to and from the optical line system (OLS). This setup ensures efficient communication and data exchange between the IP/MPLS and optical layers, leading to seamless integration and optimized performance. This study employs a multi-period planning strategy to accommodate evolving traffic patterns. The initial traffic pattern and its growth rate are assumed to be known by the telecom provider, allowing for annual adjustments to the line interface bit rate through license activation to meet changing traffic demands. The proposed algorithms address both fixed-grid and flex-grid channel spacing scenarios, though this study focuses on the fixed-grid scenario, as shown in Figure 2(b). The line interfaces considered are commercial BVTs with tunable baud rates and modulation format cardinality (MFC), though they are assumed to operate at the maximum baud rate by default to accommodate future capacity growth and minimize the number of BVTs needed. The MFC is selected based on the Quality of Transmission (QoT), specifically the Generalized Signal-to-Noise Ratio (GSNR). For example, Figure 2(b) shows the allocation of BVTs in an OLS for various demands, where four BVTs are assigned to the blue demand. Three of these BVTs have fully activated licenses, while the remaining one has three licenses activated to handle the traffic demand.

BVT allocation is determined based on the observed traffic demands each year. For instance, if an HL4 node has an initial traffic demand of 100 Gbps in year 1, with a fixed CAGR of 40%, the traffic volume is projected to reach 384.16 Gbps by year 5. To meet these demands, the telecom provider deploys a 400G BVT in year 1, which includes 100G capacity. During that year, the first additional 100G license is activated, and subsequent licenses are scheduled for activation in years 2, 4, and 5. No licenses are needed in year 3 as the traffic volume for that year is only 196 Gbps. This approach ensures that bandwidth resources are adequately available in line with evolving traffic requirements over the planning horizon. To optimize resource utilization and minimize the need for new BVT deployments, annual traffic grooming operations are performed on the Xponder's switch fabric (if equipped). For example, by year 6, if the cumulative traffic demand reaches 537.8 Gbps while the existing BVT capacity from year 5 is 15.84 Gbps (400G - 384.16 Gbps), a second 400G BVT and a fifth 100G license are required to handle the additional

137.84 Gbps of traffic. Efficient traffic grooming and resource utilization help the telecom provider manage evolving traffic demands without unnecessary additional BVT deployments.

3.1.3.3   Network and Traffic Engineering Modeling

This section provides a comprehensive explanation of the network and traffic engineering modeling for multi-homed and multi-layer hierarchical MANs, considering both primary routers and co-located lower HL routers. Building on the network architecture discussed in Section 2, the hierarchical optical MAN under investigation comprises seven distinct subsets of IP nodes: N_4, N_3, N_2, N_1, N_{4c}, N_{3c}, and N_{2c}. These subsets correspond to HL4, HL3, HL2, and HL1 nodes, as well as the co-located HL4, HL3, and HL2 nodes, respectively. The network topology can be represented as G(N, L), where N denotes the set of nodes (or vertices) and $L \subseteq \{(i, j) \mid i, j \in N$, and $i \neq j\}$ represents the set of links (or edges). The node set N can be divided into subsets based on hierarchical levels, denoted as Nh, where $h \in H = \{1, 2, ..., |H|\}$, and the overall set N is the union of these subsets, excluding co-located nodes. Specifically, $N_{4c} = N_3 \cup N_2 \cup N_1$, $N_{3c} = N_2 \cup N_1$, and $N_{2c} = N_1$, as illustrated in Figure 3.
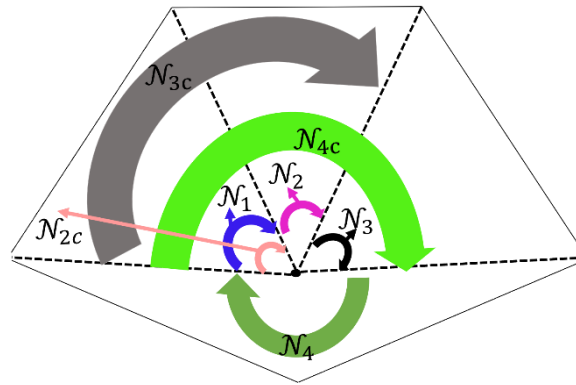
Figure 3: Venn diagram of the nodal sets.

In contrast to the simplified model shown in Figure 1, a real-world MAN accounts for the geographical distribution of different node types in urban areas. HL nodes are not exclusively virtually connected to HL(h-1) nodes; rather, they can be physically or virtually linked to various HL(h−m) nodes, where $1 \leq m < h$, due to the co-location of lower HL routers within higher HL nodes. For instance, Figure 4 demonstrates a hierarchical optical MAN with eight nodes, two from each HL category. The topologically equivalent network at the optical layer (layer zero) is shown in the top-left corner of Figure 4.

No	Node		Router		OCh bit rate	IP Flow bit rate	P/S
	Source	Destination	Source	Destination			
1	1	2	HL4	HL3	100G	50G	P
2	1	3	HL4	HL3	100G	50G	S
3	2	2	HL3	HL2	50G	25G	P
4	2	4	HL3	HL2	50G	25G	S
5	3	3	HL3	HL2	50G	25G	P
6	3	5	HL3	HL2	50G	25G	S
7	2	3	HL2	HL1	33G	12.5G	P
8	2	5	HL2	HL1	50G	12.5G	S
9	3	3	HL2	HL1	33G	12.5G	P
10	3	5	HL2	HL1	25G	12.5G	S
11	4	5	HL2	HL1	50G	12.5G	P
12	4	3	HL2	HL1	33G	12.5G	S
13	5	5	HL2	HL1	25G	12.5G	P
14	5	3	HL2	HL1	25G	12.5G	S

HL4 router ●
HL3 router ●
HL2 router ⊗
HL1 router ⊗

HL1's node: ■ , HL2's node: ⬟ , HL3's node: ▲ , HL4's node: ●

Figure 4: An illustrative example for hierarchical multi-layer traffic engineering in an optical MAN

13

In this example, the top-left HL4 node (node 1) does not have optical connections to the HL3 nodes but is directly connected to an HL2 node (node 2) and an HL1 node (node 3). As discussed in Section 3.1.3.1, traffic survivability is ensured through a multi-homed approach, where an HLh node's traffic demand is serviced by at least two HL(h−m) nodes, with 1 ≤ m < h. Using shortest path routing, nodes 2 and 3 serve as primary and secondary hubs for traffic flows, as detailed in the table on the left side of Figure 4. In this case, a 100G Optical Channel (OCh) is allocated for both primary and secondary flows to handle 100 Gbps of traffic, dividing the IP flows carried by these OChs into 50G each. The co-located HL3 routers at nodes 2 and 3 act as hubs for these IP flows, with intra-data center optical connections carrying 25G IP flows through 50G OChs from the HL3 routers to the HL2 routers. This chaining process continues until traffic is routed to the HL1 nodes. Ultimately, 100G traffic is routed through two HL1 nodes using link and node-disjoint paths. Notably, using a conventional 1+1 protection scheme would require four times the resources. The proposed survivability approach demonstrates robustness against single fibre cuts. To ensure node failure robustness, two important considerations are made:

Remark 1: The hub of a co-located router in an HLh node cannot be another co-located router in an HL(h−m) node, where h ≤ 3 and 1 ≤ m < 3.

Remark 2: The calculation of OCh capacity in HL nodes (where h < 4) is given by R/(Np − Np-c), where R is the aggregated traffic at the HL2 node, Np is the number of primary and secondary paths connected to the HL1 node in question, and Np-c is the number of paths originating from co-located HL2 or HL3 nodes and routed to the HL1 node under consideration.

For example, as shown in Figure 4, despite the proximity of node 3 to node 2, the hub for the co-located HL3 at node 2 must be the HL2 router at node 4 rather than the co-located HL2 at node 3. Choosing the latter would only reroute 50% of the original traffic (100 Gbps) in case of a failure at the top HL1. To illustrate Remark 2, if the OCh capacity for all flows were set to 25G, a failure at the HL1 would result in the complete loss of the original traffic. For instance, a failure at the bottom HL1 would affect the 25G flow from flow 14. If other OChs had a 25G capacity, only two-thirds of the traffic would survive. Thus, to ensure traffic survivability, OChs with a capacity of 33G should be considered for flows 7, 9, and 12.

3.1.4   Migration strategies

In this section, we will thoroughly examine three seamless PAYG migration scenarios designed for MANs. These scenarios facilitate the transition from C-band to Super C+L-band and multifibre configurations. This investigation analyzes three migration strategies over a 10-year period, considering current technologies. These strategies are (as defined in 3.1.2): 1) C+NFP, 2) C+SupC+NFP, and 3) C+SupC+L+NFP. In the C+NFP strategy, the Telco initially uses the C-band (4.8 THz) and progressively leases additional new fibre pairs (NFP) as traffic demands increase over the years. The second strategy, C+SupC+NFP, involves upgrading the Xponders and Optical Line Systems (OLSs) to support the Super C (SupC)-band, which provides a total bandwidth of 6 THz, in the necessary nodes and links. Once the SupC-band bandwidth proves insufficient to accommodate rising traffic, the telco then leases additional NFPs. The third strategy, C+SupC+L+NFP, begins with the deployment of the Super C-band in the required nodes and links. Following this, the nodes and links are upgraded to support the L-band, which adds another 6 THz of bandwidth, resulting in a total bandwidth of 12 THz per fibre pair. If the upgraded Xponders and OLSs still cannot handle the traffic growth, NFPs are then deployed. Figure 2(a) illustrates the architecture of a node in a network scenario where heterogeneous links coexist, with some operating in the C-band, others in the C+SupC-band, and some in the C+SupC+L-band.

3.1.5   6D planning tool for hierarchical optical MAN

This section explores the complexities of the 6D-MAN planner tool, which is utilized for multi-layer, multi-band, multi-homed, and multi-period service provisioning. The tool's functionality is grounded in the traffic engineering principles and migration scenarios detailed in Sections 3.1.4 and 3.1.3.

3.1.5.1   Comprehensive Overview

We introduce a state-of-the-art approach to multi-period planning through the "6D-MAN planner," a sophisticated six-dimensional (6D) tool designed to tackle essential tasks for the next-generation hierarchical optical MAN, which will underpin the upcoming 6G wireless network. As depicted in Figure 5, the 6D-MAN planner integrates six critical functions, or dimensions, integral to the 6G network's backhaul infrastructure. These functions are: (1) multi-homed link and node disjoint (LAND) routing, (2) Quality of Transmission (QoT) estimation, (3) spectrum and band assignment, (4) fibre pair selection, (5) cost analysis, and (6) multi-period IP and optical planning. By incorporating these elements into a unified framework, the 6D-MAN planner provides a comprehensive solution for enhancing network performance and efficiency.
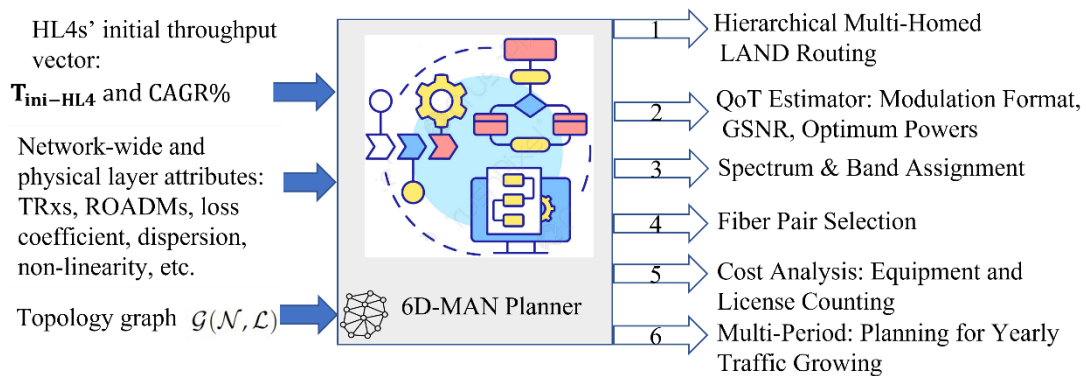
Figure 5: 6D-MAN planner abstract.

To begin the planning process, the 6D-MAN planner requires three essential inputs: Firstly, the initial throughput of HL4 services at the start of year one, denoted as $T_{ini-HL4}$ = [t1, t2, t3, ..., $t_{|N4|}$ + $t_{|N4c|}$], where ti represents the initial throughput of the ith HL4 node. Secondly, it needs network-wide and physical layer parameters, including details about muxponders and/or transponders (Xponders), ROADMs, and link parameters such as loss, dispersion, and non-linearity coefficients. Finally, the network's topology graph is necessary for a thorough analysis of its structure. Using pre-processing and core algorithms, the 6D-MAN planner produces outputs that reflect the network's characteristics across the six dimensions shown in Figure 5. These outputs offer valuable insights for network optimization and support informed decision-making. The flowchart of the 6D-MAN planner, illustrated in Figure 6, outlines its 17 distinct steps, divided into two phases: preliminary manipulation (Steps 1-5) and principal operations (Steps 6-17). Each phase is crucial for the planner's functionality, with the initial steps establishing a robust foundation for subsequent analyses and optimizations within the 6D-MAN framework.
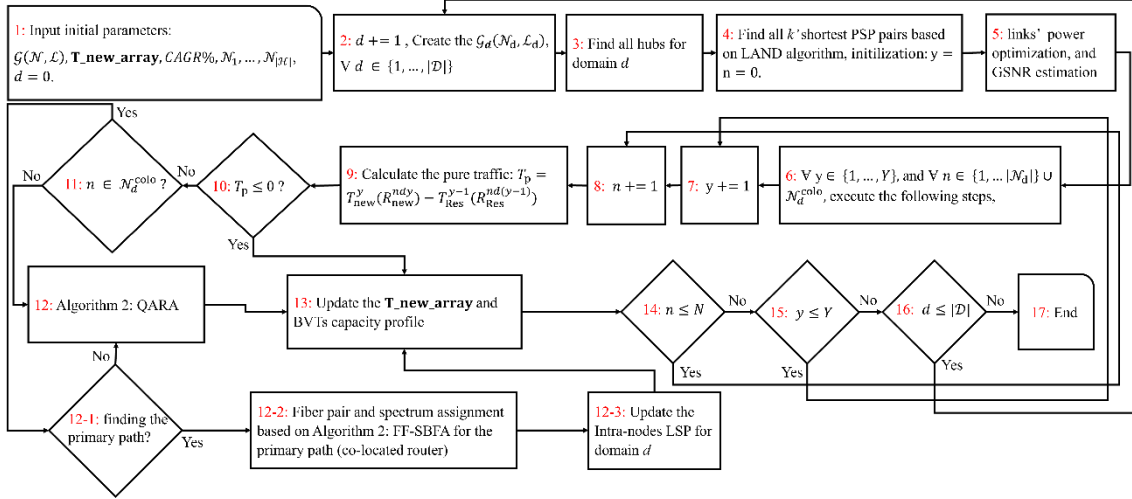
Figure 6: The proposed heuristic algorithm for 6D-MAN Planner.

3.1.5.2 Preliminary Manipulation

3.1.5.2.1 Initialization: Input Parameters

The 6D-MAN planner begins with Step 1, where key elements are assembled to set the stage for subsequent analyses. This step involves integrating several crucial components, including the network's topology graph, denoted as $G(N, L)$. Essential data are then incorporated into the planner, such as the nodes' throughput profile array, represented as $T\_new\_array(y) = = T_{New}^{y}(R_{New}^{nhy})$. This array captures the projected traffic patterns for all nodes and domains over the initial year and the following years. Here, R_{New}^{nhy} denotes the newly forecasted traffic demand for node n in HLh for year y. For these estimates, real-world traffic profiles from year 1 and the fixed $CAGR$ in percentage, as reported by Telco (Telefonica), are used for future projections. Additionally, the initial throughput vector for HL4 nodes, $T_{ini-HL4}$, is included in the $T_{New}^{y=1}$ matrix, which is a $|N| \times |H|$ matrix. In this study, with $|H| = 4$, the assignment is specified as $T_{New}^{y=1}(R_{New}^{n41}) = T_{ini-HL4}^{T}, \forall n \in N$ where $[.]^{T}$ denotes the matrix transpose operator.

3.1.5.2.2 Network Partitioning: Sub-Graph Creation and Hub Identification

The multi-homed architecture proposed ensures traffic flow continuity even in the event of a single fibre cut or node failure. However, when traffic from lower HL domains depends on links within higher HL domains, this traffic's survivability can be compromised if a fibre cut occurs in the higher HL domain. To address this, we introduce a partitioning approach that divides the network into $|H| - 1$ isolated domains. This strategy ensures that traffic originating from lower HL nodes is aggregated at designated hubs, or gateway nodes, within their respective domains. This partitioning enhances traffic management and network resilience.

In Step 2, we create sub-graphs for each domain, denoted as $G_d(N_d', L_d')$, following Eq. (1). Here, $N_d' \subset N$ and $L_d' \subset L$ represent the sets of nodes and links in domain d (e.g., domains D2, D3, and D4 in Fig. 1 correspond to d=2, 3, and 4, respectively). According to Eq. (1), a link between two nodes is removed from the original graph if neither node belongs to N_h (e.g., the link between nodes 6 and 7 in Figure 7 is removed from the sub-graph of domain *d=4*). The sub-graph $G_d(N_d', L_d')$ includes nodes from the hth level and some or all nodes from {h' ∈ H | h' < h}, where *h = d*. The adjacency matrices of domain d and the original network are denoted by $A_{G_d}(a_{ij})$ and $A_{G}(a_{ij})$, respectively, where a_{ij} equals 1 if node *i* is connected to node *j*, and 0 otherwise.

$$A_{G_d}(a_{ij}) = A_G(a_{ij}) \text{ if } i \in N_d \text{ or } j \in N_d \quad \forall i,j \in N$$

$$A_{G_d}(a_{ij}) = 0 \text{ otherwise} \qquad (1)$$

In Step 4, we determine the k-shortest Primary and Secondary Paths (PSPs) between the HLh nodes and the hubs within the corresponding domain. To expedite this process, we first identify the list of hubs for each domain in Step 3, as per Eq. (2),

$$H'_d = N'_d - N_h, \forall h \in H, d \in D \quad (2)$$

3.1.5.2.3 Path List Creation: Link and Node Disjoint (LAND) Algorithm

As detailed in 3.1.3, multi-homed traffic engineering at the IP/MPLS layer requires each lower HL node to be connected to at least two higher HL nodes via virtual links. To ensure full survivability in the event of a single fibre cut, it is crucial for both primary and secondary paths (PSPs) to be link and node disjoint (LAND) at the optical layer. Figure 7 illustrates an example where node 2 (HL4) is linked to an HL1 node (node 6) and an HL2 node (node 7) through three separate paths. Note that the link between nodes 6 and 7 is not usable as it belongs to the higher domain.
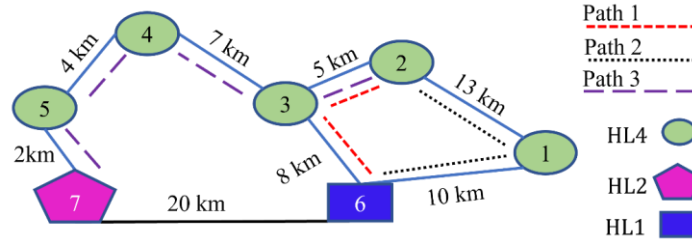
Figure 7: Illustrative example for finding the link and node disjoint primary and secondary paths for domain d=4.

In previous work [Lar19], an algorithm was proposed to find LAND primary and secondary paths (PSPs) by selecting the shortest path based on a specific metric, such as minimum hops, and then removing the links and nodes of the primary path from the original graph. This method, however, can lead to a disconnected graph, making it difficult to identify a viable secondary path. To address this issue, the authors introduced a partial link and node disjoint algorithm, where Path 3 was designated as the secondary path. Another study [Rap22] proposed a different approach to prevent graph disconnection by artificially increasing the cost of the primary path, setting link lengths to 1,000 km. This approach selected Path 2 as the secondary path, employing link disjointness and partial node disjointness for PSPs. In this paper, we introduce the LAND algorithm, which identifies PSPs with complete link and node disjointness. Using LAND, Path 2 and Path 3 are designated as the primary and secondary paths, respectively.

Algorithm 1 outlines our method for implementing the LAND algorithm. It processes a graph representing a domain-d graph and a list of hubs to generate pairs of primary and secondary paths in an array called ***PSP_array*** for each lower HL node within the domain. In line 3 of Algorithm 1, all k-shortest path (k-SP) routes between each node-hub pair are precomputed and stored in a 3D array known as ***3DKSP_array***. This array contains 2D arrays, referred to as ***2DKSP_array***, detailing the attributes of each node-hub's k-SPs, including lists of nodes and links, lengths, and hop counts. From lines 4 to 19, the algorithm examines each node (*n*) and selects LAND PSPs based on the k-SPs related to the corresponding node-hub pair. These PSPs are then sorted in ascending order based on the total hop counts of the primary and secondary paths. Algorithm 1's pseudocode provides a comprehensive description of the steps involved in generating all LAND PSPs (i.e., k') for a given node-hub pair from the associated k-SPs.

Algorithm 1: LAND

1: **procedure** LAND(domain d graph: $G = (N_d', L_d')$, H_d'; $\forall\, d \in D$
2:   Create a ***PSP_array*** to hold the results of the procedure
3:   Calculate k-shortest paths (k-SPs) based on Dijkstra's algorithm between all lower HL nodes and the hubs in domain d and create the 3D array called ***3DKSP_array*** that includes all attributes of the (*k*-SPs), i.e., nodal list, length, hop counts, and link list in a 2D array called ***3DKSP_array*** and ***2DKSP_array***
4:   **for** $n \in N_d$ do
5:       Extract all *k*-SPs between node *n* and the hubs from ***2DKSP_array***
6:       Create primary list (P_n) for node *n* by sorting the SPs in an ascending order based on the hop counts ▷ if the number of hops is the same the length breaks the tie.
7:       Counters initialization: *PSP_Ctr* ← 0, *Pri_Ctr* ← 1
8:     **while** *Pri_Ctr* ≤ |P_n| do
9:         Create a secondary path list (S_{Pri_Ctr} = P_n - *Pri_Ctr*) for primary path *Pri_Ctr*
10:         Secondary counter initialization: *Sec_Ctr* ← 1
11:       **while** *Sec_Ctr* ≤ | *Pn* | do
12:           Extract all attributes of path *Sec_Ctr*
13:           **if** the links and intermediate and final nodes of path
               Sec_Ctr ≠ of path Pri_Ctr then
14:           ***PSP_matrix*** ← (*Pri_Ctr, Sec_Ctr*)
15:             PSP_Ctr ← *PSP_Ctr + 1*
16:           *Sec_Ctr* ← *Sec_Ctr + 1*
17:       *Pri_Ctr* ← *Pri_Ctr + 1*
18:   Sorting each ***PSP_matrix***'s pairs in ascending order based on the primary and secondary hop counts, ▷ if the total number of hops is the same, the total length breaks the tie.
19:     Add the ***PSP_matrix*** for node *n* to ***PSP_array***
20: **return** *PSP_array*

3.1.5.2.4   Quality of Transmission (QoT) Estimation and Power Optimization

The Gaussian-noise (GN) model is utilized to illustrate the effects of both linear factors, such as loss and chromatic dispersion, and nonlinear interference (NLI) phenomena, including self-phase modulation (SPM), cross-phase modulation (XPM), and inter-channel stimulated Raman scattering (ISRS), on amplitude and/or phase-modulated optical signals as they propagate through an optical fibre. The GN model is particularly relevant in the context of coherent detection at digital signal processing receivers. Within this framework, the generalized signal-to-noise ratio (GSNR) is derived as a key parameter for assessing QoT. In this study, since the link lengths are under 65.67 km, inline amplifiers are unnecessary. Therefore, the GSNR for a specific channel *i* within link *l* is calculated using the following equation:

$$GSNR^{l,i} \cong \frac{P_{tx}^{l,i}}{P_{ASE}^{l,i}+P_{NLI}^{l,i}} \quad (3)$$

where $P_{tx}^{l,i}$ is the launch power at the start of each link, $P_{ASE}^{l,i}$ is the noise power from the Erbium-doped fibre amplifier (EDFA), and $P_{NLI}^{l,i}$ includes SPM, XPM, and ISRS.

The end-to-end GSNR for a lightpath (LP) is then determined using the incoherent GN model as follows:

$$GSNR_{LP}^i = 10\log_{10}\left[\left(\sum_{l=1}^{N_{link}}\frac{1}{GSNR^{l,i}} + SNR_{TRx}^{-1}\right)^{-1}\right] - SNR_{Pen}^{Filter} - SNR_{mrg}^{Aging} \qquad (4)$$

where N_{link} is the number of links, and other terms account for SNR penalties from transceiver noise, WSS filtering, and aging margins. Channel bandwidth and bit rate are computed using Eq. (5) and Eq. (6), with parameters such as the symbol rate, roll-off factor, FEC overhead, and base frequency slot size. The FEC overhead typically ranges from 20% to 35% in modern coherent transceivers.

$$B_{ch}^{l,i} = \left\lceil\frac{R_s^{l,i}(1+\rho^{l,i})}{B_{Base}}\right\rceil \times B_{Base} \qquad (5)$$

$$R_{ch}^{l,i} = m \times R_s^{l,i} \times \left(1 + \rho^{l,i}\right) \times (1-\theta) \qquad (6)$$

The GSNR threshold for each modulation format level depends on the pre-FEC bit error rate (BER) and is given by Eq. (7).

$$GSNR_{th}^{m'} = m' \times erf^{-1}(2 \times \beta_{FEC}) \text{ for m'=\{1, 2\}}$$

$$GSNR_{th}^{m'} = \frac{2(M-1)}{3} \times erf^{-1}(1.5 \times \beta_{FEC}) \text{ for m'=3}$$

$$GSNR_{th}^{m'} = \frac{2(M-1)}{3} \times erf^{-1}\left(\frac{m'\times\beta_{FEC}}{2\left(1-\frac{1}{\sqrt{M}}\right)}\right) \text{ for m'=\{4, 5, 6\}} \qquad (7)$$

Two significant challenges in the closed-form calculating GSNR are the estimation of GNLI and PEP. The determination of these parameters relies on factors such as the bandwidth of the spectrum and the loss of the link, as outlined in Table 2. In cases where the link loss exceeds 7 dB and the C+SupC, equations (8)/(16) and (28)-(30) from references [Zef21,Pog17] and [Zef21], respectively, offer more accurate estimations for GNLI. However, for scenarios involving low link loss, such as MAN networks, only the closed-form formula in [Zef21] is applicable. Regarding the C+SupC+L-band, two closed-form versions of the ISRS GN-model have been proposed in [Sem19] and [Bug23]. The former is applicable only for the links with more than 7 dB loss while the latter is applicable for all links from 1 km and higher. To address this, we utilized equations (28)-(30) from reference [Zef21] and equation (21) from reference [Bug23], which were specifically designed to provide more accurate estimations of GNLI for C+SupC-band and C+SupC+L-band scenarios, respectively, encompassing both low and high loss link regimes. For the C+SupC-band, PEP is derived from exp{αL}, where α represents the fibre attenuation coefficient, while for the C+SupC+L-band, it is calculated using equations (13)-(16) from [Bug23]. Nonetheless, for a more precise determination of PEP, numerically solving the Raman differential equations [Zef20] can be employed.

Table 2 – The GN-modeled closed-form NLI estimators based on the spectrum and link's loss.

Spectrum	Link loss in dB	
	≥7	<7
C/C+SupC	[Zef21]/[Pog17]	[Zef21]
C+SupC+L	[Sem19]/[Bug23]	[Bug23]

Power optimization is performed using the local optimization for global optimization (LOGO) method, maximizing the total optical channel throughput (OCT) as described by Eq. (8). For the

sake of simplicity, we assumed that the input constellation has an ideal Gaussian distribution in the calculation of OCT [Arp23,Bug22].

$$MAX\ OCT^l = 2 \sum_{i=1}^{N_{ch}} \frac{R_s^{l,i}}{B_{ch}^{l,i}} \log_2\left(1 + GSNR^{l,i}\right)$$

$$s.t.\ C1: GSNR^{l,i} \geq GSNR_{th}^{m'=6},\ \forall i \in C$$
(8)

The simulations focus on a fully loaded 65 km link in different scenarios (C-band, C+SupC-band, and C+SupC+L-band). The optimal power and GSNR remain consistent across C-band and C+SupC-band scenarios, but the introduction of new channels in the L-band significantly impacts performance in the C and SupC bands. Hence, power and gain control mechanisms would be required only if the GSNR drops below the threshold, though this did not occur in our study. Gain flattening filters at the boosters also help achieve uniform power optimization for each link.

The parameter Nch represents the number of channels in each link. To analyze the optimal power and GSNR, we considered a fully loaded link with a length of 65 km for different scenarios: C-band, C+SupC-band, and C+SupC+L-band, as shown in Figure 8. In these simulations, we utilized the values specified in Table II of [Sem19] for conventional single-mode fibres. The average noise figure of the boosters and pre-amplifiers was set to 4.5 dB in the C-band and SupC-band, and 5 dB in the L-band, and SNR_{TRx} = 36 dB [Sou22]. It is worth noting that, as demonstrated in Section 6, optimizing the uniform input power is sufficient for MAN networks. Unlike backbone networks, where pre-tilt equalizers are necessary, MAN networks with average link distances below 20 km do not require pre-tilt equalizers. The 65 km link analyzed in this study represents the maximum link length considered in Section 6.

As depicted in Figure 8, the optimal power and GSNR are approximately the same for both the C-band and C+SupC-band scenarios. This implies that adding new channels in the SupC-band does not affect the already established services in the C-band. However, the introduction of new channels in the L-band has a significant detrimental effect on the performance of existing demands in both the C and SupC-bands. Therefore, the implementation of power and gain control mechanisms would be required only if the GSNR of the established demand falls below the threshold (here, we considered m' = 6). However, it is important to note that such a scenario did not occur in our study. Additionally, the utilization of gain flattening filters at the boosters facilitates the achievement of uniform power optimization for each link.
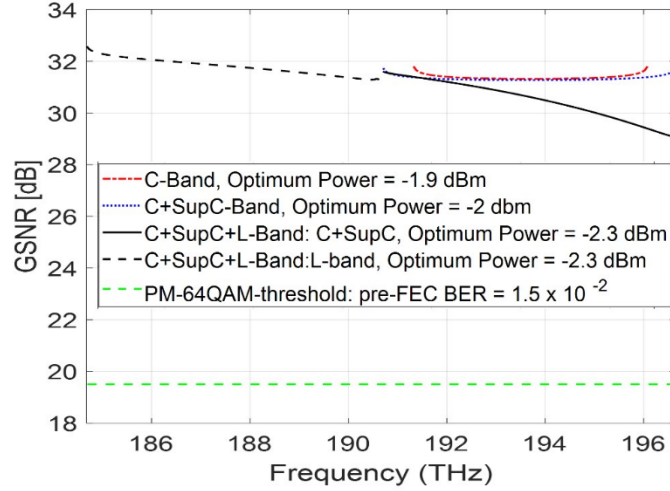
Figure 8: GSNR of all channels for the 65-km link in three scenarios, i.e., C-band, C+C+SupC-band, and C+SupC+L-band.

3.1.5.3   Principal Algorithms

After completing the initial steps, this section focuses on the main functions that establish a pipeline for multi-period QoT- aware PSP, modulation, spectrum, band, and fibre pair assignment. These functions utilize the pre-computed QoT and PSP information obtained in the previous steps as inputs. The resource assignment is then carried out sequentially for all nodes within domain d and year y. The initialization of indices is performed in blocks 6-9 in Figure 6. Subsequently, the pure traffic demand that must be provisioned is conducted in blocks 10-13. In this context, the pure traffic for node n is calculated from Eq. (9) based on the discussions in the previous section and update the throughput profile matrices.

$$T_p = T_{New}^{y}\left(R_{New}^{nhy}\right) - T_{Res}^{y-1}\left(R_{Res}^{nh(y-1)}\right) \tag{9}$$

If $T_p > 0$, it indicates the need for new resource assignments to deploy the new BVT/s and activate new license/s. On the other hand, if $T_p \leq 0$ we proceed to block 13 of Figure 6 to update the nodal traffic profiles and BVT capacities. Moreover, since the secondary paths utilize inter-node links while primary paths utilize intra-node links for low-HL co-located routers, the resource assignments differ for each scenario. Therefore, if the source router is not the low-HL co-located router in the node, algorithm 2 called QoT-aware resource assignment (QARA) is executed to facilitate service provisioning in block 12 of Figure 6. QARA is the main part of the resource assignment. QARA accepts the PSPs and QoT of the channels information pre-computed in the initial steps, the annually pure traffic T_p, number of candidate PSPs k_{PSP}, initial $Cost\_Mat$, and the link state profile array, i.e., $LSP\_array = \left[a^{lij}\right]_{|L|\times N_{ch}\times N_{FP}}$, where $a^{lij} = 1$ if the channel i in the fibre pair j of link l is busy, and 0 otherwise. Additionally, N_{ch} and N_{FP} are the number of channel and fibre pairs (FPs), respectively. It is worth noting that in some cases maybe the number of all PSPs, i.e., k' is less than k_{PSP}, as it is subject to two constraints: link disjointness and node disjointness. For instance, as shown in Figure 7 from three node2-hub (node6 and node7) pairs only one PSP is feasible, i.e., (Path2, Path3). Thus, QARA evaluates the cost of the $MIN\{k', k_{PSP}\}$ PSPs (see line 3 in QARA). As you can see in the following, the cost of each candidate PSP/SP (for the co-located low-HL routers) is stored in a cost matrix (i.e., $Cost\_Mat = \left[C^{ij}\right]_{k_{psp}\times P}$) in line 9 [Arp23c]. In the same way as k_{psp}, the number of columns in the cost matrix depends on the Telco's priorities, denoted as P, where $P \subseteq$

$\{F_{max}, FP_{max}, N_{Hop}, N_{BVT}, GSNR_{mean}^{-1}\}$. Each priority is defined as follows: F_{max} represents the maximum number of channels assigned to the BVTs, FP_{max} indicates the maximum fibre pair usage in km (see Eq. (10)), N_{Hop} represents the maximum number of hops, N_{BVT} denotes the maximum number of BVT usage, and $GSNR_{mean}$ signifies the inverse of the average GSNR of the candidate BVTs. For them, the initial values are infinite.

$$FP_{max} = 2 \sum_{l=1}^{N_{link}} \sum_{d=1}^{D^l(y)} L^l \times \varsigma^{l,d} \qquad (10)$$

where N_{link} is the number of links for PSP/SP, $D^l(y)$ is the maximum number of FP in link l in year y, L^l is the length of link l in km, and $\varsigma^{l,d}$ indicates the presence of an active channel in link l at degree d, where it takes the value of 1 if such a channel exists, and 0 otherwise. After the 100G license calculation in line 2, the subsequent lines (3-12) involve calculating various parameters for all PSPs/SPs. These parameters include the channel number, modulation format, fibre pair number, PSPs/SPs, and the required number of BVT/s for a new traffic demand in node n from domain d in year y. To do so, in line 5, QARA utilizes the first fit spectrum, band, and fibre pair assignment (FF-SBFA) algorithm, which is presented in Algorithm 3 that will be explained in the following. In line 6, the GSNR of the candidate BVT is estimated Equation (4). Then, in line 7, the bit-rate and modulation format of the BVT are identified based on Equation (6). The loop between lines 4-8 is repeated until all traffic demands are established. Therefore, the objective function to find the optimum PSP/SP is defined as follows:

$$MIN(Cost\_Mat) = Cost'\_Mat[1] \qquad (11)$$

Here, $Cost'\_Mat$ refers to the sorted $Cost^M\_at$ in ascending order of Telco's priorities. In the case where two or more candidate PSPs/SPs have the same highest priority, the second, third, fourth, and fifth priorities are considered to break the tie. The LSP_array is updated in line 12 based on the selected PSP/SP, and it will be eventually returned by QARA. Additionally, since QARA has identified the destinations of the aggregated traffic demands, the T_new_array is updated in block 13 of Figure 6 based on the selected PSP/SP. It is important to note that for the primary path of co-located lower-HL routers in each node, we follow the same approach for spectrum and FP assignment. Due to the short distances involved, we assume the utilization of PM-64QAM with a capacity of 400G for each BVT. Furthermore, the counting of FP usage is disregarded in this scenario. The FF-SBFA algorithm (Algorithm 3) uses the LSPs of the candidate path to create the lightpath state profile (LPSP). The state of each LPSP is determined by performing a logical OR operation on the corresponding LSPs. This means that if the state of a frequency slot in at least one link is 1, it indicates that the state of the corresponding frequency slot in the LPSP is also 1. To construct the unit vector (U), the LSP numbers of the LPSP are taken into account. For example, in Fig.9, an LPSP (A → B → C → D) consists of 3 links or LSPs, resulting in U = [111]. This implies that the search for an idle channel begins in the spectrum of the first fibre pair across all three links. If an idle channel that is available in all links is not found, a fibre pair is added to the links.

Assuming each LSP has 8 × 12.5 frequency slots, there are two candidate 50 GHz channels per link. To ensure the minimum deployment of the new fibre pair (NFP), the links are sorted in ascending order based on the number of idle channels (N_{idle}) in each iteration. As depicted in Figure 9, in the first iteration, an idle channel cannot be found due to the fully occupied LPSP. Consequently, in the second iteration, the second fibre pair of link 3 (the most congested with the shortest length) is included to create the LPSP. However, since the LPSP remains fully occupied in the second iteration as well, in the third iteration, the second fibre pair of link 1 is added to form the LPSP. Ultimately, the required idle spectrum to establish a BVT with 50 GHz

can be achieved through the LPSP consisting of the second fibre pair of links 1 and 3, as well as the first fibre pair of link 2. In this case, $flag\_iter$ = 0, indicating that the iteration is terminated and the FF-SBFA algorithm returns the channel and fibre pair numbers for the candidate BVT.
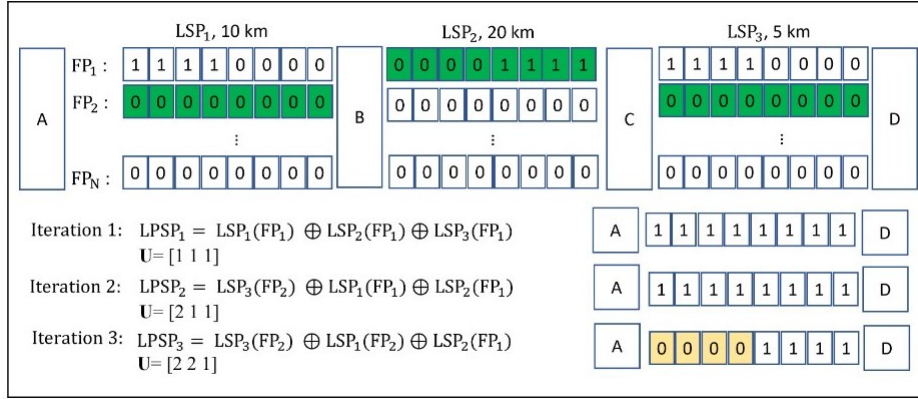
Figure 9: Illustrative example of new fibre pair assignment.

Algorithm 2: QARA

1: **procedure** QARA (PSP_array, pre-computed QoT including GSNR of the channels and the optimum power of each link, k_{psp}, $LSP\_array = \emptyset$, $Cost\_Mat = \infty$ and T_p)

2:    compute the number of 100G license based on $\left\lceil \frac{T_p}{100G} \right\rceil$

3:    for $path\_ctr \in \left[1, MIN\{k', k_{psp}\}\right]$ do

4:       while $T_p > 0$ do

5:          First fit (FF) spectrum assignment and fibre pair selection for PSP/SP (for low-HL co-located routers) based on Algorithm 3,

6:          GSNR estimation based on Eq. (4),

7:          identifications of modulation format and bit-rate of the allocated BVT based on   the estimated GSNR,

8:          $T_p \leftarrow (T_p$–allocated BVT's bit-rate)

9:          update the cost matrix, i.e., ***Cost_Mat***, based on the PSP/SP attributes,

10:           sorting the ***Cost_Mat*** in an ascending order of the Telco's priority/ies,

11:      Select the optimum PSP/SP based on ***Cost_Mat***, ▶ if the costs of some PSP candidates are the same, the second, third, and fourth priority, respectively, breaks the tie,

12:      update the ***LSP_array*** based on the selected PSP/SP, and channel and fibre pair number.

13:      return ***LSP_array***

Algorithm 3: FF_SBFA

1. **procedure** FF_SBFA (LSPs of the candidate path)

2.   create the LPSP of the path,

3.   *flag_iter* = 1

4.   create unit vector ***U[1]*** with size equal to the number of links

5.   **while** *flag_iter* do

6.   find the number of idle channels in LSPP,

7.   **if** an idle channel is found **then**

8.   assign the channel to the BVT,

9.	*flag_iter* ← 0
10.	**else**
11.	sorting the LSPs in ascending order of the links' number of idle channels, i.e., N_{idle}; when some LSPs are the same, the links' length breaks the tie,
12.	update the order of **U** based on the previous line,
13.	**U ← U(1)+1**
14.	update the LSPs and LPSP based on U
15. **return** The assigned channel and fibre pair numbers	

3.1.6 Cost model

Ultimately, this section introduces an all-encompassing cost model for the optical infrastructure of MAN networks across multiband systems. The cost model presented in this paper focuses on the Telco's total cost of ownership (TCO) in the optical-layer, specifically known as optical TCO. Optical TCO comprises two main components: capital expenditures (CAPEX) and operating expenses (OPEX). In our scenario, we consider a non-incumbent operator who seeks to obtain the indefeasible right of use (IRU) for the fibre within the MAN from the incumbent operator. The CAPEX component encompasses the one-time cost of leasing the IRU for the fibre, as well as upfront expenses associated with the right to use a strand per unit of distance per year (e.g., strand/km/year) for a specified duration, typically ranging from 10 to 30 years. Therefore, the annual OPEX cost ($C_{OPEX}(y)$) is calculated using equation Eq. (12), yielding the following expression.

$$C_{OPEX}(y) = 2 \times C_{IRU} \times \sum_{l=1}^{N'_{link}} \sum_{d=1}^{D^l(y)} L^l \times \varsigma^{l,d} \quad (12)$$

where N' link is the number of the network's links. C_{IRU} is the cost unit for IRU in [strand/km/year]. As the cost of leasing the fibre pair is contingent on various factors such as geography, network type, country/city, and contract conditions, we have incorporated three values for this parameter, i.e., 0.5, 1, and 1.5 (see Table 2). These values are derived from Telco reports, reflecting real-world figures observed in two European countries and a Latin American country. Furthermore, the CAPEX component includes the expenses related to the transponders (Xponder) and OLS. As depicted in Fig. 2. (a), the OLS comprises various components of the ROADM, including pre-amplifiers, boosters, wavelength selective switches (WSS), splitters, optical channel monitoring, optical supervisory channel, and embedded optical time-domain reflectometer. The cost units for the CAPEX components are specified in Table 2. In this regard, recently, thanks to advances in WSS technology the concept of ROADM-on-a-blade (RoB) [Inf23] or integrated ROADM (iROADM) [Nok23] has been introduced by the vendors. Indeed, all required components of a ROADM are compacted in a single card, thus reducing both cost and footprint. Therefore, Table 2 presents the CAPEX cost for 1 × 20 CDC RoB, with cost unit C_{RoB}, and 8 × 16 multi-cast switch, with cost unit C_{MCS}, both given as a multiple of the cost of a 100G line bit rate in C-band, encompassing the establishment cost of Xponder components such as BVTs, pluggable modules, client-side interfaces, and switch fabric. In our approach, rather than purchasing fully equipped Xponders, we adopt a licensed model based on the PAYG approach. This allows for more flexibility and cost efficiency by paying for the capacity of BVTs as it is utilized. Therefore, the CAPEX can be calculated using Eq. (13). In addition, the cost model presented in Table 3 is extracted from the Telco reports and we are restricted from revealing the source of these documents.

$$C_{CAPEX}(y) = C_{CMS}(y) + C_{RoB}(y) + C_{TRx}(y) \quad (13)$$

Table 3 - Estimated CAPEX and OPEX values based on the cost unit [c.u], i.e., the cost of a C-band 100G line bit-rate (CTRx=1) includes the licence, xponder, client and line interfaces. RoB: ROADM-on-a-blade, CDC: colorless, directionless, and contentionless, MCS: Multi-Cast Switch

Cost Type	Equipment	Cost [c.u]
CAPEX	100G	C_{TRx} = 1
	200G	C_{TRx} = 1.33
	300G	C_{TRx} = 1.66
	400G	C_{TRx} = 2
	1x20 CDC-RoB	C_{RoB} = 1.9
	8x16 MCS	C_{MCS} = 0.6
OPEX	IRU / Lease [strand/km/year]	C_{IRU} = 0.5, 1, 1.5

Eq. (13) incorporates the following cost factors: $C_{MCS}(y)$ stands for the cost of the MCSs, $C_{RoB}(y)$ represents the cost of the CDC RoBs; and $C_{100G}(y)$ reflects the cost of a C-band 100G line bit-rate ($C_{100G}(y)$) includes the license, Xponder, client, and line interfaces (BVTs) required in the year y. These cost parameters are calculated in accordance with Eq. (14) to Eq. (18). Moreover, in our approach, rather than purchasing fully degree equipped RoB, we deploy the RoB/s in each degree based on the PAYG approach.

$$C_{MCS}(y) = C_{MCS}(y) \times \sum_{n=1}^{|N|} \left[\frac{H\left(N_{port}^{req}(y,n)\right)}{16} \right] \quad (14)$$

where *H(x)* is the Heaviside step function, the value of which is zero for x < 0 and x for x ≥ 0, and $N_{port}^{res}(0,n) = 0$. $N_{port}^{req}(y,n)$, $N_{port}^{res}(y,n)$, and $N_{BVT}^{new}(y,n)$ are the number of required MCS ports exceeding (when positive) or remaining (when negative) in already deployed MCSs, the number of residual MCS ports in already deployed MCSs, and the number of new BVTs that are required based on the new demand, respectively. They can be calculated as follows:

$$N_{port}^{req}(y,n) = N_{BVT}^{new}(y,n) - N_{port}^{res}(y-1,n) \quad (15)$$

$$N_{port}^{res}(y,n) = \left[\frac{N_{port}^{res}(y,n)}{16} \right] \times 16 - N_{port}^{req}(y,n), \text{ if } N_{port}^{req}(y,n) > 0$$

$$or \ N_{port}^{res}(y,n) = N_{port}^{req}(y-1,n) - N_{BVT}^{new}(y,n), \text{ otherwise} \quad (16)$$

$$C_{RoB}(y) = C_{RoB}(y) \times \sum_{n=1}^{|N|} N_{Degree}^{new}(y,n) \quad (17)$$

$$C_{100G}(y) = C_{100G}(y) \times \sum_{n=1}^{|N|} N_{100G}^{new}(y,n) \quad (18)$$

$N_{Degree}^{new}(y,n)$, and $N_{100G}^{new}(y,n)$ are nodal degree, and 100G line bit-rate of node n in year y. As a result, the optical TCO can be derived from Eq. (19).

$$OTCO(y') = \sum_{y=1}^{y'} [C_{CAPEX}(y) + C_{OPEX}(y)] \quad (19)$$

Within the domain of pricing tactics like price skimming, customer-driven pricing, and premium pricing, in conjunction with the progressions in silicon technology, the expense related to state-of-the-art equipment commonly undergoes a reduction after its market launch. Consequently, the parameter β(y) in Eq. (20) serves to capture the fluctuations in the cost of SupC- and L-band

25

equipment over time. Furthermore, γ represents the annual depreciation value for equipment costs. C-band photonics and optoelectronics enjoy the advantages of large-scale production, benefiting from economies of scale that drive down prices for C-band components. Conversely, SupC- and L-band components are currently manufactured in smaller volumes, resulting in higher prices. As a result, there is a premium of 10 to 20 percent for SupC and L-band optoelectronics and photonics, respectively.

$$C_{CAPEX}^{SupC-:L-Band}(y) = \left(1 + \alpha \times \beta(y)\right) \times C_{CAPEX}^{C-Band}(y = 1) \qquad (20)$$

where α = 10% and 20% for SupC and L-band, respectively, and $\beta(y) = (1 - \gamma)^y$, $\gamma = 10\%$, and $y \in \{2, 3, \ldots, Y = 10\}$. Furthermore, γ represents the annual depreciation value for equipment costs. C-band photonics and optoelectronics enjoy the advantages of large-scale production, benefiting from economies of scale that drive down prices for C-band components. Conversely, SupC- and L-band components are currently manufactured in smaller volumes, resulting in higher prices. As a result, there is a premium of 10%–20% for SupC- and L-band optoelectronics and photonics, respectively.

3.1.7 Simulations and results

In this section, we evaluate the performance of the three proposed migration strategies in terms of optical TCO (Eq. (19)). We begin by providing a comprehensive overview of the network characterization. Subsequently, we highlight the key findings related to the operational parameters of the proposed migration strategies, namely C+NFP, C+SupC+NFP, and C+SupC+L+NFP.

3.1.7.1 Simulation set-up

The network topology discussed in this paper (refer to Figure 10) is a Telefónica metro-urban network called MAN157. It consists of |N | = 157 optical nodes, |L| = 220 links, |H| = 4 HLs, and |D| = 3 HL domains. There are two HL1 nodes (represented by blue rectangles), three HL2 nodes (represented by pink pentagons), 33 HL3 nodes (represented by black triangles), and 118 HL4 nodes (represented by green circles). All HL1, HL2, and HL3 nodes have a co-located HL4 node. The simulation setup in Figure 8 utilizes the same physical layer parameters as those examined in this section. Additionally, the pre-SD-FEC BER is assumed to be $BER_{pre-FEC} = 1.5 \times 10^{-2}$ [32].
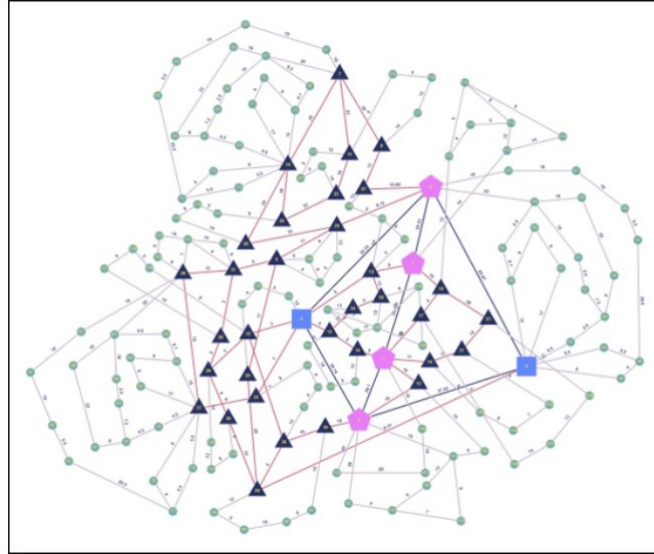
Figure 10: Telefónica metro-urban network (MAN157) topology.

The selected parameters for the bit rate, symbol rate, roll-off factor, channel spacing, and FEC overhead are 100-400 Gbps, 40 GBaud, 0.1, 50 GHz, and 20-35%, respectively. Based on equation Eq. (7), the threshold GSNR($GSNR_{th}^m$) values are as follows: 3.71 dB for PM- BPSK, 6.72 dB for PM-QPSK, 10.84 dB for PM-8QAM, 13.24 dB for PM-8QAM, 16.16 dB for PM-16QAM, and 19.01 dB for PM- 64QAM with cardinality m = 2, 4, 6, 8, 10, and 12, respectively. Furthermore, the C-band, C+SupC-band, and C+SupC+L-band encompassing 4.8 THz, 6 THz, and 12 THz, consist of 96, 120, and 240 channels respectively, with a channel spacing of 50 GHz [Kon19]. A separation of 400 GHz is taken into account between the L-band and the C+SUpC-band. Figure 2(b) illustrates an example of the spectrum profile in this study. Based on 100 Monte Carlo iterations, the initial aggregated traffic at the HL4 nodes is uniformly generated within the range of 20-200 Gbps, with an average of 100 Gbps and a CAGR of 40% according to the Telco reports. The subsequent results in this section represent the average values obtained from 100 independent network simulations utilizing the specified sets of traffic demands. To account for realistic OLS penalties, we consider the following parameters: $SNR\_Pen_{Filter} = 0.3 - 7\ dB$, derived from Figure 4(a) in [Seq18], which depends on the number of traversed hops and the degree number of the nodes; SNR_Pen_{Aging} = 1 dB; and back-to-back SNR_{TRx} = 36 dB, which includes the losses due to connectors, polarization dependence, and MUX/DeMUX insertion.

3.1.7.2   Network Characterization

To support the findings presented in this paper, let us provide some statistical information about the network being studied that is reported by the 6D-MAN planner. Figure 11 illustrates the data regarding link length and nodal degree. The maximum link length is observed in domain 2, spanning 65 km, while the minimum link length is found in domain 4, covering 1 km. As we move from the edge domain towards the core domain, the number of links and nodal degree per node increase in each domain.
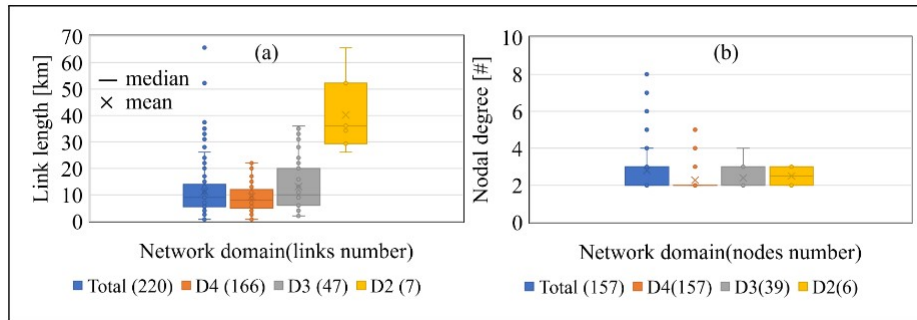
Figure 11: (a) link length in km, and (b) nodal degree number for each network domain. Every domain's legend shows the number of links and nodes in parentheses.

Notably, the highest nodal degree of 8 is attributed to the right HL1 node, as depicted in Figure 10, spanning the entire network. However, in domain 2, its nodal degree is 2. In this topology, the HL3 nodes exhibit the highest nodal degree of 5. On average, the nodal degree slightly exceeds 2 across all domains, while the average link lengths are 8 km, 10 km, and 40 km in domains 4, 3, and 2, respectively. In the following box plots, it is important to note that the cross symbol represents the mean, while the dash symbol represents the median. As shown in Figure 6, the 6D-planner has the capability to provide the attributes of all primary and secondary candidate paths between lower HL nodes and higher HL nodes within the HO-MAN network. These attributes are determined using the k_{PSP}= K shortest LAND pairs algorithm. Figure 12 displays the distances and number of hops for K= 1 and 3. As expected, the secondary paths exhibit longer distances, and more hops compared to the primary paths. The highest values are observed in D3 for K = 1, where the maximum distance is 175 km and the maximum hop count is 11. For K = 3, these values increase to 200 km and 14 hops, respectively. It should be noted that due to limitations in nodal degrees of certain nodes, particularly in D4, all three pairs could not be provided for each HLh-HL($h − m$) (where 1 ≤ m < 4). Additionally, as depicted in Figure 11, the number of links and nodal degrees are higher in D3 compared to D2 and D4, resulting in the longest primary and secondary paths being located in D3. Moreover, there is a difference of approximately 20 km between the average distances of primary and secondary candidate paths in all domains for K = 1. However, in D4, D3, and D2, this difference increases to 30 km, 40 km, and 60 km for K = 3. A similar trend can be observed in terms of the number of hops as well. Overall, the hop counts in D2 are lower compared to other domains, mainly due to the presence of fewer nodes in this domain. These values offer valuable insights into the QoT analysis of each channel on a candidate path, particularly concerning the GSNR and modulation format level. To begin with the power optimization and GSNR estimation analysis, as explained in section 3.B.4, the optimal power for each link is derived from Eq. (8). The migration scenarios for each year consider the fully loaded C-, C+SupC-, and C+SupC+L-bands by applying the dummy noise idlers at ROADMs. For instance, the initial state for all strategies is the C-band, and as the traffic demand increases each year, an extra spectrum is added to the C-band. Figure 13(a) illustrates that the minimum GSNR of all channels for all candidate primary and secondary paths is approximately 29 dB at each link, occurring in D2 for a secondary path. Additionally, the results in Figure 12 confirm that, as expected, the average GSNRs of D4's links are greater than D3's links, which in turn are greater than D2's links.

Furthermore, as discussed in Section 3.1.5, the results in Figure 13(a) show that there is no significant difference between the average GSNRs of the channels in the C-band and C+SupC-band links within each domain. Additionally, since the average and median differences in link lengths between D4 and D3 are less than 3 km (as shown in Figure 11), the corresponding

average GSNRs do not vary significantly across all strategies. However, there are notable GSNR differences of approximately 9.2 dB (7.8 dB) on average between D4 (D3) and D2 links. There is also a slight difference between the average GSNRs of the C(+SupC)-band and C+SupC+L-band due to the ISRS effect. For instance, as depicted in Figure 13(a), this difference is around 0.84 dB and 1.3 dB on average in D4 and D2, respectively. By optimizing the power using the dynamic gain equalizer (DGE), we can ensure a smooth migration from C-band to C+SupC+L-band over a ten-year period. This advantage is largely attributed to the relatively short reach distances in hierarchical MANs and the application of the SD-FEC method, which supports a pre-FEC BER of 1.5×10^{-2}. It is important to note that for lower pre-FEC BER rates (e.g., 4×10^{-3}) supported by HD-FEC schemes, reconfiguring the lightpath, such as altering the modulation format, becomes essential to address the bit rate degradation of the BVTs. Figure 13(b) shows the optimal power levels for each strategy within each domain. It is evident that D2 links require higher launch power due to their greater distances. Moreover, the optimal power for the C- and C+SupC-band links are nearly identical. However, due to increased Nonlinear Interference (NLI), the optimal powers for the C+SupC+L-band scenario are slightly lower than for the C(+SupC)-band. In Figure 13(c), we observe that by incorporating the new spectrum, the throughput of the links (as per Eq. (8)) increases by 33(28) Tbps and 108(103) Tbps for D4(D2) links in the C+SupC- and C+SupC+L-band, respectively.
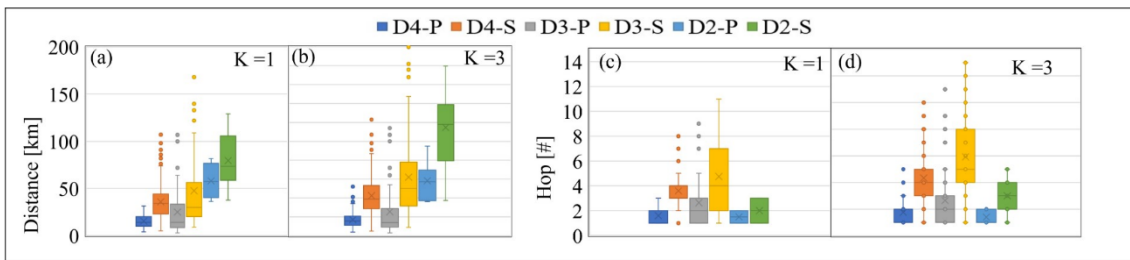
Figure 12: (a) and (b) Primary (P) and Secondary (S) connections' distances in km, and (c) and (d) connections' hops numbers in D4, D3, and D2 domains for K=1 and 3.
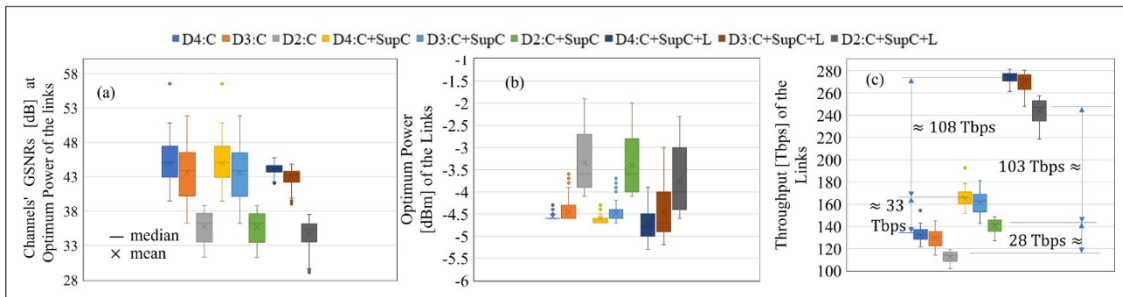
Figure 13: Boxplots of (a) the estimated GSNRs in dB for all channels at all links, (b) the estimated optimum power in dBm, and (c) the throughput in Tbps, for all links in domain D4, 3, 2, and scenarios C, C+SupC, and C+SupC+L.

Nevertheless, it's worth noting that the ISRS effect prevents the throughput from increasing proportionally to the added channels. In the following analysis, we evaluated the QoT of the lightpaths over a span of ten years as we transitioned from the C-band to the SupC- and SupC+L-band. As shown in Figure 14, for both K=1 (Figure 14(a)) and K=3 (Figure 14(b)), the minimum GSNR exceeds the required GSNR for 64-QAM, confirming a seamless migration process.
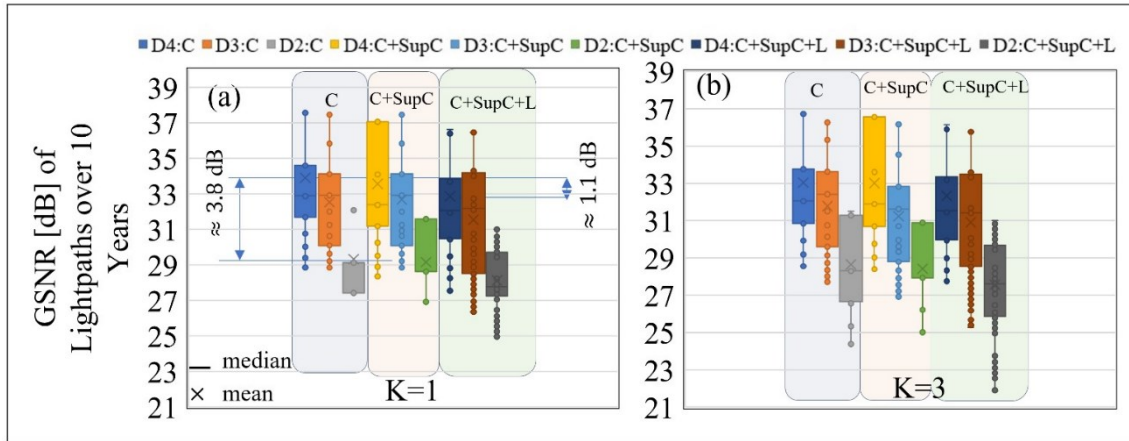
Figure 14: Boxplots of the estimated GSNRs in dB for all established lightpaths over 10 years in HL4, 3, and 2 domains and scenarios C, C+SupC, and C+SupC+L, respectively, (a) K= 1 (b) K=3.

3.1.7.3 Performance Comparison of the Proposed Migration Strategies

Figure 15(a)-(f) reveals a compelling finding: not only can the number of NFPs be significantly reduced by increasing parameter K from 1 to 3, but the deployment time can also be delayed by one year across all migration scenarios. However, caution is advised, as K>3 negatively impacts performance due to constraints from the limited number of PSPs in all domains, especially HL4 and HL2 [Arp23b]. Additionally, a higher K results in longer lightpaths, requiring greater NFP lengths. For example, with K=3, we achieve a 6.8% reduction (equivalent to 391 km) in NFP length and an 8.45% decrease (amounting to 20 links) in NFP links compared to K=1 in the C+SupC+L+NFP scenario. Notably, reducing the number of links is critical since each NFP link requires installing a new optical line system, such as RoB.
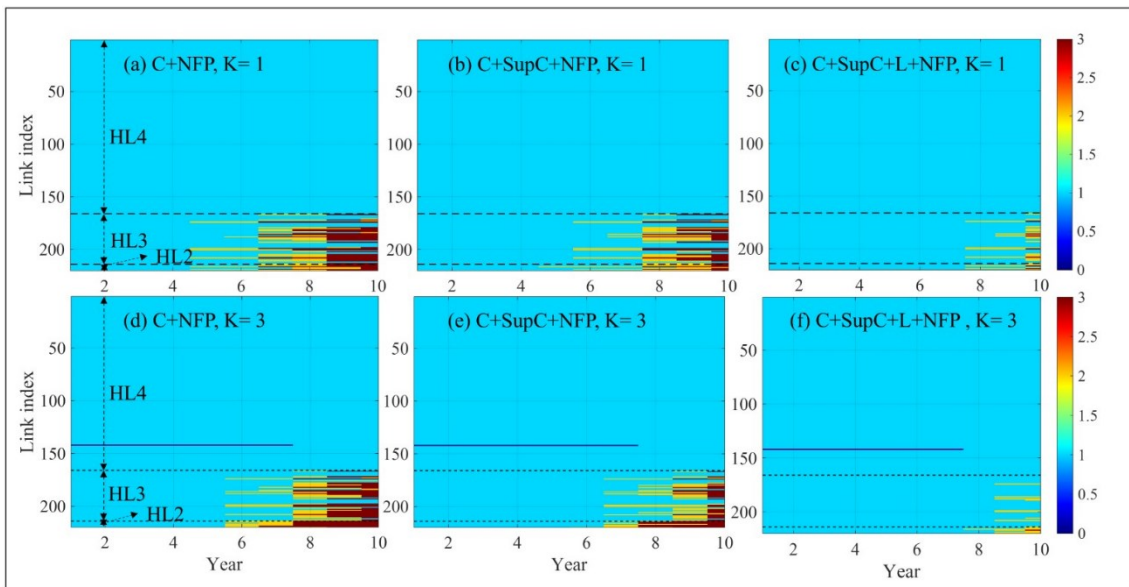
Figure 15: Fibre usage per link over ten years for (a) and (d) C+NFP, (b) and (e) C+SupC+NFP, and (c) and (f) C+SupC+L+NFP for K=1 and K=3, respectively. NFP: New Fibre Pair, C, SupC, and L: C-Band, Super-C-Band, and L-Band, respectively.

Fortunately, the HL4 domain remains resilient, meeting traffic demands over the ten-year period without needing additional spectral bands or NFPs. However, HL3 and HL2 domains require NFPs by years 9/8 in C+SupC+L+NFP with K=3 (see Figure 15(c) and (f)). Remarkably, in these cases,

the C+SupC+L+NFP strategy achieves substantial NFP length (link) savings of 42.8% (29.23%) and 60.9% (45.33%) by year 10 compared to C+SupC+NFP and C+NFP, respectively. However, this comes with the need for SuperC- and L-band BVTs, which impact Capex and Opex in the second five-year period (with 8.3% and 20.8% of BVTs being SupC- and L-band in year 10). Regarding nodal degree, we observe a significant increase of 55%, 39%, and 7% for strategies C+NFP, C+SupC+NFP, and C+SupC+L+NFP, respectively, by year 10. This leads to a 60.9% reduction in new degrees for C+SupC+L+NFP compared to C+NFP, despite 22% of nodes requiring L-band WSS for C+SupC+L+NFP. While introducing the new spectrum band reduces NFP deployment, it necessitates L-band ROADM deployment at nodes establishing a lightpath in the L-band. Conversely, in C+NFP, NFP nodes will need to be revisited for RoB deployment.

Initially, the C+SupC+L+NFP strategy achieves an impressive 60% reduction in length and a 45% reduction in links compared to C+NFP. However, it's important to note that the average link lengths in D3 and D2 show minimal variation (see Figure 11). Thus, in a MAN network, L-band equipment may not significantly reduce OPEX as it typically does in backbone networks. As shown in Figure 16(a), a 71% OPEX saving occurs by year 10. However, Figure 16(b) shows a less favorable CapEx outcome. Although a license-based approach and PAYG could control CapEx from year 1 to year 6, traffic growth from 16 Tbps in year 1 to about 330 Tbps by year 10 necessitates NFP deployment or expansion beyond C-band channels after year 1.
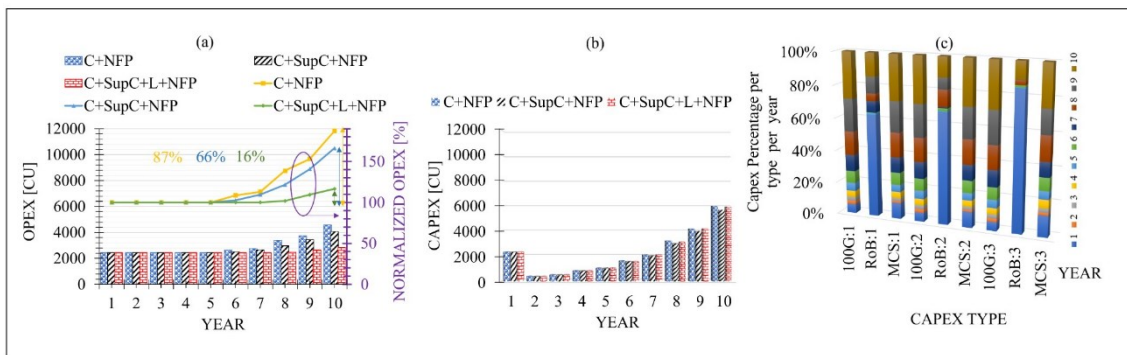
Figure 16: (a) Opex, (b) Capex, and (c) Contributions from different Capex types over a 10-year period for the following scenarios: (1) C+NFP, (2) C+SupC+NFP, and (3) C+SupC+L+NFP. The notations 100G:x, RoB:x, and MCS:x represent the Capex contributions of 100G, RoB, and MCS for scenario x.

Unfortunately, establishing new channels beyond C-band requires new SupC(+L)-band equipment, especially RoBs, across all nodes along the lightpath, leading to exponential CapEx growth in C+SupC+L+NFP, similar to C+NFP and C+SupC+NFP, with identical values. Detailed insights into Capex components are shown in Figure 16(c). The percentage of RoBs in C+SupC+L+NFP, at around 20%, surpasses that in C+NFP from year 1 to year 5. Across the decade, similar patterns are observed for other Capex items. As expected, deploying beyond C-band components does not significantly reduce Capex in the terminal section (C100G and CMCS). Figure 17 and *Figure 18* highlight that the most substantial portion of Capex is attributed to transponders, which remain unaffected by beyond C-band technology and peak in year 10. Finally, optical TCO variations are shown in Fig. 19(a)-(c), reflecting differences in IRU/lease prices across countries, cities, and contract types. Fig. 19(a)-(c) reveals that the C+SupC+L+NFP approach reduces OTCO [CU] by 17% to 27% by year 10. For example, with a CU value between 10-15 thousand US dollars, this reduction saves approximately 5-8 million US dollars by year 10 with CIRU = 1.5.
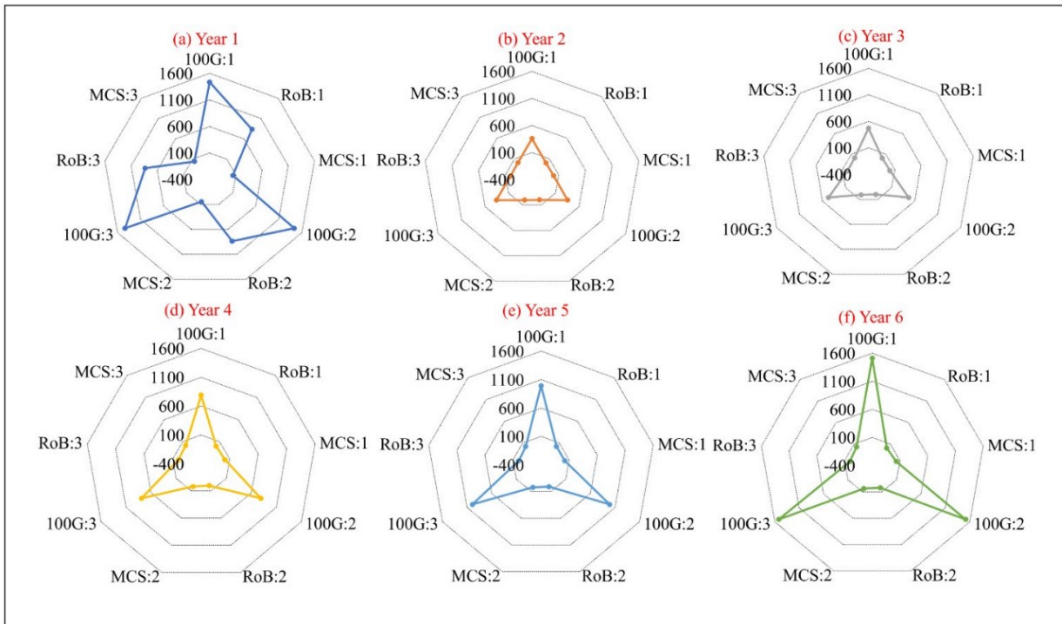
Figure 17: Capex over first 6 years for RoB (ROADM-on-a-blade), MCS (multi-cast switch), and 100G for the following scenarios: (1) C+NFP, (2) C+SupC+NFP, and (3) C+SupC+L+NFP. The notations 100G:x, RoB:x, and MCS:x represent the Capex contributions of 100G, RoB, and MCS for scenario x.

"NOTE: CapEx scale starts at -400 for ease of representation, all element costs are greater than zero"
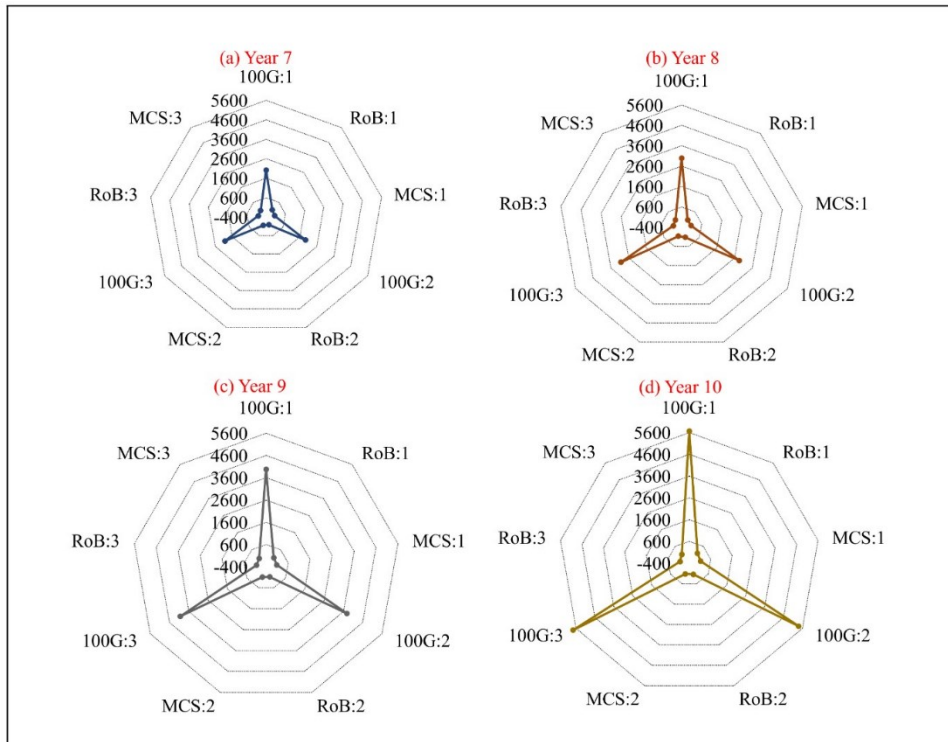
Figure 18: Capex over last four years for RoB (ROADM-on-a-blade), MCS (multi-cast switch), and 100G for the following scenarios: (1) C+NFP, (2) C+SupC+NFP, and (3) C+SupC+L+NFP. The notations 100G:x, RoB:x, and MCS:x represent the Capex contributions of 100G, RoB, and MCS for scenario x.

"NOTE: CapEx scale starts at -400 for ease of representation, all element costs are greater than zero"

Finally, as shown in Figure 19, the normalized TCO for C+SupC+L+NFP can be reduced by up to 90.9% in year 10 compared to year 1. In the initial years of network establishment, more CapEx and OpEx are required to develop the infrastructure. However, as traffic increases, multi-band technology helps offset these costs. While it imposes a 20% overhead compared to C-band, the reduction in new fibre pair deployments significantly decreases the normalized TCO, demonstrating the efficiency of multi-band technology. It should be noted that this figure reflects simulation results with CIRU = 1.5. Therefore, in networks where fibre pair deployment is less expensive, the benefits of leveraging multi-band technology will be reduced.
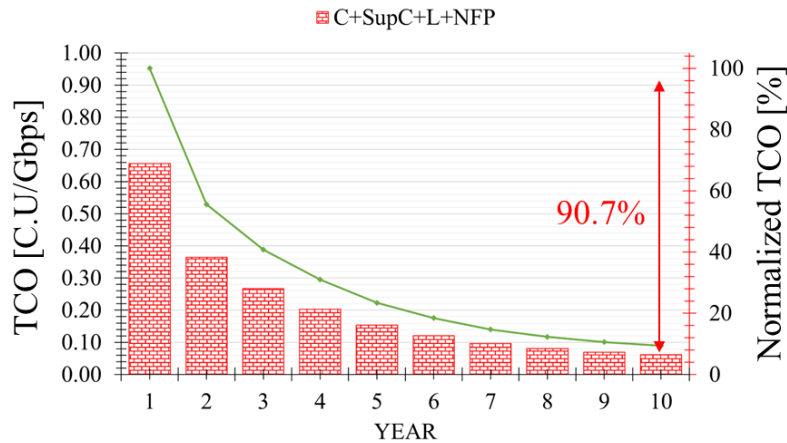
Figure 19: Normalized Total Cost of Ownership (TCO) for the C+SupC+L+NFP strategy. CIRU = 1.5.

3.1.8   Summary

This study introduces three band/fibre migration strategies: C+NFP, C+SupC+NFP, and C+SupC+L+NFP, facilitating a seamless upgrade of hierarchical optical metropolitan area networks (MAN) from the C-band to C+SuperC(+L-band). A multi-task 6D MAN planner has been developed for service provisioning, incorporating six key functions: multi-homed link and node disjoint routing, QoT estimation, spectrum assignment and traffic grooming, fibre pair selection, cost model analysis, and multi-period traffic growth. The study demonstrates that implementing C+L-band solutions on specific links can significantly extend the longevity of existing networks, reducing the need for new fibre deployments. However, adopting this new technology incurs a cost premium of approximately 20% compared to existing solutions.

The results show that deploying L-band equipment on selected links effectively enhances the lifespan of current networks, ensuring congestion-free operation with minimal intervention. Overall, the findings emphasize the importance of exploring alternative spectral resources beyond the traditional C-band, highlighting the potential of strategically deploying L-band equipment to address capacity constraints in MANs. This leads to a remarkable 60% reduction in length and an impressive 45% decrease in the number of links. This conservation of fibre pairs results in substantial OPEX savings, approximately 71%, and improved cost efficiency in optical total cost of ownership (TCO), ranging from 17% to 27% over ten years. Finally, while the SupC-band and Super C+L band contribute to extending the network's lifespan, it's crucial to note that the maximum cost savings achievable with the SupC-band are approximately 9% based on optical TCO, a figure that is roughly three times higher when employing the Super C+L band.

3.2 POWER CONSUMPTION OF POINT-TO-MULTIPOINT COHERENT METRO AGGREGATION NETWORKS

3.2.1 Study Objective and Motivation

The environmental impact of telecommunications is becoming increasingly relevant in our society as more data is transmitted every day. While telecommunication networks can help reduce power consumption in other areas (such as e.g. travel), the power consumption associated to communication equipment itself is reaching unprecedented levels as a consequence of the growing bandwidth demand needed by novel applications and services. This overall power demand currently accounts for 3-5% of the global consumption. The optical network infrastructure contributes in part to this figure, hence the need to optimize the cost and power efficiency of these networks as much as possible. In this analysis [Mas23], we focus on estimating the energy efficiency of several types of optical transceivers when employed in the most common topologies of metro aggregation networks, i.e., horseshoes, rings, and hub-and-spoke topologies. We considered three different types of coherent pluggable modules: (i) 400G ZR point-to-point (P2P); (ii) 400G ZR+ P2P; and (iii) 100G/400G point-to-multipoint (P2MP) which can be enabled by digital subcarrier multiplexing (DSCM). Specifically, we aim to demonstrate how the P2MP solutions, enabled and tested throughout multiple B5G-OPEN backed solutions, can simplify network design and lower power consumption due to higher flexibility.

3.2.2 Network Scenarios

In metro aggregation networks, there has been a misalignment between actual traffic patterns and the underlying transmission technology. For example, metro aggregation traffic is overwhelmingly Hub-and-Spoke (H&S), with multiple low data rate transceivers communicating to a few hubs operating at high data rate. On the other hand, optical connectivity has been mainly realized using Point-to-Point (P2P) technology in networks other than PONs. This is a suboptimal network architecture that requires a large number of bookended transceivers as part of the aggregation stage, in addition to numerous intermediate aggregation devices that adapt flows to higher order containers [Wel21].

Alternatively, it would be possible to broadcast/narrowcast the traffic, using simple passive splitter/combiner devices to transmit/receive from a hub, while P2MP interfaces can steer different sized flows to different destinations according to traffic hub/leaf needs. In this analysis, we look at three baseline architectures for metro aggregation: 400G ZR P2P with Regen [400ZR]; 400G ZR+ with Express [OZR+]; and 100G/400G P2MP [Wel22]. These are illustrated in Figure 20 for horseshoe topology deployments.

3.2.3 Modeling and Analysis

For the techno-economic analysis, we have considered different types of networks: (i) horseshoe, (ii) ring, and (iii) an H&S; where traffic is considered symmetric. For the horseshoe network, each leaf node transmits the same amount of data to both hubs (see Figure 20). Similarly, for the ring network, each node transmits the same amount of data to the given end hub through both ends of the ring structure. Regarding the H&S network, a single hub is used to terminate traffic from all leaf sites. The amount of traffic can differ for leaves connected to the same hub. For each network configuration, we simulate 5, 9 and 12-node metro networks, where we consider dual hubs (for horseshoe and ring only) and duplicated hardware at leaf sites for redundancy purposes. The initial conditions for the traffic from the leaf node(s) to the hub(s)

are set to 100G, and we assume a traffic growth of 100G per year per leaf node, which corresponds to a total of 38% CAGR over a 5-year period in line with analyst reports. The traffic analysis performed in this study obeys the following profile: odd leaf sites (i.e. 1, 3, …, 11) transmit $1 \times 100G$ to the hub(s), while even leaf nodes (i.e. 2, 4, …, 12) transmit $2 \times 100G$ to the hub(s). For each type of network, we compared the three different coherent-based approaches shown in Figure 20.

In horseshoe or ring configurations, the traffic between the source and the destination is regenerated at the intermediate leaf sites using 400G ZR pluggables. In the 400G ZR+ P2P w/Express solution, traffic is optically express forwarded at the intermediate leaf sites, taking advantage of the higher optical performance of 400G ZR+. From a line system perspective, this can be implemented in several ways, including the use of fixed or reconfigurable optical add/drop multiplexers or a filterless line system with passive couplers and combiners. Both 400G ZR w/Regen and 400G ZR+ w/Express operate in a P2P configuration along the horseshoe ring. However, a single 400G ZR P2P pluggable can "regen" multiple 100G streams, and it is assumed that a dual-router setup (4 Terabit (4T) for 400G and a 1T router for lower speeds, interconnected with grey optics) provides a lower granularity of service. To better match the H&S traffic, a 400G P2MP transceiver is deployed at each hub site, while 100G P2MP pluggables are introduced at the remote leaf nodes. Given the 25 Gb/s granularity, a single 1T router is assumed at each leaf node. The study looks at two aspects: (i) number of telecom devices used in each setup to assess the cost and impact on electronic waste; (ii) CO_2 emissions.
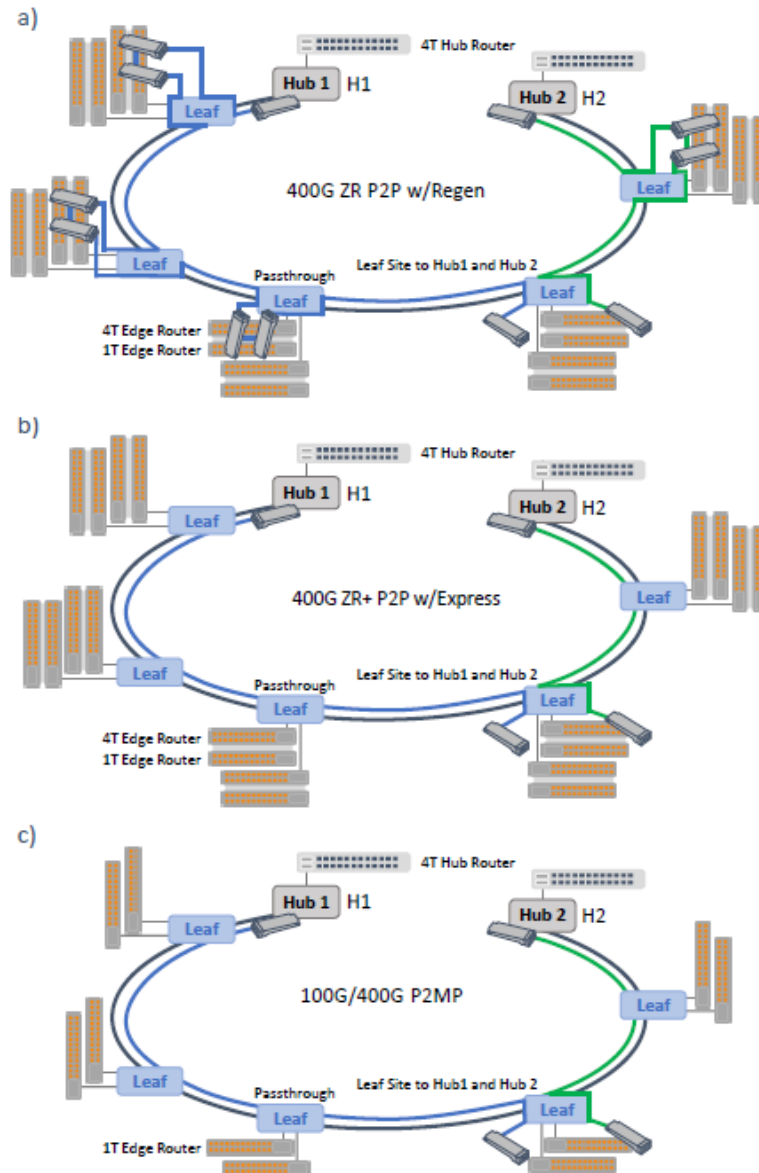
Figure 20: Horseshoe configurations for: a) 400G ZR P2P with Regen; b) 400G ZR+ P2P with Express; c) 100G/400G P2MP

3.2.4 Results

The main assumptions used in this analysis are listed hereafter: (i) 400G ZR+ P2P w/Express has the same power consumption as 400G P2MP; (ii) 400G ZR P2P w/Regen has the same power consumption as 100G P2MP; (iii) The power consumption of a 4T router ($10 \times 400G$ ports) at hub sites is the same as that of a 4T mix router at the leaf sites; and finally (iv) the power consumption of a 1T router is 10% of a 4T router.

Our analysis reveals that the number of devices, when using 400G ZR P2P w/Regen, increases significantly with traffic growth (Figure 21 and Figure 22). In horseshoe and ring configurations, this can be explained by the fact that all traffic streams must be regenerated at each intermediate site; hence, there is a considerable increase in the number of coherent pluggables as traffic grows. Furthermore, increasing the number of leaf sites also impacts the number of devices, since each additional leaf site will be required to "regen" the traffic, thus driving the

need for more routers and 400G ZR P2P pluggables. We also notice that the gap between 100G/400G P2MP and 400G ZR+ P2P w/Express is smaller than the gap between 100G/400G P2MP and 400G ZR P2P w/Regen given the latter requires fewer coherent pluggable compared to 400G ZR P2P w/Regen (no regeneration is required at the intermediate leaf site). However, 400G ZR+ P2P w/Express uses higher count of routers given its granularity of 400G compared to 100G/400G P2MP's granularity of 25G. For the H&S configuration (Figure 23), the number of devices for 400G ZR+ P2P w/Express and 400G ZR P2P w/Regen is the same since both require the same number of routers, grey and coherent pluggables. In this configuration, we notice that 100G/400G P2MP requires on average 50% fewer devices than 400G ZR+ P2P w/Express and 400G ZR P2P w/Regen.

Figure 21: Number of devices per coherent pluggable solution for horseshoe topologies with 5, 9 and 12 leaf nodes per network.

Figure 22: Number of devices per coherent pluggable solution for ring topologies with 5, 9 and 12 leaf nodes per network.

Figure 23: Number of devices per coherent pluggable solution for H&S topologies with 5, 9 and 12 leaf nodes per network.

Regarding power consumption, we look at the combined consumption of routers and coherent pluggables in the considered scenarios. Our calculations suggest a beneficial impact of

37

100G/400G P2MP transceivers in horseshoe configurations, as they reduce power consumption by ~75% compared to 400G ZR+ P2P w/Express and 400G ZR P2P w/Regen, since fewer routers and pluggables are needed at the hub sites [Bac20]. Furthermore, the finer granularity of 400G P2MP allows us to deploy smaller and more power efficient routers at leaf sites compared to the alternative approach, which required two interconnected/stacked routers (4T and 1T) for higher-speed and lower-speed communication, respectively. Additionally, a single coherent 400G P2MP pluggable can be connected to a maximum of 16 leaf nodes simultaneously at a data rate of 25G per leaf, thus reducing the number of interfaces at the hub sites. We also notice that, as the traffic and the number of leaf sites increase, the power consumption gap between 100G/400G P2MP and 400G ZR P2P w/Regen widens significantly; especially in Y5 when a horseshoe network with 12 leaf sites is modeled. This can be explained by the excessive number of 400G ZR P2P pluggables that have to be deployed at intermediate sites to regenerate the terminating and digitally passthrough traffic. In a ring configuration, the results are similar to the horseshoe configuration. Here, the 100G/400G configuration with P2MP reduces power consumption up to 89% when 12 leaf nodes are analyzed. For H&S configuration, on the other hand, traffic is not regenerated as there are no intermediate nodes. For this reason, the number of coherent pluggables for 400G ZR+ P2P w/Express and 400G ZR P2P w/Regen solutions is the same. Moreover, the number of routers for both configurations is also the same. 400G ZR+ P2P w/Express, however, has a slightly higher consumption than 400G ZR P2P w/Regen due to the fact that 400G ZR pluggables consume less power than 400G ZR+ pluggables (15 W versus 25 W, respectively). To assess the carbon footprint of a network in relation to consumed power, we have used data from the US Energy Information Administration (EIA) [17] to estimate CO_2 emissions according to energy source: 1.012 kg/kWh corresponds to coal, 0.413 kg/kWh is the value for natural gas, and 0.966 kg/kWh denotes petroleum. For this study, we have also assumed different weights (i.e. contribution percentage) for the electricity generated from coal (30%), natural gas (30%), and petroleum (40%) according to [Bac20]. The results showing the estimated CO_2 emissions as a function of the number of nodes and growth for the various scenarios are depicted in Figure 24, Figure 25 and Figure 26 for horseshoe, ring and H&S architectures respectively. These results show that100G/400G P2MP pluggables undoubtedly exhibit the lowest amount of CO_2 emissions among the approaches we have considered and investigated.
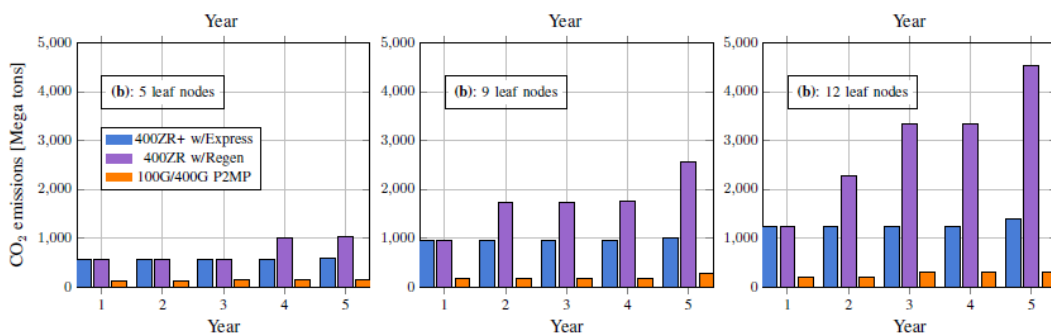
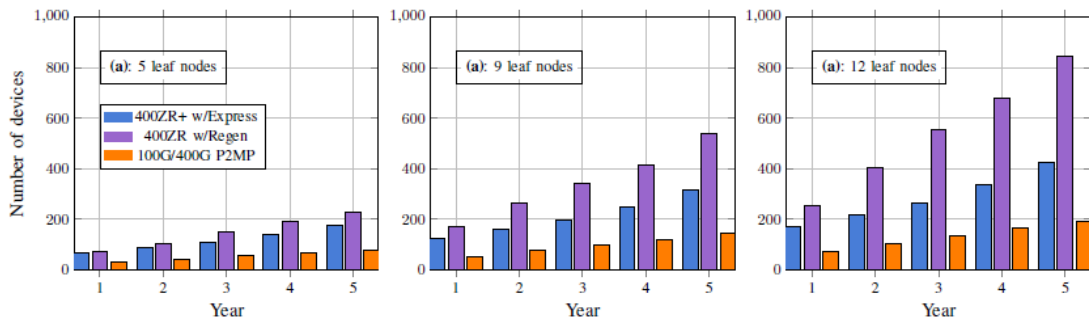

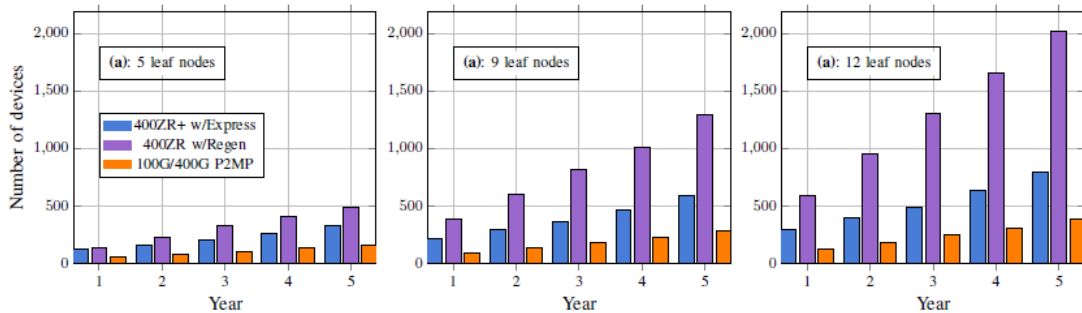Figure 24: CO_2 emissions per coherent pluggable solution for horseshoe topologies with 5, 9 and 12 leaf nodes per network.

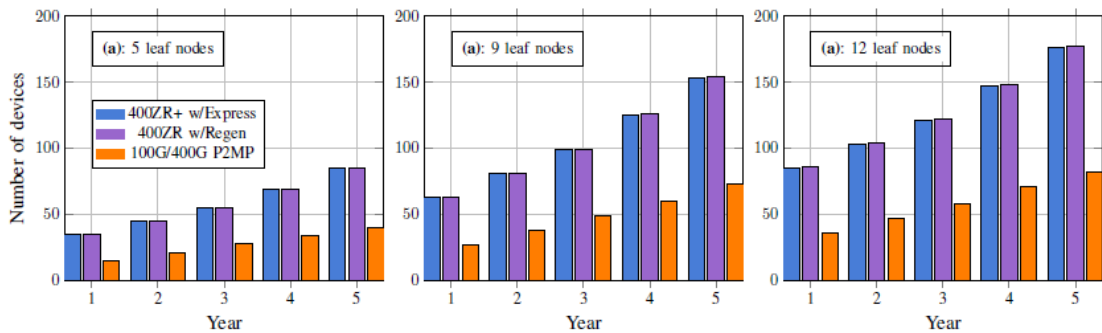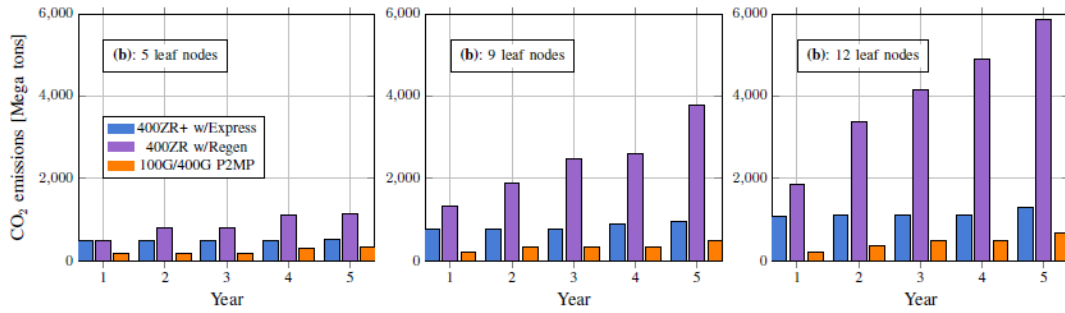*Figure 25: CO2 emissions per coherent pluggable solution for ring topologies with 5, 9 and 12 leaf nodes per network.*
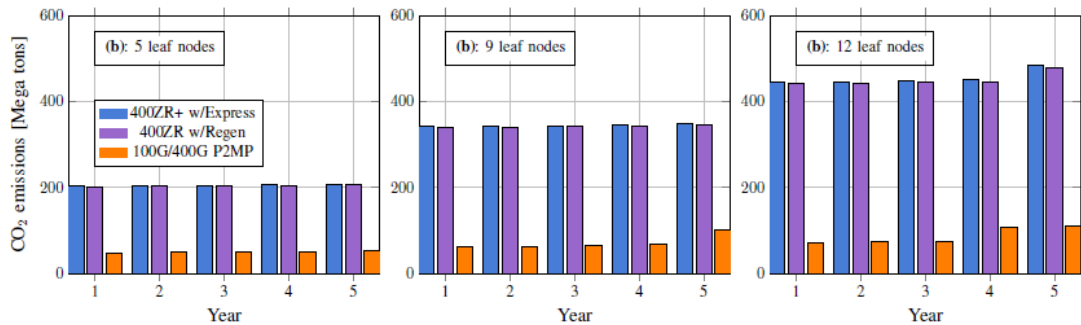
Figure 26: CO2 emissions per coherent pluggable solution for H&S topologies with 5, 9 and 12 leaf nodes per network.

3.3 NETWORK CAPACITY ANALYSIS

This section is dedicated to an analysis of the capacity needed in the metro and backbone networks assessed on a time horizon starting from the beginning of the project (2021) and projected to values accomplishing a target specified in KPI 2.3 (10 x in comparison to in-service bandwidth available at the project start period). Before proceeding, let's first provide a reminder of the terminology. The term in-bandwidth service refers to the capacity in terms of data rate available for services, while the bandwidth refers to the spectrum used by the optical signals used to carry those services. The ratio between capacity (bit/s) and spectrum (Hz) used is defined as spectral efficiency (SE), a parameter subject to the Shannon limit.

The analysis on network capacity is carried out from two points of view:

1) from an operator viewpoint (with an analysis based on data from TIM, but which has many common points with other European operators)) based on the expected evolution of traffic demand and networks, and;

2) from a more general point of view, which goes beyond the operator specificity and takes into account the technological trends in optical technologies and equipment, including the switching and transmission technologies exploiting multi band developed and experimented in the B5G-OPEN project.

3.3.1 Operator perspective

In this subsection dedicated to the operators' perspective of network capacity growth analysis an overview of timeline for in-service bandwidth increase is presented assuming two steady CAGR values (i. e., lower, +26%, and higher, +41%) as a reference for the analysis. These two

CAGR values identify a range within which, by sure or with a very high probability, the demand for network capacity in metro and backbone optical networks has evolved and will evolve.

Figure 27 identifies the time periods (i.e. the years) in which the 10-fold in-service bandwidth multiplication factor required by KPI 3.2 will be achieved. With a CAGR of 41% (higher value, orange bars Figure 27) the 10-fold multiplication compared to the project start year will be achieved in the second half of 2027 (very close from today), while with a CAGR of 26% (low, blue bars in Figure 27, the 10-fold multiplication of the in-service band will be achieved later, at the beginning of 2031.

Different operators have different in-service band growth rates, but the majority have values within the limits mentioned above [Tef24], [Lig22], [Eri24]. TIM, for example, in the last decade has recorded traffic growth values around 30-35% per year in its metro and backbone networks due to important increase of traffic in the access [Tim23].
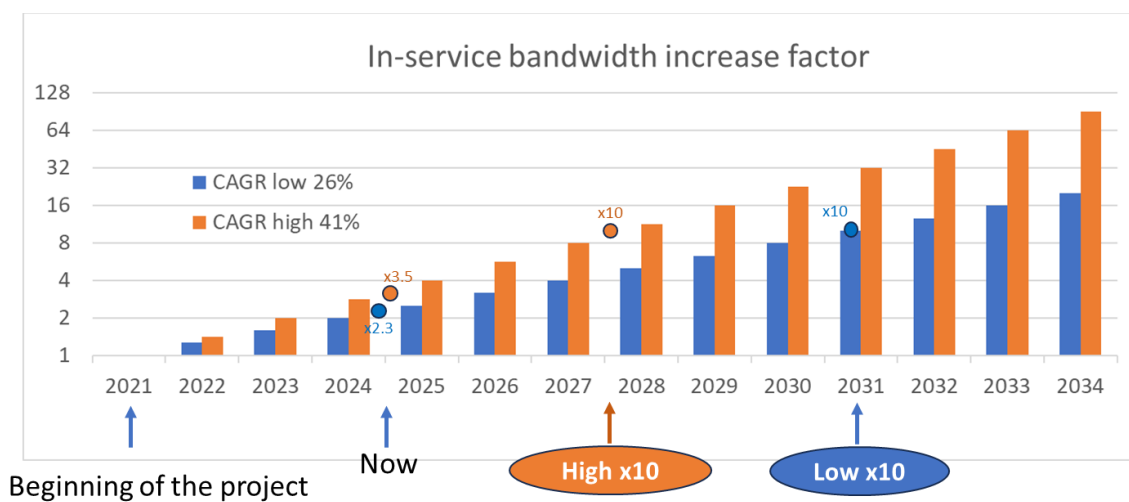
Figure 27: In-service bandwidth increase factor assuming two different CAGR and starting from beginning of the project (year 2021).

In Figure 27, values represented by bars refers to the beginning of the year. Increase factor 1 is for beginning 2021, period of project proposal editing and KPIs definition and reference for the diagram. Mid-2027 is the period in which in-service bandwidth increases tenfold from 2021 with a CAGR of 41%; beginning 2031 is the same for a CAGR of 26%.

An analysis will now be made on the temporal evolution of the data plane devices between the beginning of the project (2021), today (mid-2024) and the period in which the multiplication by 10 of the in-service bandwidth will be achieved as required by KPI 3.2. As we already pointed out and shown in Figure 27 the x10 period is between 2027 and 2031, depending on the CAGR of traffic increase.

The analysis is articulated separately in the three network segments, metro aggregation, metro core and backbone, shortly recalled hereafter in their main characteristic of topology and traffic pattern.

Metro aggregation is made of horseshoes having up to ten nodes in the chain including in-between leaves (up to eight) and two end-tail hub nodes. Hub nodes also take part of one of the metro-regional metro core meshed networks. The total horseshoe length is usually less than 100

Km, but distance up to 200 km can be possible. Traffic is prevalently or exclusively hubbed from leaves towards hub nodes.

Metro-regional core topologies are meshes made of one to some dozens of nodes covering a macro region made of one to three administrative regions (14 macro region in total in TIM Italian network), with up to 400 Km network diameter. Traffic is mainly hubbed toward one or few National nodes taking part both of the metro-core mesh and backbone network; a subset of Metro-regional core nodes host also the nodes of National backbone level.

National Backbone shows a meshed topology (nodal degree is up to 6), with a spread traffic pattern, but with a convergence of flows to few super-core nodes (and also between such super core nodes). TIM optical Backbone has about 50 nodes in total, of which about 35 with add/drop capability and the remaining pass-trough/transit only nodes, and a subset of about 10 super-core nodes with very high traffic. Backbone topology counts about 80 link in total. Network diameter is of the order of 2000 even if almost all the traffic is on paths under 1000 km and a significant part (>50%) on paths under 500 km.

3.3.1.1   State of the network and capacity needs at the beginning of the project

If we look at the technologies that an operator like TIM has deployed in the aggregation, metro core and backbone segments at the beginning of the project (year 2021), the following scenario could be observed.

In the metro aggregation segment, the regional hubbed traffic over horseshoes was carried by N x 10G IMDD transceivers. (for almost everyone it was N=1, often at moderate % of link occupation). Optical nodes were F/ROADM (2 nodal degrees in leaves, with few exceptions), line systems were made with DCF compensated fibre and used C bandwidth fixed grid 40 channels at 100GHz (SE = 0.1 Bit/s/Hz). Wavelength occupation in line systems was less than 50% on most of the line systems.

In the Metro-Regional segment, the traffic is mainly hubbed towards National nodes over the topology mesh. Services are carried by N x 100G coherent wavelengths (N=1 mostly). The optical network is a mesh of ROADMs (2 to 5 nodal degrees) over uncompensated fibre. C-band systems were of 80 fixgrid channels at 50 GHz (SE = 2 Bit/s/Hz). System occupation was about 50% in most congested links.

In Backbone-National network line rate was 100 Gb/s in 50 GHz or 200 Gb/s in 75 GHz coherent (SE = 2 to 2.6lBit/s/Hz). The network was a mesh of flexgrid CDC ROADMs (2 to 6 nodal degrees) linked by line systems over uncompensated fibre. 4.8 THz in C-Band is exploited with a resolution of 12.5GHz and a minimum channel bandwidth of 37.5 GHz. Occupation was greater than 50%, in few cases near the saturation, in most loaded link.

3.3.1.2   Update to current situation from beginning of the project

Looking at the current state of traffic and technology in the network, we can observe that, in comparison to the beginning of the project (2021), the traffic has increased by a factor of approximately x3, as shown in Figure 27.

In the aggregation network, the equipment (optical nodes and transceivers) has not changed in in relation to the state present at the start of the project. In most of the situations, Nx10G IMDD (many N=1, some N=2, a few N>3) are now required between leaves and hubs. System occupation is around or higher than 50%, and this requires an upgrade of technology to scale. One solution is to still rely on C-Band only systems (even possibly extended) but using 80 to 100

channels at 50 GHz instead of 40 channels at 100 GHz. Such upgrade requires a replacement of current ROADM nodes. This change can be made in combination with the use of 100 Gb/s (or even higher data rates) coherent transceivers. Another option is the introduction of XR DSCM systems (e.g., 400Gbt/s hubs and up to 200 GB/s leaves) with filtered (modified ROADMs enabling point to multipoint networking) or filterless nodes.

In the metro-regional core network N x 100G coherent in 50 GHz (N=1, 2 , 3) flows between nodes are currently required. The nodes can be maintained as they are (fixed grid 80 channel ROADMs) but as the system occupation reaches or exceeds the 50%, there is a need an upgrade of technology to scale with 200G/400G coherent transceivers as a first step, and then introducing SDM (multi fibre parallel line systems) or/and Multi Band (C+L) systems as a further development.

In the backbone the same optical switching and line infrastructure is maintained but line rate has reached 400 Gb/s in 75 GHz for part of the reaches required (SE = 5.3 bit/s/Hz, up to around 400 km). For longer reaches 200 Gb/s (SE =2.6 bit/s/Hz) remains the reference line rate. As occupation is higher than 50% on some links despite the increase in line rate (in few cases already reaches the saturation), a technology upgrade is needed to scale. 800 Gb/s line rate, SDM (multi-fibre or multi-core) and/or multi bandwidth is required (in fact, multi fibre has already implemented in the super-core of photonic backbone).

3.3.1.3 Capacities and optical system upgrades to cope with x 10 in-bandwidth service from beginning of the

In the future, when the in-bandwidth service traffic will be tenfold the one at the project beginning, capacities and network solutions are expected to be the following ones.

In metro aggregation, x 10 traffic increases will require the use of N x 100G coherent transceivers (N usually 1 or 2, in a few cases N > 2) or the use of DSCM P2MP systems with hubs at rates higher than 400 Gb/s (e.g., 800 Gb/s at hubs and up to 400Gb/s at leaves with a sub carrier granularity of 50 Gb/s). Extended-C band flexgrid ROADMs will therefore be necessary in the case of P2P while transformed ROADMs (i.e., enabled for P2MP) or filterless nodes will be the optical node solution for the P2MP case.

In the metro-regional core segment, the traffic increase leads to the need of Nx400G or Mx800G coherent (N=1 to 4, M=1 to 2) flows. A mesh of extended C-band or C+L optical nodes (SB or MB ROADM) will be required. Multi-fibre is a possible choice to cope with extraordinary needs on specific topology edges.

In the backbone segment, traffic needs will require an upgrade of technology to scale (higher client and line rates, SDM, MB). The traffic requirement can be satisfied thanks to coherent transceivers with line rate of 400 Gb/s or higher (SE = 5.3 Bit/s/Hz, e.g., 800G in 150 GHz) and with MBoSDM nodes. Bandwidths used could be C+L or S+C+L. In each band 6 THz flexgrid systems should be employed (with differences from band to band). The SDM can be realized on the most critical edges more likely with multi-fibre, possibly with multicore fibre.

3.3.1.4 Summary and comment of achievement of KPI 3.2

Table 4 summarizes the evolution of the optical system solutions required from the beginning of the project until the achievement of the growth of in-bandwidth service specified by KPI 2.3. Note that this is a specific scenario from one of the consortium's operators, but nevertheless constitutes a fairly representative scenario of the European ecosystem. Table entries are from

B5G-OPEN Consortium

an operator perspective with a target of in-bandwidth service capacity tenfold compared to the values at the start of the project (2021). The period in which this tenfold multiplication occurs depends on the annual rate of traffic growth: assuming that the CAGR is between 26% and 41%, this period is in the range between mid-2027 and beginning 2031.

Table 4 - Transmission (T) and switching (X) optical system solutions for the three network segments analyzed and in the three timeframes considered.

Network Segment	T/X	Begin of project 2021	Now Mid 2024	Mid 2027 to 2031 (CAGR dependent) (x 10 in-bandwidth service increase)
Metro Aggregation	T	10G IMDD	Nx10G IMDD	P2P: 100G coherent Tr. on leaves OR P2MP: with 400G DSCM Tr. on hubs
	X	FOADM, DCF C-band	FOADM, DCF C-band	extended C-band R/F-OADM for P2P OR Mod. ROADM or filterless for P2MP
Metro Core	T	100G coherent	Nx100G coherent	Nx400G or Mx800G coherent for P2P (P2MP 800G DSCM Tr. on hubs possible)
	X	CD ROADM, C-band	CD ROADM, C-band	CD ROADM, ext. C-band or C+L bands and/or multi-fibre for P2P (Modified ROADM for P2MP)
Backbone	T	Up to 200G cohe.	Up to 400G cohe.	> 400G coherent (e.g., 800G/1.6T, 150/300 GHz, SE 5.3 bit/s/Hz at 1000 km)
	X	CDC ROADM C-band	CDC ROADM C-band	MBoSDM node (S)+C+L bands and multi fibre/core

If we look at the characteristics of the optical systems reported in the last column of Table 4 and consider the technologies under research in the project, and in particular those of the data plane as reported in D3.3 (the final deliverable of WP3), we can say that they will be able to guarantee the network updates that make it possible to reach the capacity objective expressed by KPI 2.3.

As regards the node capacity needed to support the future traffic growth, the analysis reported in D3.3 shows that the values of total and add/drop traffic reported in Table 1-1 of D3.3 are extraordinarily high because that values come from hypotheses of higher values of initial traffic and a high percentage of increase in future periods (short, medium and long term).

The situation of the last column (from the left) of the Table 4, which is based on a real scenario based on Operators' data, corresponds in broad terms, to the values of the short term of the Table 1-1 of D3.3.

That said, the systems analysed or developed in B5G-OPEN that allow to implement the requirements expressed in the fifth column of Table 4 (targeted to mid-2027-2031, depending on the grow rate) are the following.

A node architecture suitable for the Backbone or for the Metro-Core segment, in case of meshed network requiring very high capacity node architecture, can be a single or multi-band WSS based switching architecture as the presented in Section 2.7 of D3.3 and shown in Figure 28. This node

allows the internetworking with conventional point-to-point transponders operating in the C, L, S or other bands and the number of bands and fibres/cores used in a specific context depend on the capacity needed but it is definitely 10 times or even much more than the capabilities available at the beginning of the project as requested by KPI 2.3. Data rates suitable for metro core transceivers would be in the range of 200 Gbit/s-800 Gbit/s (and even higher in the long term), with a SE of up to 5 bit/s/Hz (or even slightly higher). Data rate for backbone transceiver and transponder could be even higher reaching and exceeding the Tb/s (for example 1.6 Tb/s) with a SE of the order of 3 to 4 bit/s/Hz.
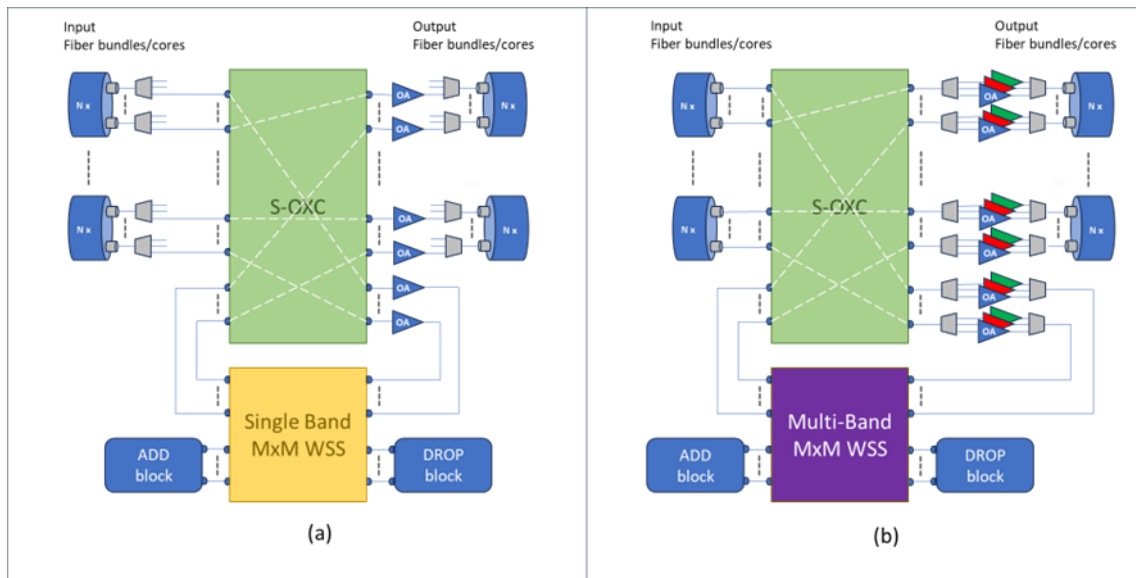
Figure 28: Combined MB over SDM (MSoSDM) node architectures suitable for the backbone or for the metro core in case of high capacity needs: (a) single-band matrix-switch-based MBoSDM node with a S-OXC, (b) multi-band matrix-switch-based MBoSDM node with a S-OXC. All the subsystems that make up the node are today commercially available or as systems in the R&D phase.

In addition to the solutions identified above, which use conventional point to point networking and ROADM or their extensions (i.e., MBoSDM nodes) in the metro core segment, in B5G-OPEN point-multi-point coherent optics (DSCM/XR) were also considered as a solution for the entire metro environment (aggregation and core). The challenge to investigate ROADM structures suitable for point to multipoint networking have been addressed in Section 2.8 of D3.3. Specifically, the problem that different digital DSCM subcarriers in the same wavelength coming from different sources cannot be merged by conventional and commercially available WSS based ROADMs is solved by means of 1) some novel modified ROADM architectures and 2) the configuration of light threes on the physical topology of the network (i.e., one light tree configured for each DSCM wavelength). In D3.3 four ROADM novel architectures for DSCM subcarriers internetworking have been proposed. The modified ROADM architecture shown in *Figure 29* is the simplest one, since it allows linear light threes only with hub at the end of the three; even if it is not yet commercially available, it would be easy to be implemented from spare commercial components. Regarding capacities, today's DSCM P2MP XR systems with 400 Gb/s hubs are available but in a long-term horizon it is possible to imagine that XR hubs could be at 1.6 Tb/s or even at 3.6 Tb/s (some concept, just need to scale the capacities), thus leading to a tenfold increase in the typical flow capacity on this network segment which was characterised by 100 Gb/s flows at the beginning of the project. The possibility of creating multi-band systems

(for example two coexisting light three systems in C- and L-bands) further increases the potentially available capacity in the metro core segment.
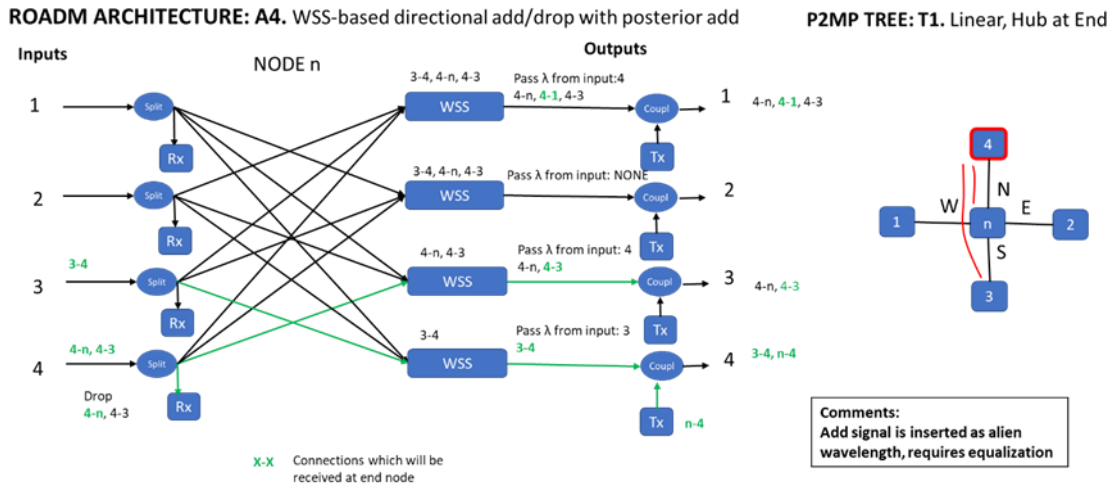
Figure 29: Modified ROADM with WSS-based directional add/drop with posterior add for applications in DSCM subcarriers switching in combination with light trees creation on physical topology.

In the metro-aggregation network segment, the low cost of the optical data-plane solution is an important driver, considering the high number of nodes comprised by this network segment. Very high value of node capacity for the access segment can be reached by novel architectures like the one developed and experimented in B5G-OPEN and presented in Section 2.9 of D3.3. An example of such a kind of node (other versions were developed) that can be used as leaf node in horseshoe topologies (i.e., two topological degrees plus add and drop) is given in Figure 29. Thanks to a simple SDM implementation (2 pairs of fibre on each degree) and to Multi Band wavelength blockers, the capacity handled by the node is very high, in the order of hundred Tb/s, that is, two degrees of magnitude higher than systems available at the beginning of the project and therefore also in this case KPI 2.3 is largely satisfied.
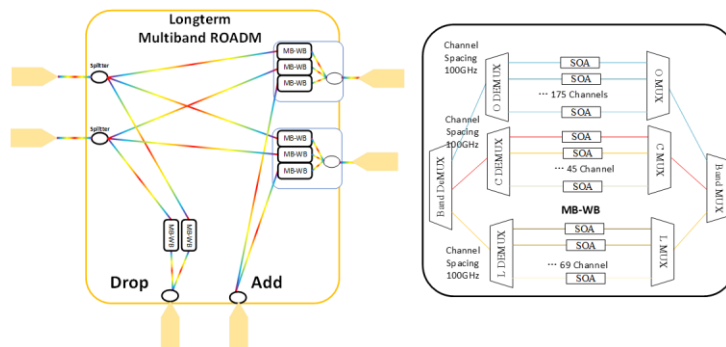
Long-term: 144 Tb/s
MB-Wavelength Blocker
Channel Spacing 100GHz
O(175 channel)+ C(45 channels)+L bands(69channels)

Figure 30 OADM architecture for an Access node based on O+C+L bandwidth and two parallel fibres. To obtain bidirectionality of the flows terminated on the node, two blocks like the one illustrated are necessary.

3.3.2   Technology perspective

From a more general point of view, this section discusses the technological trends in optical technologies to increase the in-service bandwidth of current transmission systems. One of the

most promising ways to resolve the looming capacity crunch relies on further increasing the existing systems transmission bandwidth using multi-band transmission. The ITU-T G.652D fibre offers a low-loss transmission spectrum of approximately 54 THz from the O- to the L-band, offering more than a ten-fold increase of the available bandwidth of conventional C-band-only systems (4.8 THz). Unfortunately, other transmission bands show worse optical performance than the C-band. Consequently, this bandwidth increase does not translate into a ten-fold increase in capacity.

Before deploying additional amplification bands, the trend of expanding the operating bandwidth of amplifiers from 4.8 to 6 THz in commercial systems is recognized as a strategy to augment system capacity without the costs of extra amplifiers, band multiplexers, and demultiplexers associated with multi-band transmission [Sho24]. To further increase the capacity of optical systems, MB transmission may be combined with techniques that leverage parallel spatial paths such as multi-fibre (MF), multi-core/mode fibre (MCF/MMF), or few-mode fibre (FMF) transmission.

The results presented in this section examine the optical performance and capacity of single- and multi-band systems, ranging from a minimum of one super-band (with a total transmission bandwidth of 6 THz) to a maximum of three super-bands (totaling 19 THz, including a 500 GHz guard band between adjacent bands) across the SuperC-, SuperL-, and SuperS-bands (SuperL-band from 184 THz to 190 THz, SuperC-band from 190.5 THz to 196.5 THz and SuperS-band from 197 THz to 203 THz). As a reference, we also consider a C-band-only system with 4.8 THz of available bandwidth (from 191.3THz to 196.1 THz).

3.3.2.1 Simulation setup

Employing a local span optimization approach, we set the launch power by assuming a line system with a single optical fibre span followed by an optical amplifier. Each band utilizes a dedicated amplifier, thus requiring a band demultiplexer and multiplexer at each amplification site. We assume the transmission of 80 channels on a 75-GHz grid on each super band and 64 channels on a 75-GHz grid on the C-band. Each channel consists of a 64 GBd signal with a 0.15 roll-off factor. The ITU-T G652.D optical fibre model characteristics are as follows. A nonlinear coefficient of 1.27 W^{-1}/km, a dispersion parameter of 16.8 ps/nm/km at 1550 nm, and a dispersion slope of 0.058 ps/nm^2/km, are assumed. The frequency-dependent loss coefficient and the Raman gain profile of the optical fibre are the same as in [Sou24]. Additionally, we assume input and output connector losses of 0.25 dB and splice losses of 0.01 dB/km. The optical amplifiers are modelled by a constant noise figure of [4.7, 4.3, 6.5] dB for the SuperL-, SuperC/C-, and SuperS-bands, respectively [Sou24]. The combined losses of the MUX/DEMUX are 1.5 dB for the two-band system and 3 dB for the three-band MBT systems.

3.3.2.2 Launch power optimization and point-to-point capacity-reach profile

We use the per-channel GSNR as the quality of transmission (QoT) estimation (considering the signal bandwidth as a reference). This QoT metric is given by:

$$GSNR_i = \frac{P_i}{P_i^{ASE} + P_i^{NLI}},$$

where P_i is the power of channel i and P_i^{ASE} and P_i^{NLI} are the power of the Gaussian noise corresponding to the amplified spontaneous emission (ASE) noise and the nonlinear interference due to the self- and cross-channel nonlinear crosstalk at channel i, respectively. The NLI noise contribution is calculated using the GGN model and the stimulated Raman

scattering (SRS) is calculated by numerically solving the Raman equations that govern this effect [Chr96]. Both methods are available in the open-source python library GNPy [OPT-PSE].

The goal of the launch power optimization is to maximize the total system GSNR while minimizing the GSNR variation within each band. Targeting a flat QoT profile potentially reduces the complexity of routing and wavelength assignment algorithms and increases the availability of channels [Men01]. The optimization variables are illustrated in Figure 31 for a S+C+L-band system. The variables are parameters that can be typically set on commercial amplifiers: the per-band average channel power (P_x) and tilt (T_x). The power of a channel i of band x is given by $P_{i,x} = P_x + T_x(f_i - f_x)$, where f_i and f_x are the frequency of channel i and the center frequency of band x, respectively. These optimization variables are chosen to simplify the optimization process, instead of optimizing the launch power of each channel, which would lead to N_{ch} optimization variables per transmission band, where N_{ch} is the number of channels per band. Moreover, the multivariate optimization problem was divided into a series of single-variable problems that were solved sequentially and iteratively until convergence, similarly to the approach followed in [Sou22].
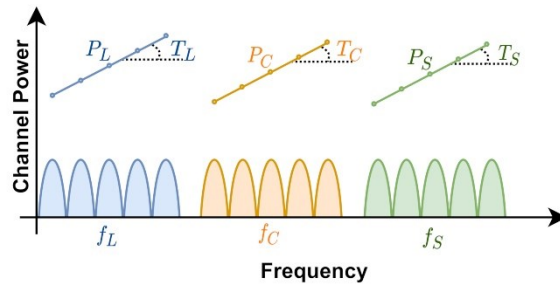
Figure 31: Representation of the optimization variables.

The optimized launch power and GSNR profiles for a single span of 75 km considering the use of C-, SuperC-, SuperC+SuperL- and SuperS+SuperC+SuperL-band are shown in Figure 32 and Figure 33, respectively. The systems with the best GSNR profiles are single band. This happens because of the extra MUX and DEMUX losses, higher nonlinearity, higher fibre attenuation and higher amplifier noise figure of the multi-band systems. The analysis of the figures also shows that adding the SuperS- to a SuperC+SuperL-band system improves the GSNR in the SuperL-band due to the power transfer between bands (caused by the SRS effect). Moreover, the average GSNR in the SuperS-band is much worse than in the other two bands.
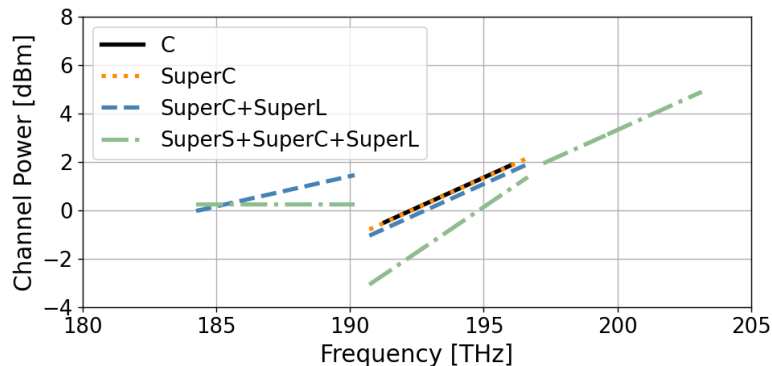
Figure 32: Optimized launch power for a 75-km span.
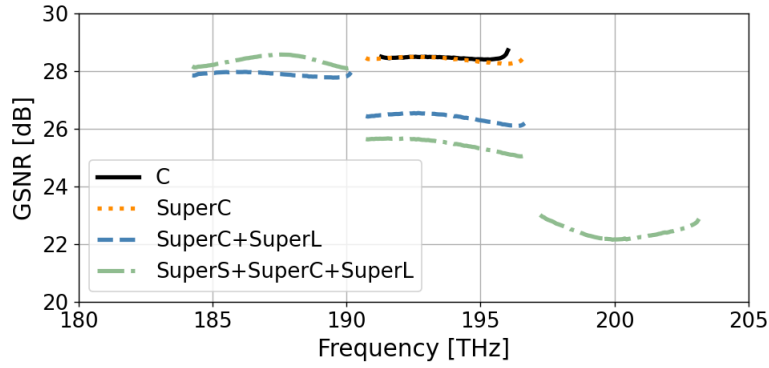
Figure 33: Optimized per-channel GSNR for a 75-km span.

The GSNR variation between amplification bands leads to several capacity-reach profiles for each of the transmission systems. To illustrate this phenomenon, consider an optical link composed of 75-km spans and a transceiver with the operation modes described in Table 5. The values of required OSNR were extracted from the Open ROADM Multi-Source Agreement (MSA) [OR]. The SNR_{req} values are calculated as i.e., $SNR_{req} = OSNR_{req} - 10\log_{10}(R_S/B_{ref})$, with R_S equal to the symbol rate and B_{ref} to 12.5 GHz [Ess12].

Table 5 - Required SNR and OSNR for each operating mode of the transceiver.

Mod. Format	QPSK	8QAM	16QAM
Bit rate [Gb/s]	200	300	400
OSNR$_{req}$ [dB]	17	21	24
SNR$_{req}$ [dB]	9.2	13.2	16.2

For each band, the GSNR at the end of a lightpath with N spans of length L_n is given by:

$$\text{GSNR}_N = \sum_{n=1}^{N} \text{GSNR}_{OPT}^{L_n} - M,$$

where $GSNR_{OPT}^{L_n}$ is the optimized GSNR of the worst channel in each band and M is the system margin defined as $M = 2 + 0.05 N_{OLAs}$. The system margin comprises a fixed 2 dB margin and a variable contribution that depends on the number of traversed optical amplifiers (N_{OLAs}). A lightpath is feasible for a given signal configuration and transmission band if the required SNR is smaller than GSNR_N.

Figure 34 and Figure 35 show the SE-reach and capacity-reach profiles of the different transmission systems, respectively (the reach is presented in terms of number of 75-km spans in the link). Clearly, the single-band systems have the best spectral efficiency for any reach and the longest reach because of the higher GSNR value on the single-span transmission ($\text{GSNR}_{OPT}^{L_n}$).
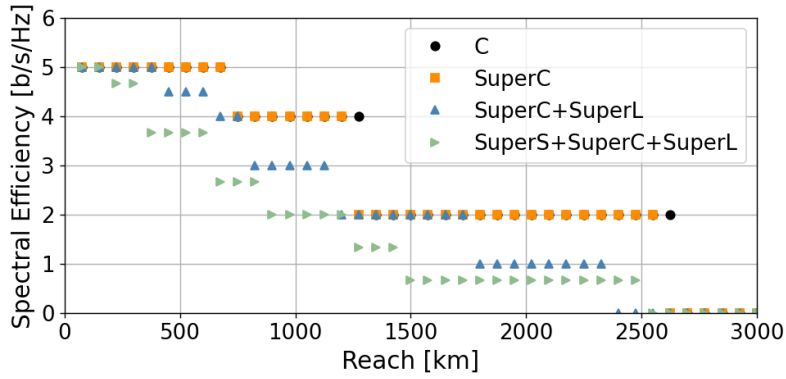
Figure 34: Spectral efficiency of the different transmission systems for different link lengths.
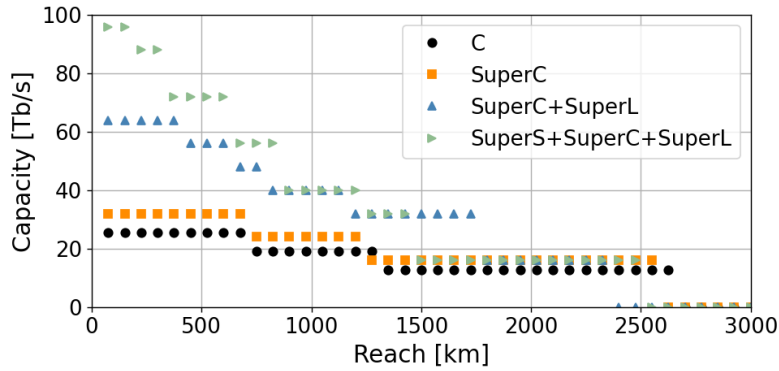
Figure 35: Capacity of the different transmission systems for different link lengths.

However, the multi-band systems have a higher total capacity for almost every transmission distance because of the higher channel count. The capacity increase due to the addition of another amplification band is greater for shorter reaches because of the worse optical performance of the multi-band systems. For example, adding the SuperL-band to a SuperC-band-only system doubles the link capacity (from 32 Tb/s to 64 Tb/s) for links shorter than 375 km (inclusive). However, the capacity is only increased by 72% for link lengths between 450 km and 600 km (inclusive). The capacity gain of doubling the available bandwidth of the SuperC-band-only system progressively decreases for longer reaches and there is no gain for links longer than 1800 km. Curiously, there is a loss in capacity (from 16 Tb/s to 0 Tb/s) for link lengths between 2400 km and 2550 km, i.e., the SuperC-band-only system is able to deliver 16 Tb/s for those link lengths while the link is unfeasible for the SuperC+SuperL-band system because of the lower $\text{GSNR}_{OPT}^{L_{\text{n}}}$ values.

Moreover, the capacity gain of adding the SuperS-band to the SuperC+SuperL-band is even smaller. There is a 50% increase in capacity for link lengths shorter than or equal to 150 km, and there is no gain for link lengths longer than or equal to 900 km. Comparing the three-band system with the SuperC-band-only system, there is a 3x capacity increase for link lengths shorter than or equal to 150 km, and there is no gain for link lengths longer than or equal to 1500 km, even though the three-band system requires three times the number of optical amplifiers and transceivers. Compared to the C-band-only system, the SuperS+SuperC+SuperL-band system offers a 3.75x capacity increase for link lengths shorter than or equal to 150 km, and there is no gain for link lengths longer than or equal to 2475 km. Further interpretations of the results shown in Figure 34 and Figure 35 are presented in the next section.

3.3.2.3 Summary and Comment of Achievement of KPI 2.3

Multi-band transmission is a promising way to cost-effectively increase the capacity of current optical transmission systems because of the wide low-loss window of the ITU-T G.652D fibre (approximately 54 THz). However, increasing the number of amplification bands reduces the spectral efficiency of the system (especially for longer links), as shown in Figure 34. Consequently, it is unlikely that all the available low-loss window of the fibre will be used for data transmission. A good compromise between spectral efficiency and bandwidth expansion seems to be using two or three super bands occupying 6 THz each (SuperC+SuperL or SuperS+SuperC+SuperL).

To achieve the in-service bandwidth growth of 10x (KPI 2.3) in comparison to the single-fibre C-band-only system in the near future, the proposed systems must be combined with space-division-multiplexing techniques such as multiple parallel fibres or fibres with multiple cores. By doing so, increasing the bandwidth of the amplifiers and MB transmission techniques reduce the number of parallel paths (parallel fibres or fibre cores) required to achieve the required in-service bandwidth growth and potentially the cost.

Table 6, Table 7 and Table 8 show the number of required parallel fibres/cores, amplifiers and transceivers to achieve 10x in-service bandwidth increase for each transmission system, respectively (these results are based on the SE and capacity profiles presented in Figure 34 and Figure 35). To achieve a 10x capacity growth with the C-band-only transmission system, it is necessary to use 10 parallel fibres. As mentioned before, increasing the bandwidth of C-band amplifiers from 4.8 THz to 6 THz (Super-C-band) enables the reduction of the number of deployed fibres (from 10 to 8), the number of amplifiers (by 20%) while maintaining the number of required transceivers. The multi-band solutions allow for a reduction in the number of deployed fibres at the cost of requiring more amplifiers and transceivers.

Table 6 - Number of required parallel fibres/cores to achieve 10x in-service bandwidth growth for each transmission system.

Link Length [km]	Transmission system			
	C	SuperC	SuperC+SuperL	SuperS+SuperC+SuperL
150	10	8	4	3
300	10	8	4	3
1050	10	8	5	5
2025	10	8	8	8

Table 7 - Number of required amplifiers to achieve 10x in-service bandwidth growth for each transmission system.

Link Length [km]	Transmission system			
	C	SuperC	SuperC+SuperL	SuperS+SuperC+SuperL
150	30	24	24	27
300	50	40	40	45
1050	150	120	150	225
2025	280	224	448	672

Table 8 - Number of required transceivers to achieve 10x in-service bandwidth growth for each transmission system.

Link Length [km]	Transmission system			
	C	SuperC	SuperC+SuperL	SuperS+SuperC+SuperL
150	640	640	640	640
300	640	640	640	686
1050	640	640	854	1280
2025	640	640	1280	1920

4 NEXT-GENERATION ACCESS WITH LIFI NETWORKS

4.1 POWER CONSUMPTION AND THROUGHPUT IMPACT OF LIFI INTEGRATION

4.1.1 Power Consumption and Achieved KPI 4.3

The transition to 5G has necessitated the deployment of high-density small cells, such as femtocells, to meet increasing capacity demands, especially in urban areas. Femtocells, typically used for indoor coverage, consume 10-30 W per cell for scenarios like residential or small business environments according to [Che22]. The energy-intensive nature of 5G small cells is primarily due to their need to support high data rates and dense user populations. The aggregate power consumption of 5G networks, including macro and micro base stations, can be substantial, with a single macrocell requiring 3 kW to 10 kW.

Table 9 - Specifications of different types of base stations as given in [Che22].

Type	Coverage Radius	Power Consumption	Application Scenario
Macrocell	1 – 10 km	3 kW – 10 kW	Main wide area radio coverage
Microcell	300 – 1000 m	150 W – 300 W	Infill radio coverage and additional capacity (e.g. urban and suburban)
Picocell	Limited	15 W – 50 W	Localised coverage (e.g. inside buildings)
Femtocell	Limited	10 W – 30 W	Coverage improvement (e.g. home or small business premises)

Compared to traditional 5G small cells, LiFi technology provides a significant reduction in power consumption. LiFi leverages existing lighting infrastructure as the transmission medium, allowing for a dual-purpose use of energy—supporting both illumination and data transmission—thereby improving overall efficiency.

By adopting LiFi technology, we achieved KPI 4.3, which targets a 50% reduction in energy consumption in small cell deployments. This achievement is supported by the following power measurements:

- The LiFi Access Point (AP) demonstrated a power consumption of only **3.64 W**.
- The user device USB dongle used **1.405 W**.

These power consumption values are substantially lower compared to traditional femtocells, which typically consume 10-30 W per cell. The inherent efficiency of LiFi, combined with the reuse of existing lighting infrastructure, contributes to significant energy savings, making LiFi a sustainable and energy-efficient alternative for indoor coverage scenarios.

4.1.2 Throughput Impact and Achieved KPI 4.4

In 5G networks, maintaining quality of service (QoS) during handover is a critical aspect of ensuring uninterrupted connectivity, particularly in dense small cell environments. 5G networks typically leverage overlapping coverage between adjacent cells to facilitate smoother handovers, but this also results in substantial throughput variations, depending on user mobility and network density. The challenge in 5G lies in sustaining a high throughput rate during these frequent handovers, especially in scenarios with high user mobility.

52

LiFi introduces unique challenges to handover management due to its limited coverage area and line-of-sight (LOS) dependency. Unlike traditional RF-based networks, the deployment of LiFi APs is determined primarily by lighting infrastructure, resulting in smaller overlapping areas between APs and necessitating more frequent handovers. Moreover, due to the directional nature of visible light, it is uncommon for a single user to be simultaneously covered by multiple APs, complicating the handover process.

Despite these challenges, our implementation has successfully achieved KPI 4.4, ensuring QoS-guaranteed handover with a minimum throughput exceeding 50% of system capacity during user mobility scenarios. Specifically, for a setup with throughput of **37 Mbps** (both downlink and uplink, where 43 Mbps is the device capability), we observed minimum throughput values of **28.4 Mbps** (downlink) and **26.6 Mbps** (uplink) at a user movement speed of 1 m/s. Furthermore, auto-reconnection times for interrupted links were achieved as follows: less than 1 second for link interruptions of up to 5 seconds, and less than 2 seconds for link interruptions lasting up to 1 minute.

The reduced coverage overlaps in LiFi compared to traditional 5G deployments necessitates frequent handovers but also results in more precise and localized communication. This characteristic, coupled with LiFi's lower power consumption and enhanced indoor security, positions it as an effective alternative to RF-based solutions, particularly in controlled indoor environments requiring stringent energy efficiency and security.

5 IMPACT OF MONITORING PLATFORMS

In this section, we first introduce the **reference distributed monitoring architecture** that has been developed in the framework of this project, and its feasibility assessed in other WPs. Then, assuming such architecture, **two different impact studies** numerically evaluating the impact and benefits of such architecture are presented. In particular, the use of **intelligent data aggregation** allows **increasing the amount of observation points** that collect telemetry data (and their telemetry frequency) without exceeding the capacity of current serial interfaces devoted to telemetry data collection [Vel23]. Moreover, the distributed telemetry architecture enables scalable **dynamic optical capacity management** in point-to-multipoint connection, which leads to **remarkable energy consumption reduction** [Sha22].

5.1 REFERENCE TELEMETRY ARCHITECTURE

Figure 36 presents the reference network scenario, where an SDN architecture controls several optical nodes, specifically optical transponders (TP) and reconfigurable optical add-drop multiplexers (ROADM), in the data plane. Note that the SDN architecture might include a hierarchy of controllers, including optical line systems and parent SDN controllers. A centralized telemetry manager is in charge of receiving, processing and storing telemetry data in a telemetry database (DB). Some data exchange between the SDN control and the telemetry manager is needed, e.g., the *telemetry manager* needs to access the topology DB describing the optical network topology, as well as the label switched path (LSP) DB describing the optical connections (theses DBs are not shown in Figure 36). Every node in the data plane is locally managed by a node agent, which translates the control messages received from the related SDN controller into operations in the local node and exports telemetry data collected from observation points (labeled M) enabled the optical nodes.

A detailed architecture of the proposed telemetry system is presented in Figure 37, where the internal architecture of *telemetry agents* inside node agents and the telemetry manager is shown. Internally, both, the telemetry agent and manager are based on three main components: *i*) a *manager* module configuring and supervising the operation of the rest of the modules; *ii*) a number of modules that include *algorithms*, e.g., data processing, aggregation, etc. and *interfaces*, e.g., gRPC; and iii) a *Redis DB* that is used in *publish-subscribe* mode to communicate the different modules among them. This solution provides an agile and reliable environment that simplifies communication, as well as integration of new modules. A gRPC interface is used for the telemetry agents to export telemetry to the telemetry manager, as well for the telemetry manager to tune the behavior of algorithms in the agents.

Let us describe now a typical telemetry workflow valid for a wide range of use cases. The node agent includes modules (denoted data sources) that gather telemetry data from observation points in the optical nodes. Examples include optical spectrum analyzers (OSA) in the ROADMs and data from digital signal processing, e.g., optical constellations, in the TPs, as well as the traffic (bitrate) collected at the receivers. A telemetry adaptor has been developed, so data sources can export collected data to the telemetry system; specifically, the adaptor receives raw data from the data source and generates a structured json object, which is then published in the local Redis DB (labeled 1 in Figure 37). The periodicity for data collection can be configured within a defined range of values. Several algorithms can be subscribed to the collected

measurements. For simplicity, let us assume that only one algorithm is subscribed, which processes the measurements locally. Such processing might include doing: *i*) no transformation on the data (null algorithm); *ii*) some sort of data aggregation, feature extraction or data compression; or *iii*) some inference (e.g., for degradation detection or traffic prediction). The output data (transformed or not) are sent to a gRPC interface module through the Redis DB (not shown in the figure) (2), which conveys the data to the telemetry manager. Because gRPC requires a previous definition of the data to be conveyed, our implementation encodes the received data in base64, which allows generalization of the telemetry data to be conveyed. Note that, although such encoding could largely increase the volume of data to be transported, intelligent data aggregation performed by telemetry agents could reduce such volume to a minimum.

In the telemetry manager, the data are received by a gRPC interface module that publishes them in the local Redis DB, so subscribed algorithms can receive them. The algorithms in the telemetry manager can implement functions related to data aggregation, inference, etc. Once processed, the output data is published in the local Redis DB (4) and can be stored in the telemetry DB (5) and/or be exported to external systems (6). Interestingly, algorithms in the telemetry manager can communicate with those in the telemetry agents using the gRPC interface (7-8). Examples of such communication include parameter tuning, among others.
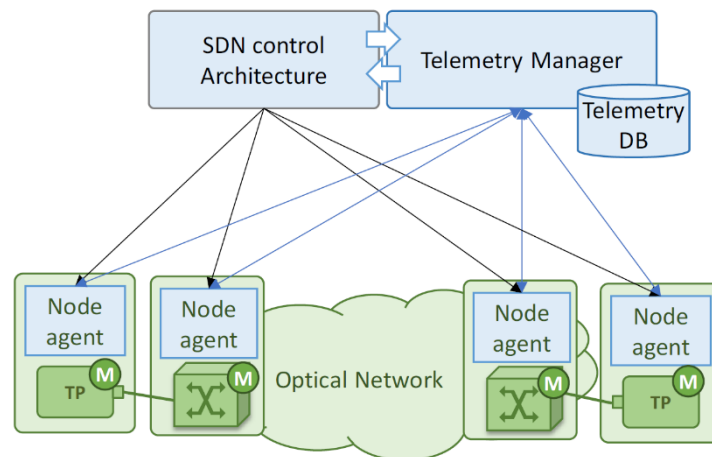

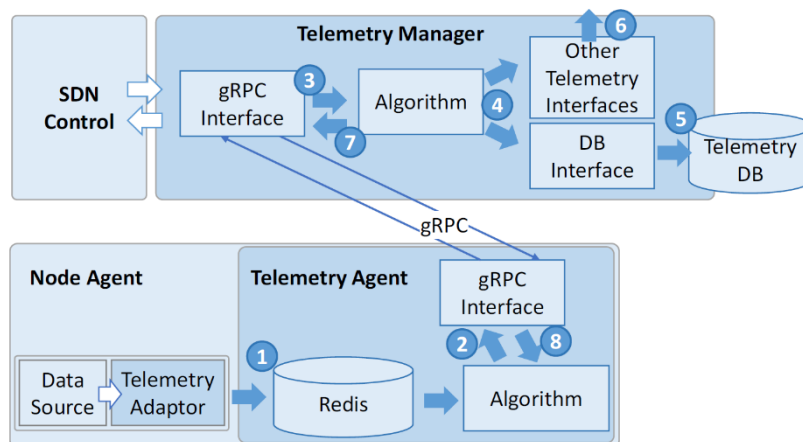*Figure 36: Reference network architecture with support of hierarchical telemetry platform*

Figure 37: Detailed telemetry architecture: manager and agent components

5.2 INTELLIGENT TELEMETRY DATA AGGREGATION

In this section, the distributed telemetry system proposed in the previous section is used to deploy intelligent data aggregation on optical constellations telemetry, which largely reduces data rate without introducing significant error. This remarkable and efficient reduction, jointly with the explosion of monitoring (observation) points expected for the near future, enables achieving target high volumes of collected and processed monitoring data. The contents of this section are based on those published in [Vel23].

5.2.1 Methodology

Let us focus on introducing several techniques to greatly reduce the data volume that needs to be conveyed through the gRPC interface connecting telemetry agents to the manager. In particular, we analyze: *i*) *data compression* using autoencoders (AEs); *ii*) *supervised feature extraction*; and *iii*) *data summarization* using the arithmetic mean of a number of observations. For this example, let us assume the case where the observation point is in a TP, which gathers the received optical symbols of a m-QAM signal. The related data source then, periodically retrieves a constellation sample *X* (a sequence of *k* IQ symbols as represented in Figure 38(a) for a 16-QAM signal) and publish it in the local Redis DB.

Let us start with the use of AEs, a type of neural network with two components: the *encoder*, which maps input data into a lower-dimensional latent space, and the *decoder*, which gets data in the latent space and reconstructs the original data back. Once trained, the autoencoder takes as input 2×*k* values from the received constellation sample and generates the latent space *Z*, where the size of *Z* is significantly lower than that of *X* (Figure 38(b)). In this case, the encoder runs as an algorithm module in the telemetry agent and exchanges *Z* for every input sample *X* with the decoder running in the telemetry manager through the gRPC interface. The algorithm in the telemetry manager uses the decoder to reconstruct the constellation sample and it stores the result in the telemetry DB.

Let us now consider supervised feature extraction, applying *Gaussian Mixture Models* (GMM) [Rui22] to characterize each constellation point of an optical constellation sample as a bivariate Gaussian distribution (Figure 38(c)). Therefore, each constellation point is characterized by 5 features: the mean position in *I* and *Q* axes (μ), as well as the *I* and *Q* variance and symmetric covariance terms that the symbols belonging to the constellation point experience around the mean (σ). Therefore, for an m-QAM signal, m*5 features need to be propagated from the telemetry agent to the manager.

With the two previous intelligent data aggregation techniques, telemetry data is propagated from the observation point to the telemetry manager with the same frequency, i.e., every time a new constellation sample is collected from the observation point, a subset of data representing it is generated and conveyed to the telemetry manager. Assuming a high collection frequency, this policy entails large volume of data being conveyed. However, in normal conditions, this is not needed in general. Hence, we could measure variations in the computed features to decide whether a representation of the new sample needs to be sent to the telemetry manager. In case of no significant variations in the features, the telemetry agent can send averaged values of the features with a much lower frequency, thus reducing the volume of telemetry data being conveyed.
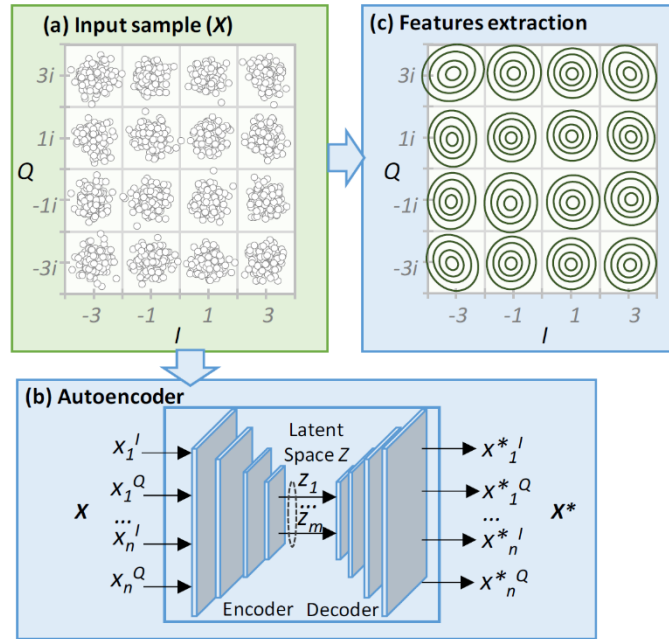
Figure 38: Constellation sample (a), use of autoencoders (b) and supervised features extraction (c).

5.2.2 Results

The telemetry agent and the telemetry manager have been implemented in Python and deployed as containers in two different virtual machines. InfluxDB 2.4 implementing the telemetry DB was deployed as a separated container. A data source was developed that emulates constellation samples collection from an observation point in a TP (available in [Rui22b]). Each constellation sample X includes k=2048 symbols from a 16-QAM optical signal. In consequence, the size of each sample X is 2×2048×4 = 16,384 bytes (B), assuming that every symbol is represented with two scalars (I and Q) of 32 bits. The telemetry adaptor in the data source publishes samples X encoded as a json object. A representation of the json object is shown in Figure 39 identified with the same label as the related message in Figure 38 for the sake of clarity.

{
  "X": [[-3.08519822419515, 2.984674519523211],
        ⋮
        [2.96258763128303, 2.979845582996481]]
}

{
  "Z": ["2.732774257",
        ⋮
        "0.172829926"]
}

{
  "F": [["-2.971842458","2.971601309","0.004633636",..."0.004507746"],
        ⋮
        ["-2.941472597","2.931215828","0.113045212",..."0.121031438"]]
}

Figure 39: Examples of json-based telemetry messages

Algorithms have been implemented in Python and deployed in the telemetry agent and manager for the intelligent data aggregation techniques detailed above. In case of using AEs for data compression, the encoder runs in the telemetry agent, whereas the decoder runs in the telemetry manager. The algorithm in the telemetry agent is subscribed to messages from the data source, so it takes as input a constellation sample X and generates the latent space Z representing it. We have trained the AE for the maximum compression that produces a reproduction error in the decoder lower than 2%, which results in vectors Z of size 32. Such vectors are output as json objects, where each component of the vector is represented as a string with 11 characters, resulting is 455 characters in total for the json object (2a in Figure 39). The json object is then compressed, so each character uses only 1B and encoded in base64, which results in 607B. When the message arrives at the telemetry manager through the gRPC interface, it is used as input to the decoder in the related algorithm. The decoder generates a

sample *X**, which is finally stored in the telemetry DB. In our tests, both data encoding and decoding took 60ms.

In the case of supervised feature extraction, the algorithm in the telemetry agent applies GMM fitting to every constellation sample *X* received and generates outputs of *m*=16 vectors with 5 features each (denoted *F*). This process, outputs a json object with 1,159 characters (2b in Figure 39), which is then conveyed through the gRPC interface using 1,545B. To compare the results of features extraction to those from the autoencoder, the algorithm in the telemetry manager samples each distribution to obtain constellation samples with 2,048 symbols, and stores them in the telemetry DB.

Figure 40 presents the telemetry data rate when the telemetry period ranges from 1s to 1min for gRPC messages with: *i*) samples *X* using scalar values; *ii*) *Z* vectors with the latent space encoded as json objects; and *iii*) features *F* encoded as json objects. The inset in Fig. Figure 40 summarizes the size of every object. We observe that using constellation samples for the telemetry results in extremely large data rates, which limits the telemetry period. The reason is double; on the one hand, high data rates would require expensive data communication infrastructure dedicated for network telemetry, and on the other, optical devices (in this case, the TP) would need to support them, which might impact its performance. Therefore, assuming a **maximum data rate for telemetry collection of 9600 b/s** (e.g., for a typical serial interface), the minimum telemetry period for optical constellations would be 14.5s. With such period, the **telemetry data rate reduces one order of magnitude** to only hundreds of b/s.
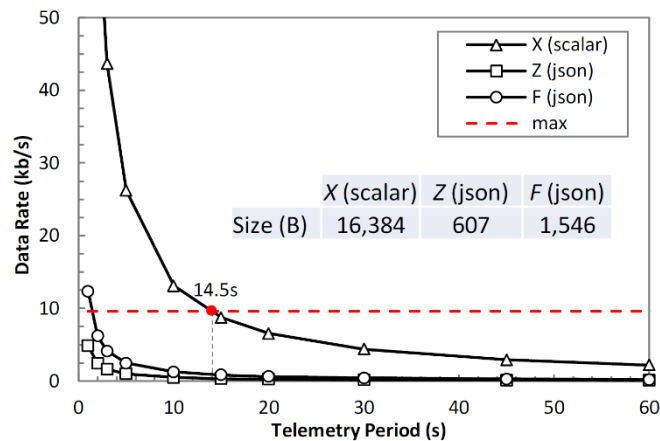
Figure 40: Telemetry data rate vs period

Telemetry data rate can be further reduced by implementing data summarization on the extracted features, which can be sent with a larger period in case no significant changes occur. To illustrate this, Figure 41 shows the relative maximum difference of features *F* when the telemetry period ranges 1-30 s, assuming collection period of 1s. Telemetry data of two lightpaths of 800km and 1600km are shown. In both cases, increasing the telemetry period above 20 s achieves negligible aggregation error under 2%.
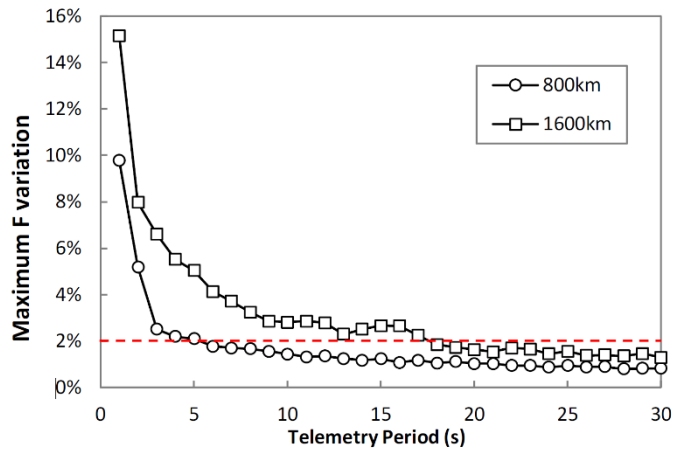
Figure 41: Aggregation error vs telemetry period

5.2.3   Achieved KPI

We can conclude that having fine grain telemetry for network data analysis at a centralized location results in a large amount of data to be conveyed from the devices. To solve that fact, a distributed telemetry architecture has been proposed, where collected data is analyzed before sending them to the central location. Intelligent data aggregation has been shown for optical constellations telemetry, where aggregation introduces negligible error.

The proposed distributed monitoring architecture, together with the different methods for intelligent data aggregation (compression, feature extraction, and summarization) allows **processing 1 order of magnitude more monitoring data** than current centralized monitoring platforms **without extending the capacity of data communication infrastructure**. This increase can be obtained by increasing the number of observation points (e.g., monitored lightpaths), as well as reducing telemetry intervals (from minute/s to few seconds). Hence, the **committed KPI 5.1** (*10x more physical monitored data than what is today available in the field*) is achieved.

5.3   ENERGY-EFFICIENT OPTICAL CAPACITY ALLOCATION

By means of the proposed telemetry architecture, efficient and scalable **dynamic operation of optical connections** is achieved. In particular, in this section we focus on the problem of dynamically assigning optical capacity in Digital Subcarrier Multiplexing (DSCM) systems for multipoint-to-point (P2MP), i.e., where the edge nodes (Tx) demand a variable number of subcarriers SCs as a function of the **local traffic** being conveyed to the hub node (Rx). Thus, distributed telemetry agents are used to **monitor actual traffic** of the P2MP connection, which is a needed input to decide the actual spectrum allocation of hub and edge nodes at every time instant. Results show that dynamic SC management supported on **local (distributed)** monitoring and **global (centralized)** decision making allows both **capital and energy cost reduction.** The contents of this section are based on those published in [Sha22].

5.3.1   Scenario and Methodology

Figure 42a illustrates a P2MP optical connection based on DSCM, where *n* Txs at the edge nodes communicate with a single Rx at the hub node. Every Tx has a portion of the spectrum, i.e. wavelengths, assigned (dotted lines), where its SCs are allocated. The SCs of every Tx are aggregated using, e.g., an optical coupler. It is worth noting that Rx needs to support the aggregated number of SCs. A possible example would be 4 Tx supporting 4 SCs each, and one Rx supporting 16 SCs in total. Although it would be possible that the Tx could allocate every SC in a

59

different part of the optical spectrum, we assume that this is not possible, to reduce the cost of the Tx, and all the SCs need to be allocated in a small portion of the spectrum, named channel, with minimum width to support the required SCs.

Figure 42(b) summarizes our approach, where the channel assigned to every Tx might overlap with that of other Tx; we name this *spectrum oversubscription*. The objective is to increase the number of Txs participating in the P2MP connection. In the first case in Figure 42(b) (labeled 1), spectrum oversubscription is observed between the channel assigned to Tx1 and Tx2 (wavelength 4), as well between Tx2 and Txn (wavelength 7). Note that Tx1 has a SC active in wavelength 4, whereas wavelength 7 is not in use. Let us imagine that Tx2 needs to allocate a new SC to cope with some increment of traffic. Such SC must be allocated inside the assigned channel, which in this case is possible as wavelength 7 was available (2). At this time, Tx2 cannot allocate new SCs since all the wavelengths in the assigned channel are being used. Therefore, a reconfiguration in the neighboring assigned channel (that for Tx1 or Txn) can be tried. In (3), the channel assigned to Txn has been reconfigured, as well as the allocated SCs (SC in wavelength 8 has been deactivated and SC in wavelength 10 activated). In consequence, wavelength 8 has been released and a SC Tx2 can allocate the needed SC.
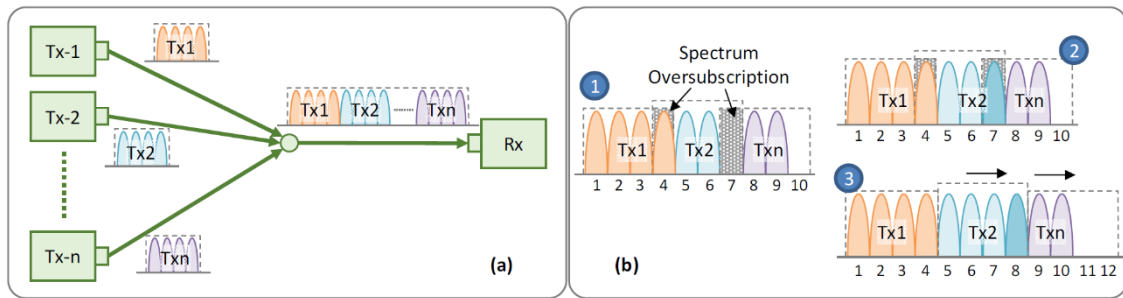
Figure 42: P2MP connectivity based on DSCM (a) and dynamic SC allocation and reconfiguration.

To solve the dynamic allocation/deallocation of SCs based on local traffic monitoring, the following problem needs to be globally solved:

Given:

> • the total spectrum available for the P2MP connection, represented by ordered set W = $\{w_1, w_2, …, w_{|W|}\}$, where $|W|$ is the maximum number of wavelengths supported by the Rx.

> • the set of candidate channels described by set C = $\{c_0, c_1, c_2, … c_{|C|-1}\}$, where c_0 is the empty set and every c_i (i:1..$|C|$- 1) is a subset of contiguous wavelengths of size 1..m, being m the maximum number of wavelengths supported by each Tx. We assume all Tx with the same characteristics.

> • a set of Txs T=$\{t_i, t_2, .., t_n\}$, where every Tx t has an associated capacity requirement k_t.

Output: the configuration of every wavelength and its assignment to every Tx, and the channel assigned to every Tx.

Objective: 1) minimize the amount of lost traffic; 2) to minimize the number of used SC, thus minimizing energy cost; and 3) minimize the number of SCs that are reconfigured.

5.3.2 Results

A simulation scenario was set up following a similar architecture that that outlined in Figure 42, with up to 8 Txs and 1 Rx; Txs can support up to 4 SCs and the Rx up to 16 SCs. For simulation purposes we assumed that every SC is configured with 16QAM, 11 Gbaud, and 60 Gb/s capacity. The simulator was developed in Python, including an integer linear programming (ILP) model implemented by using the PuLP package (details of the ILP can be found in [Sha22]).

To simplify the discussion, we consider two extreme scenarios with Txs with traffic following similar daily patterns (see Figure 43); in Figure 43(a) the traffics are almost in-phase, whereas in Figure 43(b) they are in opposite phase. To study the effects, we define traffic multiplexing ratio as a way to quantify the phase synchronization of the traffics generated by the Tx (0≡in-phase and 1≡opposite-phase). Note that the traffic volume in the peak entails that Txs will require allocating 4 SCs.
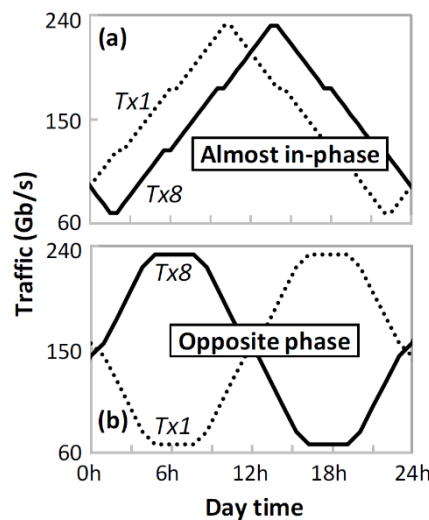
Figure 43: Traffic Scenarios

The **dynamic SC allocation** was compared against a **static SC allocation** in which a maximum of 4 SCs would be used by each Tx, independently of the traffic seen. Additionally, contiguity was relaxed in the ILP model for comparison purposes, representing a bound for the reallocation method.

The proportion of lost traffic (traffic rejected over incoming traffic) for the almost in-phase traffic scenario is presented in Figure 44(a). As for the static method (not shown in the figure), the dynamic and bound ones are able to support 4 Txs without loss. Traffic loss appears when the number of Txs increases, since all the Tx require allocating 4 SCs simultaneously. Interestingly, the **dynamic** and bound methods are **able to support 5 Txs without traffic loss** under the opposite phase traffic scenario in Figure 44(b). The inset in the figure summarizes the gain w.r.t. the static method in terms of number of Txs and supported traffic. As can be seen, the **dynamic method** is able to produce **remarkable gains compared to the static one**.

Figure 44(c)-(d) show the average number of SC reconfigurations per Tx to avoid conflicts from spectrum oversubscription. Under the opposite phase traffic scenario, about 10 reconfigurations were necessary to support 5 Txs without traffic loss. Hence, a **relatively small number of reconfigurations translates to a large amount of gain**.
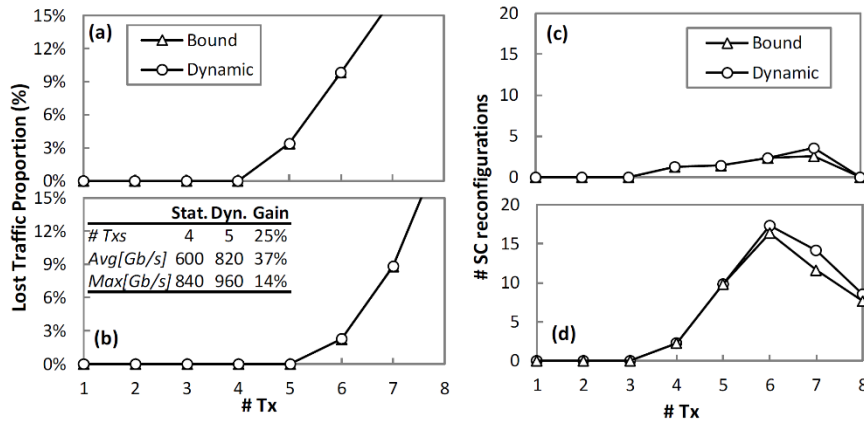
Figure 44: Dynamic vs Static Performance Analysis

Finally, let us study the energy consumption for the two extreme traffic scenarios in a configuration with 4Txs. The number of SCs in use and the power savings compared to the static method are presented in Figure 45(a) for the almost in-phase and Figure 45(b) for the opposite phase scenarios. As expected, **power savings** are concentrated during off-peak periods under the almost in-phase traffic scenario, whereas they are more spread under the opposite phase one, being **around 20% on average under both scenarios**.
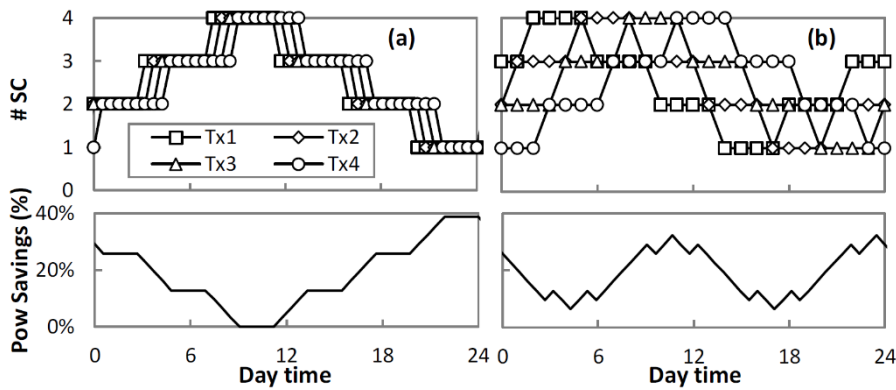
Figure 45: Power Consumption Analysis

5.3.3   Achieved KPI

In this study, we showed that **dynamic SC allocation based on local traffic monitoring** brings significant capital and operational cost reduction in P2MP connectivity, as compared to the static SC allocation. In particular, **energy consumption savings around 20% are observed,** which allows accomplishing with the **committed KPI 5.2** (*20% OPEX reduction (in combination with O8 and ZTN) by minimizing the power consumption impact of this massive new monitoring platform*)

5.4 SUMMARY

This section introduced the **reference distributed monitoring architecture** proposed in this project, and presented two different impact studies to evaluate its performance in terms of related KPIs:

- **Intelligent data aggregation** allows processing 1 order of magnitude more monitoring data that current centralized monitoring platforms without extending the capacity of data communication infrastructure. Consequently, this impact study served as means of

verification of **KPI 5.1**: 10x more physical monitored data than what is today available in the field) is achieved.

- **Dynamic optical capacity management based on local monitoring** allows accurate and efficient allocation of SCs according to actual traffic needs, which in P2MP connections open the opportunity to effectively explore oversubscription. Such dynamic operation led to remarkable savings in terms of energy consumption, i.e., 20% in average for several traffic scenarios. Hence, this impact study served as means of verification of **KPI 5.2**: 20% OPEX reduction (in combination with O8 and ZTN) by minimizing the power consumption impact of this massive new monitoring platform.

6 Disaggregation and packet-optical integration

In this section, we overview the impact of one of the key control-plane support aspects of B5G-OPEN: packet optical integration. Through enabling control solutions to seamlessly operate optical interfaces in packet optical boxes, the project opens more possibilities to deliver solutions with lower cost to deploy and maintain. This is achieved mostly by reducing the floorspace and power of chassis devoted only to optical equipment to a minimum, while leveraging the increasing capacity of routers, as well as the capabilities of next-generation optical pluggables, to deploy common platforms.

6.1 IPoWDM Paradigm

The recent evolution of transmission technology has driven the introduction of pluggable transceivers provided with a coherent detection strategy. Coherent transceivers are commercially available at rates of 400 Gbit/s in quad small form factor pluggable double density (QSFP-DD). Originally implemented for data center interconnection (DCI, up to 120 km reach) with a signal launch power of up to −10 dBm (400ZR), they rapidly evolved to support higher transmission power and longer optical reaches (400ZR+). For example, 400ZR+ QSPF-DD products have been successfully validated and deployed over few hundreds of kilometers relying on an output power of around 0 dBm. Furthermore, 800ZR+ transceivers have been recently commercialized, still relying on compact QSFP-DD (and OSFP) form factors.

All these types of pluggable coherent modules are suitable for metro-core reach (see Figure 46).

Lower cost and reach coherent pluggable modules are currently in an early commercial phase (100ZR [100ZR]) with reduced performance and in a QSFP form factor. These pluggable are ideal candidates for metro-aggregation reach (see Figure 46).

In the meantime, the Optical Internetworking Forum (OIF) has successfully defined the Common Management Interface Specification (CMIS) with related extensions for coherent modules, Coherent CMIS (C-CMIS). CMIS is the management interface of choice for pluggable modules, supported by more than 10 Vendors with excellent interoperability performance.

These coherent modules represent an extremely attractive solution to be equipped directly within packet switching devices, including those designed for the wider data center market.
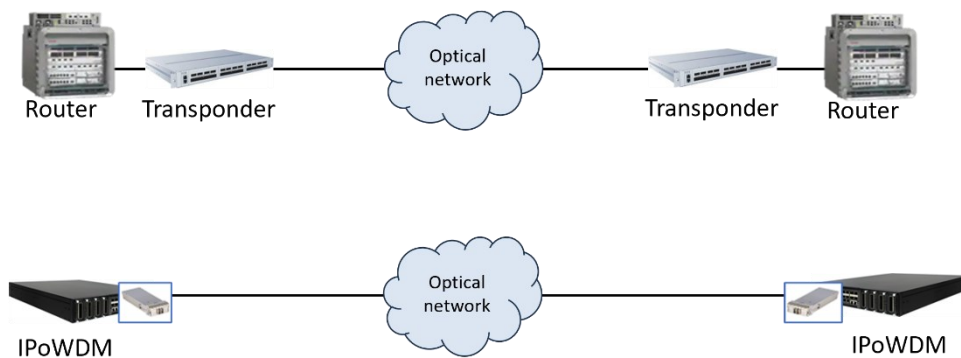

Figure 46: Evolution from Transponder-based optical networks to IPoWDM nodes equipped with coherent pluggable modules.

In B5G-OPEN, we specifically investigated the use of packet-optical nodes (typically called IPoWDM) in the Telco context, i.e. beyond the scenario of DCI. In particular, we have focused on the reduction/removal of transponders and muxponders as standalone network elements particularly in metro networks (see figure above).

The adoption of IPoWDM nodes leads to several remarkable benefits:

- reduced capital expenditure, through the elimination of expensive components like Flex-switchponders and possibly ROADMs and amplifiers in the OLS. The OLS comprises between 20-35% [Her20b] of the total CAPEX in a MAN, so only this part offers important savings opportunities.
- reduced space in central offices, relying on a single IPoWDM box instead of two standalone elements with related interconnected fibre cables.
- reduced latency, since the queuing+processing+transmission of IP packets through 400 Gbit/s (and above) coherent pluggables will be in the order of $1 - 2$ microsecs at most, very small compared with propagation delay [Kon24].
- reduced power consumption by avoiding the optical–electronical–optical (OEO) interconnection between gray router interfaces and colored transponder line interfaces (overall savings in the range between 50 and 150 W for every 100 Gbit/s of nominal traffic, depending on the line rate).
- tight integration between packet and optical networks, which is of special interest as transport is dominated by Ethernet and IP traffic.
- Introduction of advanced monitoring capabilities leveraging on programmable ASIC, as detailed in this document.

6.2 TECHNO-ECONOMIC COMPARISON OF PLUGGABLE OPTICAL INTERFACES AND STAND-ALONE TRANSPONDERS

Progress in CMOS process technology, e.g., 7 and 5 nm nodes, has enabled a new type of purpose-build pluggable and interoperable coherent transceivers. Following the seminal 400ZR implementation agreement (IA) [400ZR], targeting high-capacity data center interconnect (DCI) applications that in the past relied interfaces based on intensity-modulation combined with direct-detection (IM-DD), several multi-source agreement (MSA) initiatives have been defining extensions and improved specifications to foster the adoption of coherent pluggable transceivers in applications beyond DCI, including the Open XR Optics Forum [OXR], the OpenZR+ [OZR+] and OpenROADM [OR]. This development holds the promise of expanding the application of pluggable coherent transceivers to metro and regional networks. These networks impose longer reach requirements and are often also operated at high loads and have been a natural fit for high-performance embedded coherent transceivers [Ped22]. However, ongoing evolution of pluggable coherent transceivers, e.g., revised OpenZR+ spec, which defines higher values for output power and transmitter OSNR, may enable to benefit in these networks from the lower cost, lower power consumption and smaller footprint inherent to these devices. Moreover, this would also allow us to adopt an IP-over-DWDM architecture in these network segments. Figure 47 illustrates the three main coherent transceiver deployments that can be envisioned and have been considered in the study reported here. The first two options rely on having a dedicated transport box (line card) that either has embedded transceivers (a) or pluggable transceivers (b). The third option eliminates the need to have line cards and the grey

65

interfaces interconnecting it with a router / switch by hosting the pluggable coherent transceivers directly in the router or switch.
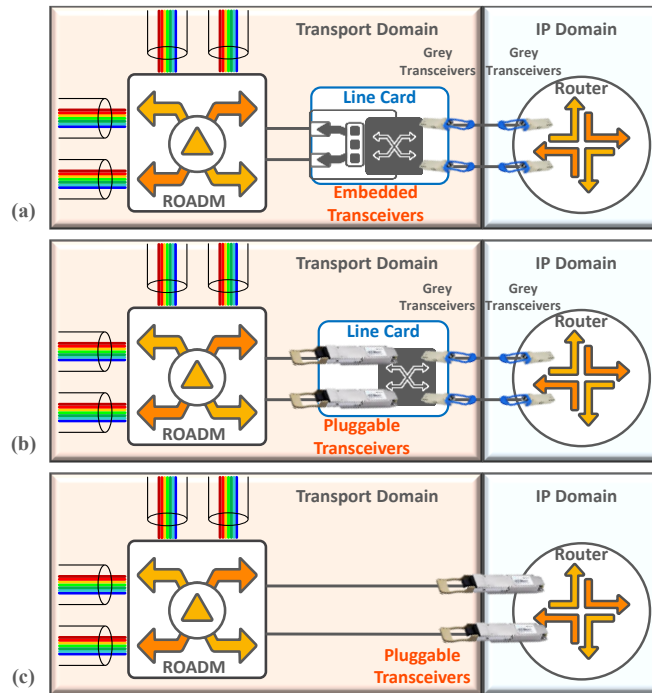

Figure 47: Network architecture: (a) line card with embedded transceivers; (b) line card with pluggable transceivers; (c) pluggable transceivers directly in routers.

The Spanish national network comprising 30 ROADM nodes and 56 bidirectional links (average length of 148.5 km) with a total of 122 bidirectional standard single mode fibre spans (average length of 68.1 km) is used. ROADM nodes are assumed to have an architecture based on a route-and-select (R&S) express layer using 1×20 wavelength selective switches (WSSs) with insertion losses (ILs) of 6.5 dB and a colorless, directionless and contentionless (CDC) add/drop layer using 8×6 multicast switches (MCSs) with ILs of 10.5 dB. Erbium-doped fibre amplifiers (EDFAs) used as both pre-amplifiers and booster-amplifiers at the ROADM nodes, as well as in-line amplifiers are considered to have a noise figure (NF) of 6 dB in the target gain regions. The 4.8 THz of the extended C-band is assumed to be available for transmission. The offered traffic load to the network is scaled from the baseline traffic spatial distribution defined by Telefónica in [IDE-D1.1]. Under the assumption of shortest distance path routing, the average length per demand request is 385 km (with minimum and maximum values of around 143 and 877 km). To simulate an extended period of network operation, a progressive loading of the network is enforced: a total of 4 years of network operation and a yearly traffic growth of 25% are considered with a new set of 400 GbE traffic demands arriving every 4 months. The provisioning framework used to route traffic demands and calculate the required resources, including line cards and pluggable transceivers, is described in [Ped23]. The quality-of-transmission (QoT) estimation model needed to determine the feasibility of using a given channel format over a specific routing path is also described in [Ped23].

Two types of pluggable coherent transceivers are used in the design exercise: one based on the early OpenZR+ specification, denoted as OZR+ LowPower, and the other based on the updated OpenZR+ specification, denoted as OZR+ HighPower. In both cases, two channel formats are available to transport 400 GbE client signals: a single 400G optical channel using a 60.1 Gbaud carrier, 16QAM modulation format, which is allocated a 75 GHz frequency slot, and two co-

66

routed 200G optical channels using 60.1 Gbaud carriers, QSPK modulation format, allocated a 150 GHz frequency slot. In the case of using an architecture based on having the pluggable coherent transceivers in a dedicated line card, a two-line port solution is assumed. The embedded transceiver solution is based on a two-line port line card with advanced DSP capabilities, which is originally capable of supporting hundreds of channel formats (varying combinations of baud rate and modulation formats). In the case of this study, the channel formats considered are: single-channel 800G (96 Gbaud, 112.5 GHz frequency slot), two co-routed 600G channels (96 Gbaud, 225 GHz) capable to support 3x 400 GbE, two co-routed 600G channels (84 Gbaud, 200 GHz), and single 400G channel in two different configurations: 84 Gbaud, 100 GHz frequency slot and 63 Gbaud, 75 GHz frequency slot. In order to model the power consumption associated with transceivers and line cards, it is assumed that an OpenZR+ pluggable consumes 24 W, a client 400 GbE pluggable consumes 13 W, a line card capable of hosting two OpenZR+ pluggable transceivers consume 70 W (excluding all pluggables) and a line card with two-line ports and embedded transceivers consumes 350 W (excluding client pluggables). Note that a more accurate estimation of power consumption would require to consider the power consumption dependency on factors such as the channel format being used and the temperature of operation. Nevertheless, despite the simplification made on these figures, the results of the exercise should provide a reasonable first estimation of the power consumption savings that can be expected by adopting pluggable coherent transceivers and an IP-over-DWDM architecture. All results reported are the average of 20 independent simulation runs.

Figure 48 plots the power consumption of line cards and pluggable transceivers (line and client) as a function of the total offered traffic load when considering architectures (a) and (b) of Figure 48. As can be seen, there is a significant decrease in power consumption for the same offered traffic load when opting for a pluggable-based solution. Moreover, the results also highlight that very significant savings are realized when using better performing pluggable coherent transceivers, which is a consequence of being able to use more often the more spectral efficient channel format. Taking as reference a total offered traffic load of 70.6 TB/s, the solution based on embedded transceivers has a power consumption of 55 kW. For the same offered traffic load, the power consumption drops to 46 kW and 32 kW when using OZR+ LowPower and OZR+ HighPower transceivers, respectively. This corresponds to a power consumption reduction of 16% (LowPower) and 42% (HighPower) versus the reference case with embedded transceivers.

Figure 48: Total network power consumption of line cards, client transceivers, and line transceivers: embedded vs. pluggable).

The potential to install pluggable coherent transceivers directly in routers (or switches) offers further opportunities to decrease power consumption. Figure 49 shows the expected power consumption as a function of the offered traffic load when considering architectures (b) and (c) from Figure 49. The results suggest that power consumption can be roughly halved by removing the line cards and client interfaces. Therefore, when comparing architecture (c) with architecture (a) the combined power consumption savings can exceed 50%.
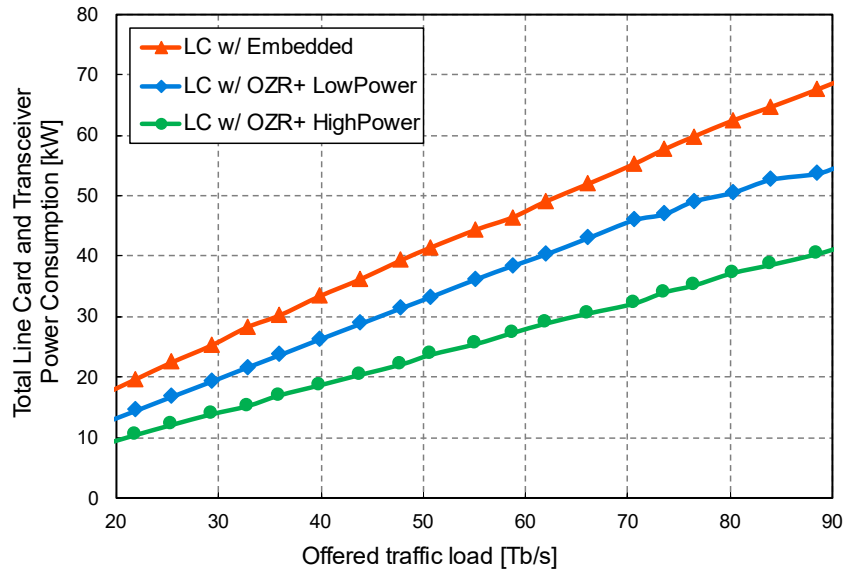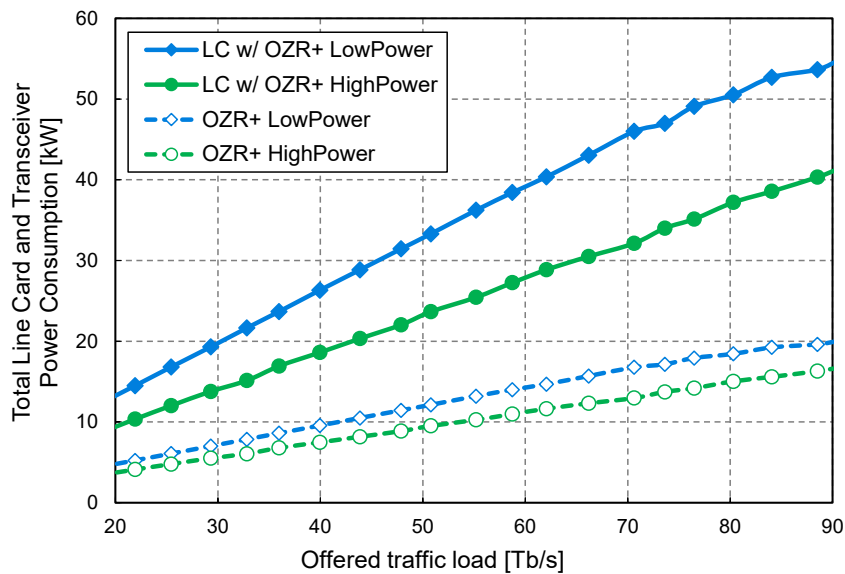

Figure 49: Total network power consumption of line cards, client transceivers, and line transceivers: pluggable transceivers in line cards vs. directly in routers.

7 TECHNO-ECONOMIC BENEFITS OF AUTONOMOUS AND DYNAMIC NETWORKS

7.1 DYNAMIC AND AUTONOMOUS NETWORK ANALYSIS

7.1.1 Introduction

Operator transport networks generate operational expenditures (OpEx) derived from required actions such as operational changes (e.g., configuration of a new service, adding a new node to the network) and failure repair (HW or SW). The actions are typically part of the responsibilities of the Operations, Administration, and Maintenance (OAM) team and involve among others: i) OAM personnel, ii) spare parts stock, in order to perform replacement of damaged parts, if any; iii) Technology suppliers, which provide service support. Some actions that currently require in-person visits to sites have the potential of either becoming remote actions or not being needed any more, provided that a certain level of automation and/or network behaviour predictability is achieved. Indeed, there are reactive actions, which could be avoided (or could turn into preventive actuations) if the aforementioned automation capabilities were available.

Among different network automation capabilities, predictive maintenance aims at avoiding the severe consequences that an unexpected service breakdown caused by a hard-failure can signify for a network operator. Failure management needs to cover: i) *the detection of degradations* (i.e., soft-failures) that do not currently affect the service, before they become hard failures; ii) *severity estimation*, i.e., if they will become hard-failures, and when this would happen. Estimating the severity of soft-failure is a useful tool to plan maintenance; iii) *identification of the root cause*, i.e., what type of device/element is causing the observed degradation; and iv) *localization* of device/element in the network.

The use of optical network digital twins (DT) based on deep neural networks (DNN) to model the propagation of optical signals through a lightpath, from the transmitter to the receiver, have been recently proposed [Ru22]. In this study, we take advantage of developed models and functions in [Dev22] to compare the received signals (X_r) and the expected ones generated by the DT (X_e) in the time and frequency domains; we call that function $diff(X_r, X_e)$. We propose methods that detect degradations by analyzing the evolution of $diff(\cdot)$ in the time and frequency domains and estimate their severity by analyzing the evolution of time domain features. Then, we evaluate the benefits of such anticipation in terms of operator OpEx savings.

7.1.2 Reference Service Support Model

According to the TID service model, technical support services are broken down into different components, which can be separated into two main groups:

- **Basic services**: that are usually contracted as a bundle and include technical assistance center, remote interrogation of equipment, provision of software updates, root cause analysis, and management reporting, among others.
- **Optional services**: that are contracted separately and individually. Belonging to this group, three categories can be distinguished:
    - **First Line Maintenance (FLM)**: engineer to site, to perform corrective actions such as replacement of malfunctioning equipment.

- o **2nd Line Support**: which includes both on site operations, such as primary provision of skilled resources for defect troubleshooting, and remote operations, where typically the vendor is the primary supplier of the troubleshooting support,
- o **3rd Line Support:** on-site support used for those cases where neither an FLM technician nor a 2nd line engineer can solve.

Without loss of generality, we assume that both FLM and 2nd Line Support are paid with an annual fee, whereas 3rd Line Support is usually quoted separately on a per human-hour or working-day basis.

As detailed in D2.1, the operator reference topology consists in a number of regional networks that are interconnected at the national level by means of a backbone infrastructure. From the point of view of maintenance service, the following assumptions are considered in order to accomplish with the committed SLAs:

- A FLM team is required <u>for each region</u>, in order to provide fast response against hard failures requiring on-site technical assistance.
- One single 2nd Line Support can be provided <u>centralized</u> at the national level, since it mainly provides remote assistance

3rd Line Support is also at the national level, but only needed when the <u>other support services cannot deal with the resolution of the event</u>, e.g. a hardware failure suddenly happens while FLM and/or 2nd Line Support are occupied with other scheduled maintenance tasks.

7.1.3 Predictive Failure Management Solution

As mentioned above, the proposed predictive maintenance procedure is based on the use of DT that model lightpaths across regional and national networks. Figure 50 shows an illustrative scenario of a lightpath connecting two remote locations and includes two transponder nodes TP A and TP B, n ROADMs and n-1 optical links with erbium-doped fibre amplifier (EDFA) and single mode fibres (SMF). We assume that every ROADM consists of two wavelength selective switches (WSS) and EDFAs (except the last one). Every optical node is controlled by a local node agent that configures the underlying optical devices and collates telemetry data from them, as well as from OSAs in the case of the ROADMs.

On top of the architecture, a software-defined networking (SDN) controller connects to the node agents and to an optical layer DT modeling the data plane. The DT includes (or it has access to): *i*) a telemetry database (DB), where data collected from the data plane are stored. Such data includes spectral measurements collected from the OSAs in the ROADMs that the lightpath traverses, as well as optical constellations from the coherent receiver in TP B; *ii*) a model DB that includes DNN models for the optical time domain [Ru22] and analytical models that represent filter transfer functions for the frequency domain. With such models, optical propagation through the lightpath can be modeled end-to-end in both time and frequency domain; *iii*) a sandbox domain, that is used to compose the models for the lightpath; and *iv*) a set of algorithms that analyze the features of the signals received and stored in the telemetry DB and compare to those generated by the models in both time and frequency. In this paper, we focus on algorithms for degradation detection and severity estimation.

Two main failure conditions are analyzed: *i*) one single filter-related failure localized in a WSS of an intermediate ROADM; here, two causes of failure are considered: filter shift (FS) and filter tightening (FT). FS or FT failures appear at some point in time and its magnitude increases over

time; and *ii*) the transmitter operates at a sub-optimal launching power and FS failure appears. Note that such non-ideal network condition might make the detection of the degradation and the estimation of its severity more difficult.
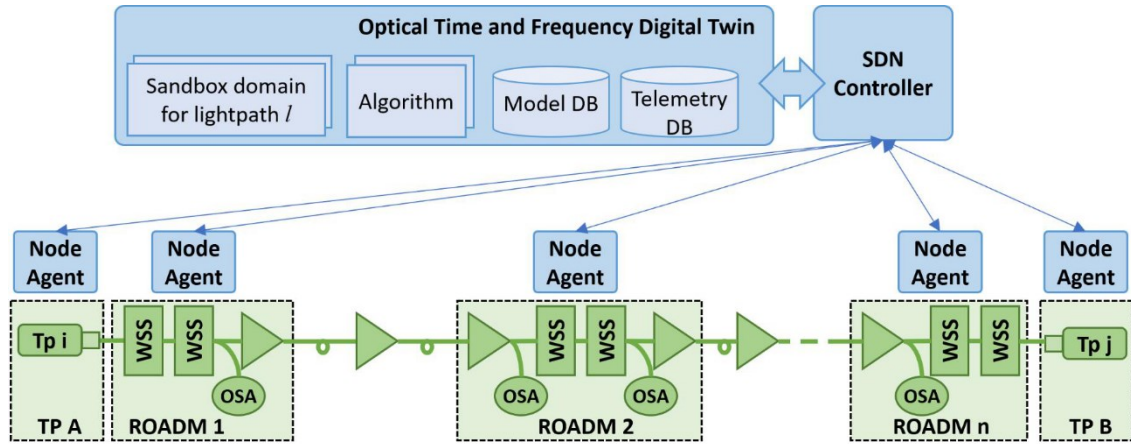

Figure 50: Overview of the envisioned network scenario.

Algorithm I presents the pseudocode of degradation detection at the frequency domain, which is executed in the DT every time that new spectrum S_r samples are received in the telemetry DB from the last OSA in the lightpath. A similar algorithm is executed every time that new constellation C_r is available. The algorithm receives: *i*) the models for the lightpath *ml* that include those for time and frequency domains that were trained in the sandbox domain and stored in the model DB; *ii*) historical DB *hl* with observations for time and frequency and computed diff(·) values; *iii*) a list *O* with the operational parameters used for fitting models; and *iv*) the current time *t*. The expected spectrum S_e is generated using the model for the lightpath (line 1 in Algorithm 4) and used to compare with the received samples (line 2). The diff$_s$(·) function computes the Euclidean norm of the residual vector computed by subtracting S_r from S_e [Sha19]. For the time domain, the diff$_c$(·) function computes the Euclidean distance between the features extracted from C_r and C_e [Ru22]. The results are stored in the historical database (line 3). Next, a linear regression model for the evolution of *diff* is trained with a fitting window of length *T* based on historical data in *hl* and tested over the last measurements for a period Δ*lr* (lines 4-6). The relative root-mean squared error (rRMSE) between the predicted evolution and the observed one is computed and stored (lines 7-8). A threshold is set by applying a margin *k* over the rRMSE moving average in a time window Δ*lr*. This threshold is exploited to detect unexpected behaviors of the analyzed time series. Whenever the threshold is exceeded, a positive detection is returned (lines 9-11).

Algorithm 5 shows the pseudocode of the severity estimation algorithm, which is run as soon as a degradation is detected and then periodically for more accurate results. The algorithm uses the average symbol variance *AvgVar* computed from the received constellation samples C_r, to estimate when the degradation will result in a hard failure. We assume a correlation between *AvgVar* and the BER and then, we can estimate the severity of the found degradation by studying the evolution with time of the former. We claim that the severity estimation by analyzing the received signal in the time domain can be used disregarding whether the degradation is detected in the time or the frequency domains. Then, let us assume that the pre-FEC BER threshold is reached when *AvgVar* reaches some specific value, *AvgVar_th*. The algorithm receives the historical database *hl* and operational parameters *O* as input. The last received

71

constellations are retrieved from *hl* and the observed *AvgVar* time series is obtained (lines 1-2 in Algorithm 5). Time series forecasting is based on two models: polynomial regression and Holt-Winters exponential smoothing trained with a fitting window *Δfr* (lines 3-4). The algorithm identifies the time of service disruption when one of the forecasts exceeds *AvgVar_th* within a given time limit *Tlim* (line 5); the shortest time in which any of the forecasts exceeds *AvgVar_th* is then returned (line 6). Otherwise, no service disruption is considered (line 7).

Algorithm 4. Degradation detection at frequency domain

INPUT: *ml, hl, O, t*	**OUTPUT:** *degradation*
1:	$S_e \leftarrow$ *ml*.generateS()
2:	*diffS* $\leftarrow$ diff$_s$(*hl*.get("Sr", *t*), S_e)
3:	*hl*.append("diffS", *diffS*, *t*)
4:	*diff*[] $\leftarrow$ *hl*.get("diffS", *t-O.Δlr-O.T*, *t-O.Δlr*)
5:	*lrmodel* $\leftarrow$ *lr_fit*(*diff*[])
6:	*Ylr* $\leftarrow$ *lrmodel*(*t-O.Δlr*, *t*)
7:	*Err* $\leftarrow$ rRMSE(*Ylr, hl*.get("diffS", *t-O.Δlr*, *t*))
8:	*hl*.append("ErrS", *Err*, *t*)
9:	ErrS[] $\leftarrow$ *hl*.get("ErrS ", *t-O.Δlr*, *t*)
10:	**if** *Err* > MovAvg(*Errs*[]) * *O.k* **then return** true
11:	**return** false

Algorithm 5. Severity Estimation

INPUT: *hl, O*	**OUTPUT:** *time_disrupt*
1:	Cr[] $\leftarrow$ *hl*.get("Cr", *t-O.Δfr*, *t*)
2:	*AvgVar*[] $\leftarrow$ featureExtraction["*AvgVar*"](Cr[])
3:	*pr_mod* $\leftarrow$ pr_fit(*AvgVar*[])
4:	*ews_mod* $\leftarrow$ ews_fit(*AvgVar*[])
5:	**if** *pr_mod*(*t+O.Tlim*)> *AvgVar_th* OR *ews_mod*(*t+O.Tlim*)> *AvgVar_th* **then**
6:	**return** first_t(*pr_mod, ews_mod, AvgVar_th*)
7:	**return** ∞

7.1.4   Failure Detection and Severity Estimation Results

In order to numerically evaluate the performance of the proposed predictive failure management solution, a simulator of a digital coherent system implemented in MATLAB was employed to reproduce the optical layer. The considered scenario consisted of a lightpath passing through 8 ROADMs and a total fibre length of 1120 km. Each link consisted of 80-km SMFs spans characterized by a fibre loss of 0.21 dB/km, a dispersion 16.8 of ps/nm/km and nonlinear coefficient of 1.3 W^{-1}km^{-1}. A WDM signal with three DP-16QAM@64GBd channels and 75GHz channels spacing was transmitted over the SMF at the optimal launching power of -1 dBm obtained through power sweeping. The pulse propagation was simulated through a split-step-Fourier method (SSFM) with step of 1 km including effects such as group velocity dispersion (GVD), higher order dispersion, polarization dependent fibre loss, arbitrary fibre birefringence, and self-phase modulation (SPM). The cascade filtering penalties are considered employing experimental transfer functions from 1x9 WSS filter with 75 GHz bandwidth. Finally, the EDFAs with ideal gain and 4.5 dB noise figure are considered. At the receiver side, a 4 samples/symbol DAC rate was assumed to reconstruct the signal.

In the simulations, 2^{17}-long bit sequences were generated. For time analysis, constellation points were modeled as bivariate Gaussian distributions and five features were extracted: the mean

and variance of the real and imaginary components, and the symmetric covariance. Finally, *AvgVar* was computed by averaging the real and imaginary variance for all the constellation points. For the frequency analysis, eight features were extracted from the optical spectrum at -6 dB and -3dB: the bandwidth, the two edges and the central channel frequencies.

Figure 51(left) shows the evolution of the failure magnitude for FS and FT in a WSS in an intermediate ROADM. Those failures start after the first week with a small frequency shift or bandwidth, which slightly degrades the optical signal. The magnitude increases linearly during the second week, when the degradation becomes a hard failure. 1 observation per hour was performed (337 in total). Figure 51(right) shows the accuracy achieved by the proposed detection method (Algorithm I) for the three failure scenarios considered, i.e., FS (a), FT (b), and FS + sub-optimal power (c). **Degradation detection was performed with the following parameters O: T=84h (half a week), Δlr = 24h (1 day), Δfr = 96h (4 days) and k=2**. All the three failures were detected in a short time, just a few hours after the failure actually started. Interestingly, the presence of a previous degradation coming from sub-optimal launching power (Figure 51(right(c))) only delays FS detection for a few hours with respect to FS and optimal power (Figure 51(right(a))), which shows the feasibility of these methods to operate under realistic scenarios.
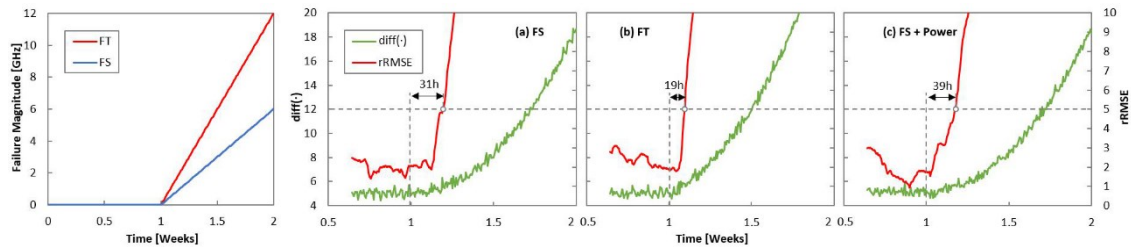
Figure 51: (left) FS and FT failure magnitude; (right) Failure detection using diff(·) for the three failure scenarios

Figure 52(left) shows a strong correlation between BER and the *AvgVar* feature for the studied values and considered failure scenarios. We observe that *AvgVar*~0.2 indicates that pre-FEC BER equals the threshold (1.5×10^{-2}). This result validates the feasibility of using *AvgVar_th* = 1.94×10^{-1} to estimate the severity of the failure in Algorithm 5. With that threshold, Figure 52(right) shows the actual and forecasted time to hard failure for the three use cases, as well as time when the estimation error goes below 8h. In all three cases, **severity estimation progressively converges to the actual time to the failure**. Note that the severity estimation works well under single and multiple failures, since it is based on the analysis of the evolution of the *AvgVar* metric, which is closely related to the actual BER. These results also entail that the failure magnitude can, indeed, be related to the achievable severity estimation accuracy. With such estimation, maintenance can be scheduled with enough time before the degradation becomes a hard failure.
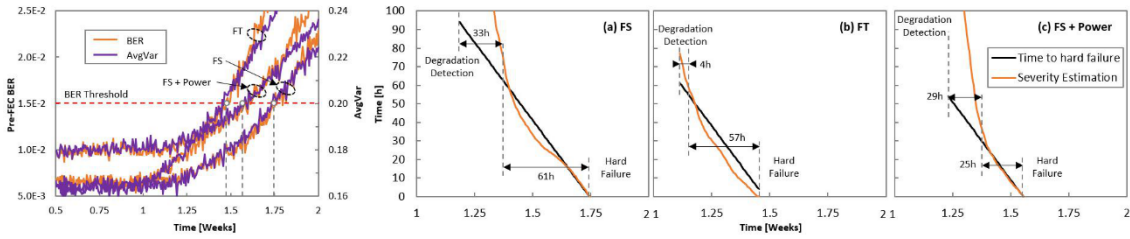
Figure 52: (left)BER vs AvgVar correlation for FS and FT ; (right) Failure detection using diff(·) for the three failure scenarios.

In view of these results, we can conclude that our proposed predictive failure management procedure is able to detect and estimate the severity of different HW soft failures **between 1 and 4 days before they become hard failures.** Assuming this range, let us now evaluate the impact of this predictive operation in terms of availability. Thus, let us consider that an overall stringent availability of 6x9s is required for all the optical connections in a network. This means that total outage time cannot exceed 30 seconds per year for such connection. In addition, let us assume that a dynamic restoration mechanism is implemented to re-route optical connections on demand [Vel17]. This restoration mechanism is triggered either *reactively* (when a hard failure is detected, and actual affected connections must be rerouted) or *proactively* (when a soft failure is detected, and potentially affected connections are rerouted before they experience any service degradation).

Considering the previous lightpath configuration (8 ROADMs and 1120 km), we computed the expected number of two types of failures: *i*) unpredictable fibre cuts, that cannot be anticipated by our mechanism, and *ii*) predictable failures in filters, that can be anticipated. For fibre cut probability, we consider 2.72e-3 cuts/km/year [Vel17], whereas we assume a conservative failure rate of 0.1 for each filter, i.e. one failure every 10 years per component. With these numbers, a reactive operation will need to deal with 1.41 hard failures/year/connection, whereas **anticipating proactively soft failures** will reduce this expectation to **only 0.41 hard failures/year/connection,** which is a **reduction of 70% with respect to reactive operation**. Hence, the impact of the proposed predictive maintenance procedure in increasing availability is clear, since significantly less hard failures affect optical connections with critical disruptions.

In the next section, the proposed predictive maintenance method is considered as an enabler to open the possibility to reorganize service support schemes, that will lead to OpEx savings.

7.1.5   OpEx Savings Quantification

Assuming that the network operator implements the aforementioned predictive maintenance procedure, in this section we quantify OpEx savings derived from such autonomous operation. In particular, we focus on a reference TID topology consisting in 3 regions of 300 nodes each. In this reference topology, and based on TID last year report, the average number of events is 92, where 12 of them correspond to HW failures. Without loss of generality, we assume the same probability of failure in each node of the network, as well as an average time-to-repair of 3 days.

We performed two different case studies to compute OpEx savings based on service support costs. Due to confidentiality reasons, those costs are provided in relative terms.

Case study 1: Centralization of FLM service support

Considering the abovementioned reference topology and the benchmark service model in Section 7.1.2, the OpEx associated to the annual fee of both FLM and 2nd line support can be computed by the equation:

$$OpEx_{benchmark} = 3 * Cost_{FLM} + Cost_{2nd}$$

However, early fault pre-detection (1-4 days before the event takes place) would allow for centralising the whole support resources' structure, enabling OpEx savings by centralizing FLM. In this case, OpEx will be computed as follows:

$$OpEx_{predictive} = Cost_{FLM} + Cost_{2nd}$$

Then, OpEx savings can be computed as follows:

$$Savings = 1 - OpEx_{predictive} / OpEx_{benchmark}$$

For the sake of simplicity and to facilitate the comparison among different options, we normalize the numbers to the cost of FLM, which results into $Cost_{FLM} = 1$ cost units (c.u.) and $Cost_{2nd} = 1.76$ c.u. Then, applying those normalized values, OpEx of benchmarking and predictive options are $OpEx_{benchmark} = 4.76$ c.u. and $OpEx_{predictive} = 2.76$ c.u., respectively. Therefore, applying **predictive maintenance leads to annual OpEx savings as large as 42%** by means of centralizing FLM teams.

Case study 2: Reduction of 3rd Line Support demand

In this study, we compute the additional OpEx savings due to the reduction of the need of 3rd Line support. Recall that, unlike FLM, 3rd line support service is used for those cases where neither a FLM technician nor a 2nd line engineer can solve the problem. This cost is usually kept independent from the size of the supported network, as it is activated by each event which requires it, thus it is also paid on a per-event basis.

In the benchmarking approach, the OpEx increment (ΔOpEx) due to the use of 3rd Line Support services can be computed as follows:

$$\Delta OpEx_{benchmark} = \# failures * daysToRepair * Cost_{hd}$$

where $Cost_{hd}$ is the cost of human-day of that service.

For the sake of simplicity, let us normalize the OpEx from fixed annual services to a value of 1. Then, the additional savings from reducing 3rd Line Support can be computed as follows:

$$Savings = 1 - [1 / (1 + \Delta OpEx_{benchmark})]$$

In a network such as the one in our study, if we consider that 12 failures will occur in one year and that they can be solved within the next 3 (working) days, the **additional OpEx savings due to predictive maintenance will grow to 6.40%.**

7.1.6 Conclusions

In this study, we proposed a predictive maintenance approach that allows the detection and severity estimation of soft failure between 1 and 4 days before they become hard failures. A comparison between reactive and proactive operation modes showed that a **reduction of the number of hard failures of 70%** using the latter when compared to a reactive approach. . This statement, consequently, reduces the total outage time of connections, which increases the availability of existing connections, as well as the number of connections that can be successfully

supported and managed for a target stringent availability (e.g., 6x9s). This study allows **accomplishing with the committed KPI 8.4** (*Improve and guarantee service and network availability*).

Due to this autonomous and predictive failure anticipation, OpEx savings can be derived by reorganizing maintenance service support. On the one hand, **annual OpEx savings up to 42%** are observed by centralizing FML services that typically require regional resource support. On the other hand, **additional OpEx savings around 6%** are obtained by reducing the utilization of 3rd Line Support services. This study allows **accomplishing with the committed KPI 8.3** (*Reduce OpEx by >20%, by increasing autonomous operations and reducing manual intervention*)

Besides the computed OpEx savings, other savings can be derived from predictive maintenance:

- With the first case (FLM + 2nd line support), an early fault pre-detection has been shown to lead to a simplification of the services structure. If we add automation to this capability, we could allow ourselves to relax the level of required services (e.g., a Gold Minus or Silver instead of Gold; this change might be translated into direct savings from the contracted service. Since negotiation strategies are quite flexible and are adapted to the conditions of each context at a given moment, it is hard to estimate the achievable savings.
- The second case is related to OAM personnel visits to site(s). By having an early fault pre-detection tool, visits to site(s) could be planned (in case needed, as mentioned in previous section), avoiding specific resources' trips (i.e., "point to point") and allowing rounds, saving distance, time and costs. Savings depend on the location of each site, location and cost of OAM personnel, distances to cover, road conditions, etc., so savings are quite hard to estimate here as well.
- Finally, the last case is related to warehouses (either owned or suppliers'). An early fault pre-detection tool and automation capabilities might allow smaller, more centralised warehouses. In other words, a more efficient warehouse management.

7.2   TECHNO-ECONOMICS OF P2MP VIA DYNAMIC CLUSTERING

In deliverable D4.3, section 3.1 demonstrates the application of clustering algorithms for finding optimal clusters or groups of nodes with uncorrelated traffic patterns. This algorithm is applied to P2MP tree architectures where multiple leaf nodes are interconnected with a master hub node via Digital Sub-Carrier Multiplexing (DCSM). In such P2MP architectures, a single central node is designed to be interconnected with multiple leaf nodes in a P2MP tree topology with only passive devices like optical splitters in between. The tree is provided with 16 subcarriers operating at 25 Gb/s such that different bandwidth settings can be configured between the central node and each leaf of the tree, depending on bandwidth requirements. This bandwidth assignment flexibility can be exploited to allow simplified topologies in metropolitan area networks (MANs) and has direct applicability in 5G/6G deployments.

Thanks to hierarchical clustering, efficient P2MP tree topologies can be designed to favor uncorrelated traffic patterns, where nodes with daily peaks coexist together with other nodes having peak traffic in the evening for example. This is shown in Figure 53.
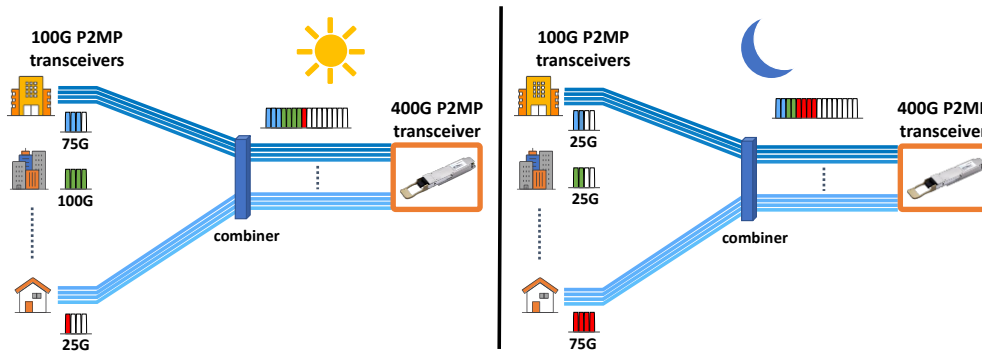
Figure 53 Dynamic allocation of subcarriers at different times of the day (top) in the morning (bottom) at night.

Essentially, the 16 x 25Gb/s channels can be assigned to clients in a dynamic fashion moving channels from one client to another as needed, according to dynamic traffic demands, thus allowing to provide extra resources to specific clients during his/her peak hour,

Clustering is a well-known unsupervised ML method for grouping elements based on a similarity or distance metric. It is used to reveal subgroups of similar structure within a set of unlabeled data, where each individual cluster has some homogeneity compared to the rest of the data. Essentially, clustering algorithms aim at partitioning data into groups such that the elements within the group are highly related or show minimal distance within the group, while the distance between groups is maximized.

As shown in [Xu16], there are four major traffic profiles identified in the 9,600 cell towers studied in the city of Shanghai, see Figure 54. As observed, different traffic profiles exhibit peak and valley times at different times of the day. For example, the residential profile has its peak time between 8 p.m. and 23 p.m. while the office traffic profile shows the peak between 9 a.m. and 4 p.m. Interestingly, the transport traffic pattern has two peaks, one before office hours plus another one after work
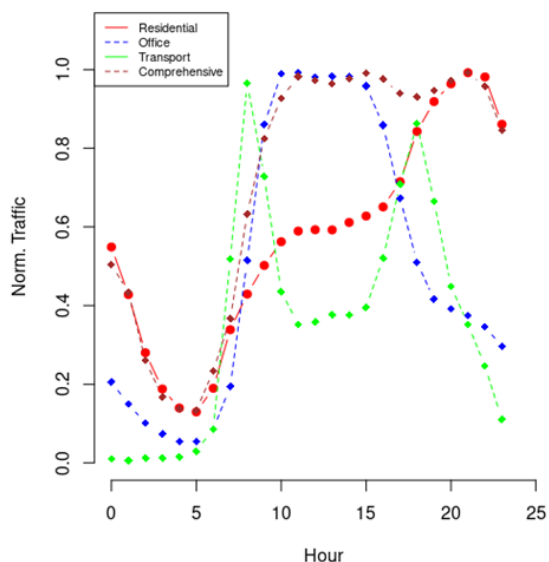

Figure 54 Normalized traffic profiles: Residential, Office, Transport and Comprehensive.

In this sense, Section 3.1 of Deliverable D4.3 shows a clustering based algorithm for finding groups of central offices with uncorrelated traffic patterns, on attempts to minimize the number of required transceivers. Figure 55 shows examples of different nodes with disparate traffic

profiles such that, when aggregated together, the number of subcarriers never exceed the maximum of 16 SCs, each one operating at 25 Gb/s.
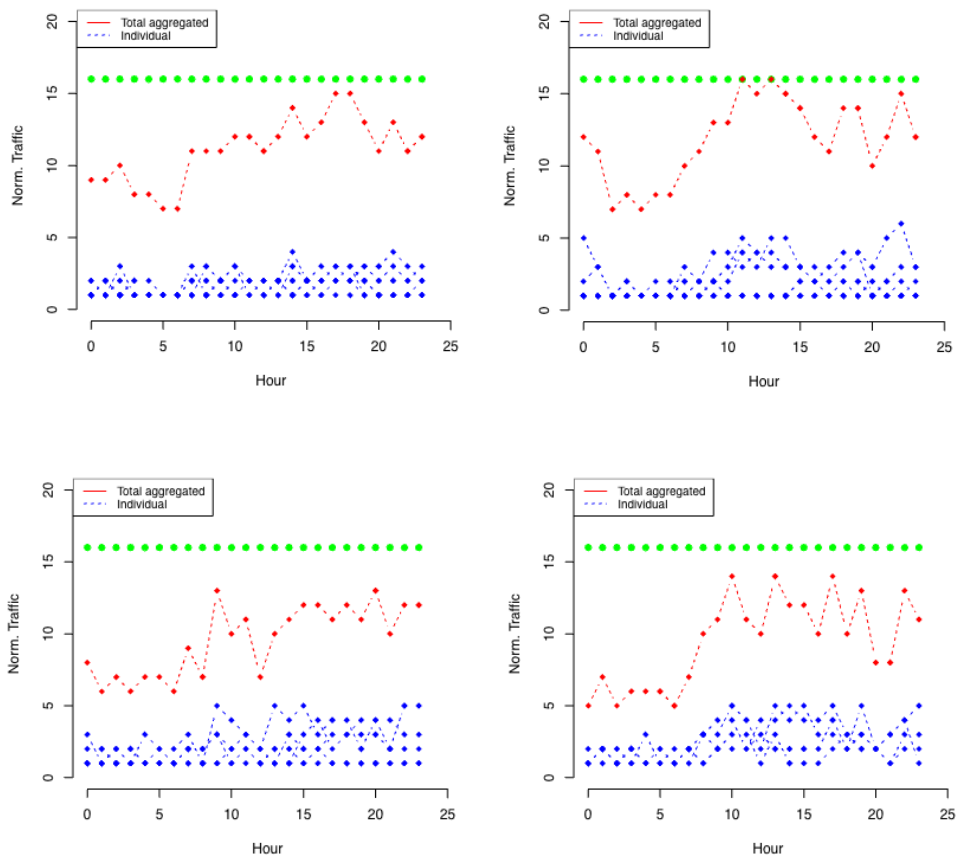

Figure 55 Daily traffic profiles for clusters/trees no. 1, 2, 3, and 4 for simulation case 1 (without geographical coordinates). In blue, is the number of 25 Gb/s subcarriers required by each P2MP leaf node. In red, is the total number of subcarriers required by all nodes in the same cluster or P2MP tree. In green, the maximum number of subcarriers (i.e., 16).

Table 10 shows a comparison of CAPEX when using fixed Point-to-Point transceivers versus Point-to-Multipoint transceivers, for different network settings with various traffic profiles. In such a comparison, in the fixed P2P setting, no dynamic allocation/sharing of bandwidth can be leveraged, and each P2P link must be dimensioned to the peak hour.

Table 10 - Comparison of P2MP versus P2P deployments and costs

Peak (Gb/s)	Var	400G	200G	100G	10G	P2P Cost units	P2MP trees	400G	100G	P2MP CU	Capex savings
U(0,100)	30%	0	234	698	68	10,860 CU	163	234	766	7404 CU	46.7%
U(10,100)	30%	0	264	736	0	11,584 CU	172	264	736	7584 CU	52.7%
U(50,100)	30%	0	482	518	0	12,892 CU	220	482	518	8892 CU	45.0%
U(0,100)	50%	12	369	558	61	11,894 CU	184	381	619	8282 CU	43.5%

| U(10,100) | 50% | 14 | 411 | 575 | 0 | 12,662 CU | 193 | 425 | 575 | 8550 CU | 48.0% |
| U(50,100) | 50% | 27 | 711 | 262 | 0 | 14,644 CU | 250 | 738 | 262 | 10644 CU | 40.4% |

In the first row of the table, we observe that 1000 nodes can be connected with 163 P2MP trees, which require a total of 234 high-rate and 766 low-rate transceivers. On the other hand, using P2P fixed transceivers would need 234 pairs of 200G, 698 pairs of 100G, and 68 pairs of 10G transceivers. Following the cost models of [Hos23,Her20], we may consider the following normalized cost units (CUs) for each P2P transceiver: 1 CU for 10G transceivers, 5 CU for 100G transceivers, 8 CU for 200G transceivers, and 12 CU for 400G transceivers. Thus, the CAPEX for P2P architectures depicted in the table is computed as:

$$Cost_{P2P} = 2 \times (12N_{400G} + 8N_{200G} + 5N_{100G} + N_{10G})$$

For the cost of P2MP trees, we assume that high-bitrate 400G P2MP transceivers have the same cost as in fixed P2P, that is, 12 CUs, while low-bitrate transceivers cost one half, that is 6 CUs, in line with state of the art estimates [Hos23,Her20]. Thus, the cost for P2MP trees follows:

$$Cost_{P2MP} = 12N_{high-br} + 6Nlow-br$$

As shown in the table, more fixed P2P transceivers are needed when both peak traffic and its variability increase, since P2P deployments need to be dimensioned to the peak. The rise in cost for P2MP technology is not as sharp as in the case of P2P deployments.

In total P2MP tree topologies designed with AI/ML clustering algorithms allow cost savings around 40 to 50% in all network settings studied. This is achieved thanks to the careful selection of nodes with uncorrelated traffic patterns to be on the same P2MP tree. Figure 56 summarizes this conclusion.

Figure 56 Total cost evolution in the short and medium term for 1,000 nodes: P2MP vs P2P technology.

8 Conclusion

This deliverable reports a set of techno-economic studies that target the KPIs defined for the B5G-OPEN project along the main technological and architectural aspects outlined in its charter. Building on the architectural definitions of WP2 and the data- and control-plane solutions developed in WP3 and WP4, respectively, the bulk of the project KPIs are addressed by experimental demonstrations (summarized in D5.2), and in this deliverable for theoretical analysis based on network simulation/optimization frameworks, qualitative analysis, and cost/service modeling.

The techno-economic evaluations attempt to characterize how B5G-OPEN architectures and devices allow to advance the state of the art in optical networks in terms of network deployment costs (CapEx), network operation costs (OpEx), environmental impact in the form of reduced CO_2 emissions, and higher offered service capacity by the end-to-end optical infrastructure. In order to do this, the main proposed innovations of B5G-OPEN were evaluated in reference scenarios compared to current network architectures. These innovations are reflected in the project KPIs and comprise:

- Multi-band networking
- Direct connectivity slicing across network domains
- Point-to-multipoint transceivers
- Packet/Optical integration and disaggregation
- Large-scale platforms for AI/ML based optical network monitoring and digital twins

From the studies presented in D5.3, we are able to quantify the type of improvements yielded by these different developments enabled by the project. Multi-band networks are shown to be a viable alternative to increase capacity in the short/medium-term at lower costs and are especially attractive for operators without easy/cheap access to deployable fibre. The expansion to the L- and S-bands can, if properly optimized in terms of optical performance, yield almost 3-fold capacity increases for shorter networks.

The benefits of P2MP transceivers were shown in various scenarios. The flexibility of these transceivers allows to more easily reconfigure traffic against changing patterns, as well as reduce power consumption significantly due to the reduced amount of router port consumption at hub nodes. Additionally, optimized network design that exploits the capabilities of P2MP interfaces, namely by designing optical trees that suit the efficiency of P2MP for hub-and-spoke traffic patterns, can further enhance the cost and power consumption benefits of deploying these interfaces in optical metro-access and metro-core networks.

The "optical continuum" concept, wherein services can be orchestrated across domains seamlessly, also can leverage multi-band networking to establish these differentiated services (in reach, capacity, etc.), across different bands and even using tailored optical switching nodes suited to each logical connectivity pattern.

Packet/optical integration was a key aspect of the project, which proposed extensive control/monitoring capabilities for disaggregated switches/routers across optical networks, but also integrating and controlling optical pluggables in the white boxes themselves. In the scope of D5.3, the techno-economic analysis shows the benefits of using these coherent pluggables deployed directly in router ports, as the cost and footprint of deploying chassis dedicated only

80

to transponder boxes can be avoided for metro applications in a multitude of network scenarios. This yields very significant cost and power consumption benefits for the deployment of optical capacity at scale.

Finally, massive monitoring and telemetry are fundamental to enable more and more AI powered applications to enhance and automate optical network operation. B5G-OPEN proposed a complete monitoring and telemetry platform, with distributed control and model training capabilities, that allows to massively scale up the amount of data that can be retrieved and processed to be used in AI/ML models. Some of these use-cases are also shown to yield concrete benefits in network operation, be it through avoiding failures altogether through monitoring/prediction and pre-emptive action, but also by reducing operation costs from maintenance operations due to the ability to properly schedule them across different network nodes.

REFERENCES

[100ZR] 100 ZR – (available at https://www.adtran.com/en/products-and-services/open-optical-networking/pluggables-and-subsystems/coherent-zr-series/coherent-100zr-series)

[400ZR] OIF 400ZR IA, https://www.oiforum.com/technical-work/hot-topics/400zr-2/

[Arp23] F. Arpanaei, M. R. Zefreh, J. A. Hernández, et al., "Launch power optimization for dynamic elastic optical networks over C+L bands," arXiv, arXiv:2308.13578 (2023).

[Arp23b] F. Arpanaei, J. M. Rivas-Moscoso, J. A. Hernández, et al.,"Migration strategies from C-band to C+L-band/multi-fibre solutions in optical metropolitan area networks," in 49th European Conference on Optical Communication (ECOC) (2023).

[Arp23c] F. Arpanaei, J. M. Rivas-Moscoso, M. R. Zefreh, et al., "A comparative study on routing selection algorithms for dynamic planning of EONs over C + L bands," in Advanced Photonics Congress (Optica Publishing Group, 2023), paper NeM3B.4.

[Bac20] J. Bäck, P. Wright, J. Ambrose, A. Chase, M. Jary, F. Masoud, N. Sugden, G. Wardrop, A. Napoli, J. Pedro, et al., "CAPEX savings enabled by point-to-multipoint coherent pluggable optics using digital subcarrier multiplexing in metro aggregation networks," in 2020 European Conference on Optical Communications (ECOC), pp. 1–4, IEEE, 2020.

[Bug22] H. Buglia, E. Sillekens, A. Vasylchenkova, et al., "On the impact of launch power optimization and transceiver noise on the performance of ultra-wideband transmission systems invited," J. Opt. Commun. Netw. 14, B11–B21 (2022).

[Bug23] H. Buglia, M. Jarmoloviäius, A. Vasylchenkova, et al., "A closedform expression for the Gaussian noise model in the presence of inter-channel stimulated Raman scattering extended for arbitrary loss and fibre length," J. Lightwave Technol. 41, 3577–3586 (2023).

[Chr96] D. N. Christodoulides and R. B. Jander, "Evolution of stimulated Raman crosstalk in wavelength division multiplexed systems," in *IEEE Photonics Technology Letters*, vol. 8, no. 12, pp. 1722-1724, Dec. 1996

[D2.1] B5G-OPEN Deliverable D2.1 – Definition of use cases, requirements, and reference network architecture (available at https://www.b5g-open.eu/wp-content/uploads/Deliverables/B5G-OPEN%20-%20D2.1%20Use%20Cases%20and%20Architecture%20v1.0_FINAL.pdf)

[Dev22] M. Devigili *et al.*, "Dual Time and Frequency Domain Optical Layer Digital Twin," in proc. ECOC 2022.

[Eri24] "Mobile data traffic outlook", Ericsson official web site [online, accessed October 21st 2024] https://www.ericsson.com/en/reports-and-papers/mobility-report/dataforecasts/mobile-traffic-forecast

[Ess12]   R. -J. Essiambre and R. W. Tkach, "Capacity Trends and Limits of Optical Communication Networks," in *Proceedings of the IEEE*, vol. 100, no. 5, pp. 1035-1055, May 2012

[Her20]   J. A. Hernández, M. Quagliotti, E. Riccardi, V. López, O. González de Dios, R. Casellas, "A techno-economic study of optical network disaggregation employing Open-Source Software business models for Metropolitan Area Networks", in IEEE Communications Magazine 58(5), 40-46, 2020.

[Her20b]   J. A. Hernandez, M. Quagliotti, L. Serra, L. Luque, R. Lopez da Silva, A. Rafel, O. Gonzalez de Dios, V. Lopez, A. Eira, R. Casellas, A. Lord, J. Pedro, and D. Larrabeiti, "Comprehensive model for techno-economic studies of next-generation central offices for metro networks," J. Opt. Commun. Netw. 12, 414–427 (2020).

[Hos23]   M. M. Hosseini, J. Pedro, A. Napoli, N. Costa, J. E. Prilepsky, and S. K. Turitsyn, "Multi-period planning in metro-aggregation networks exploiting point-to-multipoint coherent transceivers," J. Opt. Commun. Netw. 15, 155–162 (2023)

[IDE-D1.1] FP7 IDEALIST project deliverable D1.1, cordis.europa.eu/docs/projects/cnect/9/317999/080/deliverables/001-D11ElasticOpticalNetworkArchitecture.doc

[Inf23]   Infinera – "The seven vectors of ROADM evolution", available at www.infinera.com (2023).

[Kon19]   J. Yu, M. Kong, H.-C. Chien, et al., "400G/channel 50-GHz WDM coherent transmission: PS 64QAM versus hybrid 32/64QAM," in Optical Fiber Communication Conference (OFC) (Optica Publishing Group, 2019), paper Th3G.3.

[Lar19]   D. Larrabeiti, J. Fernández-Palacios, G. Otero, et al., "All-optical paths across multiple hierarchical levels in large metropolitan area networks," in Asia Communications and Photonics Conference (ACP) (2019).

[Lig22]   "Priorities of Service Providers for DWDM", LightCounting report [online, accessed October 21st 2024] [online, accessed October 21st 2024] https://www.lightcounting.com/resource/29/resourceFile/Priorities%20%20of%20%20Service%20%20Providers%20%20for%20DWDM%20%20Networks%20%20of%20%20the%20%20Future.pdf

[Mas23]   F. Masoud, A. Napoli, C.Castro, J. Pedro, B. Spinnler, A. Chase, D. Hillerkuss, D. Welch, "Environmental Impact of Coherent Point-to-Multipoint Pluggables in Metro Aggregation Optical Networks", Optical Network and Design Modeling (ONDM), 2023.

[Men01]   M. Menif, L. A. Rusch and M. Karasek, "Application of preemphasis to achieve flat output OSNR in time-varying channels in cascaded EDFAs without equalization," in *Journal of Lightwave Technology*, vol. 19, no. 10, pp. 1440-1452, Oct. 2001

[Nok]   Nokia - "ROADM and C+L solutions for reconfigurable and scalable WDM networks", available at www.nokia.com (2023).

83

[OPT-PSE]   OPT-PSE team within the Telecom Infra Project, "Github repository of GNPy," [Online]. Available:https://github.com/Telecominfraproject/oopt-gnpy.

[OR]   Open ROADM MSA, http://openroadm.org/

[OXR]   OpenXR Optics Forum MSA, https://openxropticsforum.org/

[OZR+]   OpenZR+ MSA, https://openzrplus.org/

[Ped22]   J. Pedro, N. Costa, and S. Sanders, "Cost-effective strategies to scale the capacity of regional optical transport networks," J. Opt. Commun. Netw. 14, A154–A165 (2022)

[Ped23]   J. Pedro, "Coherent pluggable optical transceivers: performance versus interoperability," Proc. of ELEKTRO 2024 (2024)

[Pog17]   P. Poggiolini and Y. Jiang, "Recent advances in the modeling of the impact of nonlinear fiber propagation effects on uncompensated coherent transmission systems," J. Lightwave Technol. 35, 458–480 (2017).

[Rap22]   M. Rapisarda, J. A. Hernandez, A. Gatto, et al., "All-optical aggregation and distribution of traffic in large metropolitan area networks using multi-Tb/s S-BVTs," J. Opt. Commun. Netw. 14, 316–326 (2022).

[Rui22]   M. Ruiz, D. Sequeira, and L. Velasco, "Deep Learning -based Real-Time Analysis of Lightpath Optical Constellations [Invited]," IEEE/OPTICA Journal of Optical Communications and Networking (JOCN), vol. 14, pp. C70-C81, 2022.

[Rui22b]   M. Ruiz, D. Sequeira, and L. Velasco, "Optical Constellation Analysis (OCATA)," https://doi.org/10.34810/data146, 2022.

[Sem19]   D. Semrau, E. Sillekens, R. I. Killey, et al., "A modulation format correction formula for the Gaussian noise model in the presence of inter-channel stimulated Raman scattering," J. Lightwave Technol. 37, 5122–5131 (2019).

[Seq18]   D. G. Sequeira, L. G. Cancela, and J. L. Rebola, "Impact of physical layer impairments on multi-degree CDC ROADM-based optical networks," in International Conference on Optical Network Design and Modeling (ONDM) (2018), pp. 94–99

[Sha19]   B. Shariati *et al.*, "Learning from the optical spectrum: Failure detection and identification", IEEE JLT 2019.

[Sha22]   H. Shakespear-Miles, M. Ruiz, A. Napoli, and L. Velasco, "Dynamic Subcarrier Allocation for Multipoint-to-Point Optical Connectivity," in Proc. PSC, 2022.

[Sho24]   Rob Shore, "Optical networking in 2024 - lighting the way forward," [Online]. Available:https://www.thefastmode.com/expert-opinion/34436-optical-networking-in-2024-lighting-the-way-forward

[Sou22]   A. Souza, N. Costa, J. Pedro, et al., "Benefits of counterpropagating Raman amplification for multiband optical networks," J. Opt. Commun. Netw. 14, 562–571 (2022).

[Sou24]   A. Souza, B. Correia, A. Napoli, V. Curri, N. Costa, J. Pedro, and J. Pires, "Cost analysis of ultrawideband transmission in optical networks," Journal of Optical Communications and Networking, vol. 16, no. 2, pp. 81–93, 2024.

[Tef24]   "Impact of traffic growth on networks and investment needs", Telefonica official web site [online, accessed October 21st 2024]: https://www.telefonica.com/en/communication-room/blog/impact-of-traffic-growth-on-networks-and-investment-needs/

[Tim23]   "Traffic and quality in the access network" (in Italian), Notiziario Tecnico TIM , N. 1 2023 [online, accessed October 21st 2024]: https://www.gruppotim.it/content/dam/gt/notiziario-tecnico/articoli/2023-n1/pdf_articoli/NotiziarioTecnicoTIM-1-2023-Traffico_e_qualita_nella_rete_accesso.pdf

[Vel17]   L. Velasco and M. Ruiz, "Provisioning, Recovery and In-operation Planning in Elastic Optical Networks," ISBN 978-1-119-33856-7, Wiley, 2017.

[Vel23]   L. Velasco, P. González, and M. Ruiz, "An Intelligent Optical Telemetry Architecture," in Proc. OFC, 2023.

[Wel21]   D. Welch, A. Napoli, J. B¨ack, W. Sande, J. Pedro, F. Masoud, C. Fludger, T. Duthel, H. Sun, S. J. Hand, et al., "Point-to-multipoint optical networks using coherent digital subcarriers," Journal of Lightwave Technology, vol. 39, no. 16, pp. 5232−5247, 2021.

[Wel22]   D. Welch, A. Napoli, J. B¨ack, S. Buggaveeti, C. Castro, A. Chase,X. Chen, V. Dominic, T. Duthel, T. A. Eriksson, et al., "Digital subcarrier multiplexing: Enabling software-configurable optical networks, " Journal of Lightwave Technology, 2022

[Xu16]   Xu et al., "Understanding mobile traffic patterns of large scale cellular towers in urban environment," IEEE/ACM Transactions on networking 25, 1147–1161 (2016)

[Zef20]   M. R. Zefreh and P. Poggiolini, "A real-time closed-form model for nonlinearity modeling in ultra-wide-band optical fiber links accounting for inter-channel stimulated Raman scattering and co-propagating Raman amplification," arXiv, arXiv:2006.03088 (2020).

[Zef21]   M. R. Zefreh and P. Poggiolini, "A GN-model closed-form formula supporting ultra-low fiber loss and short fiber spans," arXiv, arXiv:2111.04584 (2021)

< End of the deliverable report >